Report 2

N63 20254

163p.

CODE-1

563310

184 P25

FLUX SWITCHING IN MULTIPATH CORES

Prepared for:

JET PROPULSION LABORATORY
4800 OAK GROVE DRIVE
PASADENA, CALIFORNIA

CONTRACT 950095
UNDER NASw-6

By: D. Nitzan V. W. Hesterman

STANFORD RESEARCH INSTITUTE

MENLO PARK, CALIFORNIA

SRI

OTS PRICE

XEROX $ [redacted]

MICROFILM $

SQT-7674

STANFORD RESEARCH INSTITUTE

MENLO PARK, CALIFORNIA

SRI

November 1962

Report 2

FLUX SWITCHING IN MULTIPATH CORES

Prepared for:

JET PROPULSION LABORATORY
4800 OAK GROVE DRIVE
PASADENA, CALIFORNIA

CONTRACT 950095
UNDER NASw-6

By: *D. Nitzan* *V. W. Hesterman*

SRI Project No. 3696

Approved:

MB adams for

J. R. ANDERSON, MANAGER COMPUTER TECHNIQUES LABORATORY

J Noe

J. D. NOE, DIRECTOR ENGINEERING SCIENCES DIVISION

Copy No. 163

62521

ABSTRACT

A three-region static $\phi(F)$ curve is calculated from two empirical hyperbolic functions that use five material parameters; very close agreement with experimental data is obtained in a practical range of application. After the limitations of a leg model are pointed out, the inelastic-switching parameter ρ of a tapered leg is calculated as a function of material properties, geometry, and flux level; this parameter is useful for practical multipath cores whose legs usually vary in width. Based on a parabolic model for $\rho(\phi)$, average ρ of a constant-width leg and a tapered leg are calculated and plotted *vs.* flux change; these plots are applicable to circuits involving partial or full switching. Flux-division ratio D between two legs in parallel *vs.* MMF drive NI, applied to a third leg in series, is calculated in terms of leg parameters for a general case, and then simplified to special cases, *e.g.*, unloaded core, or $NI \to \infty$. For relatively low NI, leg parameters are improved by considering the nonlinearity of the function peak $\dot{\phi}$ *vs.* F. For relatively high NI, the effect of leg dimensions on D is expressed more directly. In view of the complexity of the analysis, the agreement with experimental data, especially in the no-load case, is quite good. Experiments were also performed in order to study flux division in a nonsaturable core. Modification of the parabolic switching model to account for variation of the dynamic threshold with flux for low MMF results in closer agreement with experimental $\dot{\phi}(\phi)$ data. Problems in determination of leg dimensions are discussed relative to two cores that were designed for flux-division experiments. A new model is proposed for the process of slow flux switching in a core having a re-entrant shape. Laboratory techniques for determination of switching parameters are presented, and examples are given. The unsetting effect is measured as a function of applied MMF; the results are in full agreement with the qualitative analysis in a previous report.

CONTENTS

CONTENTS

ILLUSTRATIONS

ILLUSTRATIONS

TABLES

LIST OF SYMBOLS

Symbol	Definition	Reference*
A	Cross-sectional area of a leg	Rep. 1, Fig. 19
A^{min}	Constricting A of a variable-width leg	p. 10
B	Flux density	
B_e	B in negative saturation	Eq. (10)
B_i	B along the short edge of a leg	p. 9
B_o	B along the long edge of a leg	p. 9
B_r	Maximum residual B	Fig. 2
B_s	Saturation B fitting parabolic model for ζ	Eq. (24)
B_{ss}	Saturation B fitting hyperbolic models for static $B(H)$	Eqs. (10); (11)
B_u	Static B for $H \geq H_{th}$	Eq. (11)
ΔB	Change of B	
ΔB_i	ΔB along the short edge of a leg	p. 8
ΔB_o	ΔB along the long edge of a leg	p. 8
$\dot{B}$	Time rate of change of B	
$\dot{B}_i$	$\dot{B}$ along the short edge of a leg	p. 9
$\dot{B}_o$	$\dot{B}$ along the long edge of a leg	p. 9
$\dot{B}_p$	Peak $\dot{B}$	Eq. (82)
C	Capacitance	
c	r_b/r_a in a tapered leg	p. 22
D	Flux-division ratio	Eq. (58) and Fig. 10
$D_{NI\to\infty}$	Asymptotic value of D as $NI \to \infty$	Fig. 14

---

*Reference to Report 1 (*i.e.*, Ref. 1) is preceded by "Rep. 1."

SYMBOLS

Symbol	Definition	Reference
D_{NL}	D for no-load case	Eq. (74)
$D_{NL,\,NI\to\infty}$	Asymptotic value of D_{NL} as $NI \to \infty$	Eq. (78); **Fig. 14**
$D_{\delta\to 1}$	D for $\delta \to 1$ case	Eq. (79)
$D_{NL,\,\delta\to 1}$	$D_{\delta\to 1}$ in no-load case	Eq. (80); **Fig. 14**
$D_{\delta\to 1,\,NI\to\infty}$	Asymptotic value of $D_{\delta\to 1}$ as $NI \to \infty$	Eq. (81)
$D_{NL,\,\delta\to 1,\,NI\to\infty}$	$D_{\delta\to 1,\,NI\to\infty}$ in no-load case	Eq. (81a)
e	Voltage	
F	MMF	
F_{ex}	Excess MMF; *i.e.* $F - F_0$	p. 18
F_i^{max}	Static saturation MMF of the short edge of a leg	Eq. (6)
F_i^{min}	Static threshold MMF of the short edge of a leg	Eq. (5)
F_0	Dynamic MMF threshold	Eq. (23)
F_{0jk}	F_0 of Legs j and k in series	*e.g.* p. 85
F''_0	Dynamic MMF threshold for low F	Eqs. (90) and (92); Fig. 15
F''_{0jk}	F''_0 of Legs j and k in series	
F'_0	Modified F_0 for low F	Eqs. (93) and (95); Fig. 15
$\overline{F}$	Time-averaged F	*e.g.* Eq. (106)
g	Geometry ratio l_o/l_i	Eq. (8)
g_{ii}	Curvilinear parameter	Eq. (B-2)
H	Magnetic field	
H_a	Parameter in the hyperbolic model for $B_e(H)$	Eq. (10); Fig. 2
H_B	H at boundary between linear and nonlinear regions of $\dot{B}_p(H)$	Fig. 15

SYMBOLS

Symbol	Definition	Reference
H_c	Coercive H	Eq. (14); Fig. 2
H_i	H along the short edge of a leg	p. 8
H_n	Parameter in the hyperbolic model for $B_u(H)$	Eq. (11); Fig. 2
H_o	H along the long edge of a leg	p. 8
H_q	Parameter in the hyperbolic model for $B_u(H)$	Eq. (11); Fig. 2
H_r	H corresponding to $B = B_r$ on static $B(H)$ curve	Eq. (15); Fig. 2
H_{th}	Static H threshold	Eq. (12); Fig. 2
H_0	Dynamic H threshold	Eq. (24); Fig. 15
H''_0	Dynamic H threshold for low H	Eq. (83); Fig. 15
H'_0	Modified H_0 for low H	Eqs. (84) and (86); Fig. 15
H^{max}	Saturation H of linearized static $B(H)$	Rep. 1, Fig. 4(b)
H^{min}	Threshold H of linearized static $B(H)$	Rep. 1, Fig. 4(b)
$\overline{H}$	Time-averaged H	
h	Height of a leg (or core)	Rep. 1, Fig. 19
I	Current	
I_C	CLEAR current	Rep. 1, Fig. 57(a)
I_{dc}	Direct current	*e.g.* Fig. 17(a)
I_s	SET current	Rep. 1, Fig. 57(a)
i_L	Load current	Fig. 10
ID	Inside diameter of a toroid	
K	Gain of preamplifier	App. E
L	Inductance	
l	Leg length	Rep. 1, Fig. 19

SYMBOLS

Symbol	Definition	Reference
l_i	l of the short edge of a leg	Rep. 1, Fig. 19
l_o	l of the long edge of a leg	Rep. 1, Fig. 19
l_{jk}	l of Legs j and k in series	
l_{ijk}	l_i of Legs j and k in series	*e.g.* Fig. 28
l_{ojk}	l_o of Legs j and k in series	*e.g.* Fig. 28
l^{av}	Average l, *i.e.* $(l_i + l_o)/2$	*e.g.* Fig. 22
l_{jk}^{av}	l^{av} of Legs j and k in series	*e.g.* p. 85
l^{max}	Maximum l	p. 61
l^{min}	Minimum l	p. 61
$\mathbf{M}$	Magnetization vector	p. 65 and Fig. 25
$\mathbf{M}_i$	Initial $\mathbf{M}$	Fig. 26(d)
$\mathbf{M}_f$	Final $\mathbf{M}$	Fig. 26(d)
$\Delta\mathbf{M}$	Change of $\mathbf{M}$	Fig. 26(d)
$\dot{\mathbf{M}}$	Time rate of change of $\mathbf{M}$	p. 61
N	Number of turns	
N_C	N of CLEAR winding	Rep. 1, Fig. 57(a)
N_L	N of Load winding	Fig. 10
N_s	N of SET winding	Rep. 1, Fig. 57(a)
NI	Applied MMF	*e.g.* Fig. 10
NI_{Bj}	NI yielding $\overline{H} = H_B$ in Leg j	*e.g.* Eq. (108) and Fig. 15
$NI_{D\to\infty}$	Asymptotic value of NI as $D \to \infty$	Eq. (75); Fig. 14
n	Number of curvilinear squares	App. B
OD	Outside diameter of a toroid	
p	Flux-division parameter	Eqs. (70) and (73)

SYMBOLS

Symbol	Definition	Reference
$p_{NI\to\infty}$	p for $NI \to \infty$	Eq. (76)
q	Flux-division parameter	Eqs. (71) and (73)
$q_{NI\to\infty}$	q for $NI \to \infty$	Eq. (77)
R	Resistance	
R_L	Load resistance	Fig. 10
r	Radius	
r_a	Short radius of a tapered leg	Fig. 3
r_b	Long radius of a tapered leg	Fig. 3
r_i	Inside radius of a toroid	
r_o	Outside radius of a toroid	
S_w	Switching coefficient	Rep. 1, Eq. (46)
T	Time length of I pulse	*e.g.* Fig. 10
t	Time	
u	Per-unit flux, *i.e.* ϕ/ϕ_s	p. 20
u_f	Final u, *i.e.* ϕ_f/ϕ_s	p. 20
u_j	Curvilinear jth coordinate ($j = 1,2,3$)	App. B
u_{ja}; u_{jb}	Boundary values of u_j in a leg	Fig. B-1
u_r	Maximum residual u, *i.e.* ϕ_r/ϕ_s	p. 20
w	Width of a leg	Rep. 1, Fig. 19
x	Equi-F coordinate in a leg	Rep. 1, Fig. 19
α	Angle formed by leg cross sections	Rep. 1, Fig. 19
β	Angle of a tapered leg	Fig. 3
γ	Flux-division parameter	Eqs. (66) through (69)
δ	Residual-flux parameter	Eq. (68)
ϵ	Coefficient of elastic $\dot{\phi}$	Rep. 1, Eq. (33)

SYMBOLS

Symbol	Definition	Reference
ζ	Coefficient of inelastic $\dot{B}$	Eq. (24)
ζ_p	Peak ζ	Eqs. (24) and (25)
ζ_p'	Modified ζ_p in nonlinear $\dot{B}_p(H)$ region	Eqs. (84) and (85); Fig. 15
η	Flux form factor	Eqs. (37) and (39)
η	Bicylindrical coordinate	App. B
η_t	Flux form factor of a tapered leg	Eqs. (34) and (36)
θ	Angular coordinate of a tapered leg	Fig. 3
θ	Angle between crossover zone and edges of a leg having a re-entrant shape	Fig. 26
κ	Coefficient of inelastic $\dot{B}$ in nonlinear $\dot{B}_p(H)$ region	Eq. (83); Fig. 15
λ	Coefficient of inelastic $\dot{\phi}$ in nonlinear $\dot{\phi}_p(F)$ region	Eqs. (90) and (91); Fig. 15
μ	Permeability	Eq. (26)
μ_0	μ of vacuum (air)	
ν	Power coefficient of inelastic $\dot{B}$ in nonlinear $\dot{B}_p(H)$ region	Eq. (83)
ρ	Coefficient of inelastic $\dot{\phi}$	Eq. (23)
ρ_{av}	Flux-averaged ρ	Eq. (40)
ρ_{jk}	ρ of Legs j and k in series	
ρ_p	Peak ρ	Eq. (23)
ρ_{jkp}	ρ_p of Legs j and k in series	*e.g.* p. 85
ρ_p'	Modified ρ_p in nonlinear $\dot{\phi}_p(F)$ region	Eqs. (93) and (94)
ρ_t	ρ of a tapered leg	Eq. (33)
ρ_{tp}	Peak ρ_t	Eq. (35)
$\overline{\rho}$	Average ρ	Eqs. (44), (45) and (49)

SYMBOLS

Symbol	Definition	Reference
$\bar{\rho}_t$	$\bar{\rho}$ of a tapered leg	Eq. (50)
τ	Switching time	p. 18
ϕ	Magnetic flux	
ϕ_{air}	ϕ in vacuum (air)	Eq. (22)
ϕ_f	Final ϕ	p. 17
ϕ_r	Maximum residual ϕ	p. 17; Fig. 12
ϕ_{res}	Residual ϕ	p. 34
ϕ_s	Saturation ϕ in parabolic model for $\dot{\phi}$	Eq. (23)
ϕ_{ss}	Saturation ϕ in calculated static $\phi(F)$	Eq. (21)
ϕ_0	Initial flux level	p. 18
$\Delta\phi$	Change of ϕ	*e.g.* Fig. 12
$\Delta\phi_\epsilon$	Elastic $\Delta\phi$	Rep. 1, p. 19
$\dot{\phi}$	Time rate of change of ϕ	
$\dot{\phi}_p$	Peak $\dot{\phi}$	Eq. (87)
$\dot{\phi}_{jkp}$	$\dot{\phi}_p$ of Legs j and k in series	*e.g.* p. 85
$\dot{\phi}_\epsilon$	Elastic $\dot{\phi}$	Rep. 1, Eq. (32)
$\mathcal{R}$	Reluctance	Eq. (27)

ACKNOWLEDGMENT

The valuable criticism and helpful suggestions of Dr. D. R. Bennion are gratefully acknowledged.

PREFACE

This is the second report on flux switching in multipath cores. In the first report, all available published and unpublished material related to this subject was organized and evaluated, and new material was added. Conclusions were drawn about areas that needed further investigation. An attempt is made here to fill some of these gaps. Since this report is a direct continuation of the first report, reference to Report 1 is made frequently in order to save space. The reader is advised to have Report 1 on hand; otherwise the chain of reasoning in many occasions will be hard (or even impossible) to follow.

The material in this report is divided into two sections: The first section contains theoretical calculations; the second section covers mainly experimentation and discussion of measured data versus the corresponding theory. It is recognized that in some cases this division of a topic may be a nuisance. However, since part of the material in Sec. I has not yet been verified experimentally, and since part of the material in Sec. II stands alone and part is related to a theory developed in Report 1, this classification was chosen.

All equations are written in the MKS system of units. However, the numerical values of some quantities are given in other metric units for convenience as to their size. In most of these cases, only a decimal change is required to convert to MKS units. For example, flux values are given in CGS maxwells, which can be converted to MKS webers by multiplying by 10^{-8} wb/maxwell.

Section I is divided into four parts. Parts A, B, and C deal with leg models and switching parameters and are intended to improve and extend our analytical tools in dealing with flux switching in multipath cores. In Part A, realistic functions for static $\phi(F)$ are calculated. In Part B, the concept of a leg model is extended to a variable-width leg and the inelastic-switching parameter ρ of a tapered leg is calculated. In Part C, calculation of average ρ, which was developed in

Report 1 only for $\Delta\phi = 2\phi_r$, is extended to the case where $\Delta\phi$ may vary continuously from zero to $2\phi_r$. Part D contains analytical calculation of the flux-division phenomenon that was described in Report 1 with no explanation. Due to the lack of switching models of a leg in a partially-switched state, a saturable core (*e.g.*, a shaped MAD), rather than a nonsaturable core (*e.g.*, the Laddic) is assumed. Part D is by far the most significant part of Sec. I.

Section II is divided into five parts. In Part A, material properties are of concern, and since these properties can be best measured by testing a toroidal core, all the experiments in Part A are performed on a toroid. In Part B, interest is focused on the geometrical properties of a leg and, in particular, on how to divide a multipath core into legs and how to determine the leg dimensions in doubtful cases, such as when the division into legs depends on where *NI* is applied, or when the switching path does not follow the leg contour. Part C contains test procedure and laboratory techniques for measurement of leg parameters, which are affected by both the material properties and the geometrical properties. In Part D, flux division in a nonsaturable core is studied experimentally; experimentation and machine computation of flux division in a saturable core are described and compared. Finally, in Part E, the unsetting effect, which was described in Report 1, is verified experimentally.

I CALCULATIONS

The objective of this section is twofold. In Parts A, B, and C, we shall extend our analytical tools by calculating the following: a realistic static $\phi(F)$ curve, inelastic-switching parameter ρ of a tapered leg, and average ρ for partial or full flux switching of a constant-width leg and a tapered leg. In Part D, we shall employ the parabolic model for ρ to analyze flux division in a saturable core.

A. MODELS FOR STATIC $\phi(F)$ CURVE

In a previous report[1]* (hereinafter referred to as Report 1), various models for the static relation between B and H were described. One of these models [Report 1, Fig. 4(b)iii, p. 4] approximates this relation by straight lines, which are horizontal in saturation and sloping between saturation levels. Based on this model, the static $\phi(F)$† curve of a toroidal core was calculated by integrating B from $r = r_i$ to $r = r_o$ (*cf.* Report 1, pp. 36-39). We would first like to extend this calculation to a constant-width leg (*cf.* Report 1, p. 18). The drawback of this model stems from the assumption that $B(H)$ is piecewise linear, when in fact $B(H)$ is nonlinear. Our main objective is to calculate $\phi(F)$ from a more realistic $B(H)$ function.

1. $\phi(F)$ BASED ON PIECEWISE LINEARIZED $B(H)$

The piecewise linearized $B(H)$ curve between saturation levels [Fig. 4(b)iii, Report 1, p. 4] for $H^{max} \geq H \geq H^{min}$ is described by

$$B = -B_r + \frac{2B_r}{H^{max} - H^{min}} (H - H^{min}) \quad . \tag{1}$$

---

* References are listed on p. 153.

† The term "ϕ-F" in Report 1 is replaced by the term "$\phi(F)$" in order to emphasize that ϕ is a function of F. Similarly, "$B(H)$" will be used instead of "B-H." The difference between the terms static "curve" and static "loop" is trivial. A static "curve" is a portion of a static "loop," and is obtained by varying H (or F) in one direction, so that no hysteresis is recorded. The term "ϕ-F curve" in Report 1 (*cf.* p. 45) stands for residual (or peak, if so specified) flux. This will be preceded by "T-microsecond," *e.g.*, "20-μsec $\phi(F)$ curve."

Consider a leg such as shown in Fig. 19 of Report 1 (p. 18) of constant width w, height h, angle α and edge lengths l_i and l_o, and assume that an MMF F is applied along the leg. At a radial distance x from the inner edge,

$$H = \frac{F}{l} \tag{2}$$

where, following Eq. (26) of Report 1 (p. 18),

$$l = l_i + \alpha x = l_i + \frac{l_o - l_i}{w} x \quad . \tag{3}$$

Substituting Eqs. (2) and (3) into Eq. (1), we obtain the relation

$$B(F,x) = \frac{2B_r}{F_i^{max} - F_i^{min}} \left(\frac{F}{1 + \frac{\alpha}{l_i} x} - \frac{F_i^{max} + F_i^{min}}{2} \right) , \tag{4}$$

where

$$F_i^{min} = H^{min} l_i \quad , \tag{5}$$

and

$$F_i^{max} = H^{max} l_i \quad . \tag{6}$$

The $\phi(F)$ curve is obtained by integrating $B(F,x)$ over the leg cross section, *i.e.*,

$$\phi = h \int_0^w B(F,x) dx \quad . \tag{7}$$

The flux state in each of the five segments (Fig. 39, Report 1, p. 38) for the case where $l_o H^{min} < l_i H^{max}$ is shown in Fig. 1. The boundaries corresponding to each segment are indicated by dashed lines. Integrating Eq. (7) over these boundaries, we get the same relations between ϕ and F as expressed by Eqs. (57) through (62) of Report 1 (p. 39), except that $2\pi r_i$ and $2\pi r_o$ are replaced by l_i and l_o, so that F_i^{min} and F_i^{max} are as given in Eqs. (5) and (6),

$$g = \frac{l_o}{l_i} \quad , \tag{8}$$

and

$$L_i = \frac{hB_r}{F_i^{max} - F_i^{min}} \frac{l_i}{\alpha} \quad . \tag{9}$$

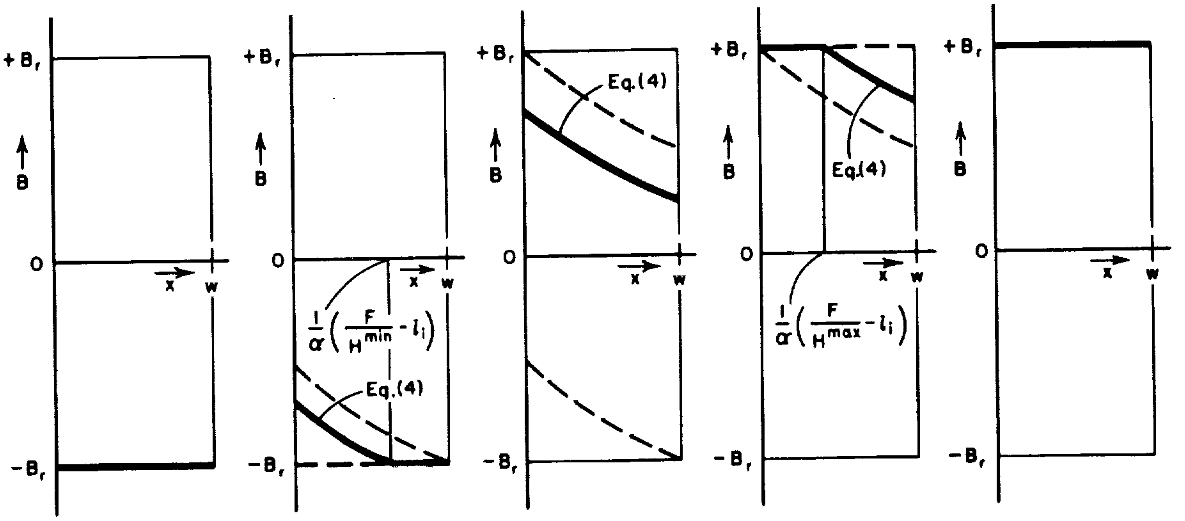

(a) SEGMENT 1 (b) SEGMENT 2 (c) SEGMENT 3 (d) SEGMENT 4 (e) SEGMENT 5

RB-3696-160

FIG. 1 STATIC FLUX STATES FOR LINEARIZED B(H) MODEL

2. $\phi(F)$ BASED ON HYPERBOLIC MODELS FOR $B(H)$

A hyperbolic model for $B(H)$ in negative saturation was proposed in Report 1 (p. 19). According to this model,

$$B \equiv B_e = -B_r - (B_{ss} - B_r) \frac{H}{H - H_a} + \mu_0 H \tag{10}$$

where H_a and B_{ss} are empirical material parameters [replacing Parameters a and B_s in Report 1 (p. 19)]. This model describes the static $B(H)$ for $H \leq H_{th}$, where H_{th} is the threshold value of H above which inelastic switching takes place.

For $H \geq H_{th}$, the following hyperbolic model is a good approximation.

$$B \equiv B_u = -B_r + (B_{ss} + B_r) \frac{H - H_q}{H - H_n} + \mu_0 H \qquad (11)$$

where H_q and H_n are material parameters.

The plots of these hyperbolic models for the material $B(H)$ are shown in Fig. 2. The intersection point, Point P, represents the transition from the region of elastic switching to the region of inelastic switching; hence, H at Point P is the threshold field H_{th}. By equating Eqs. (10) and (11), we find that

$$H_{th} = \frac{1}{4}\left[H_s - \sqrt{H_s^2 - 8\left(1 + \frac{B_r}{B_{ss}}\right) H_a H_q}\right] \qquad (12)$$

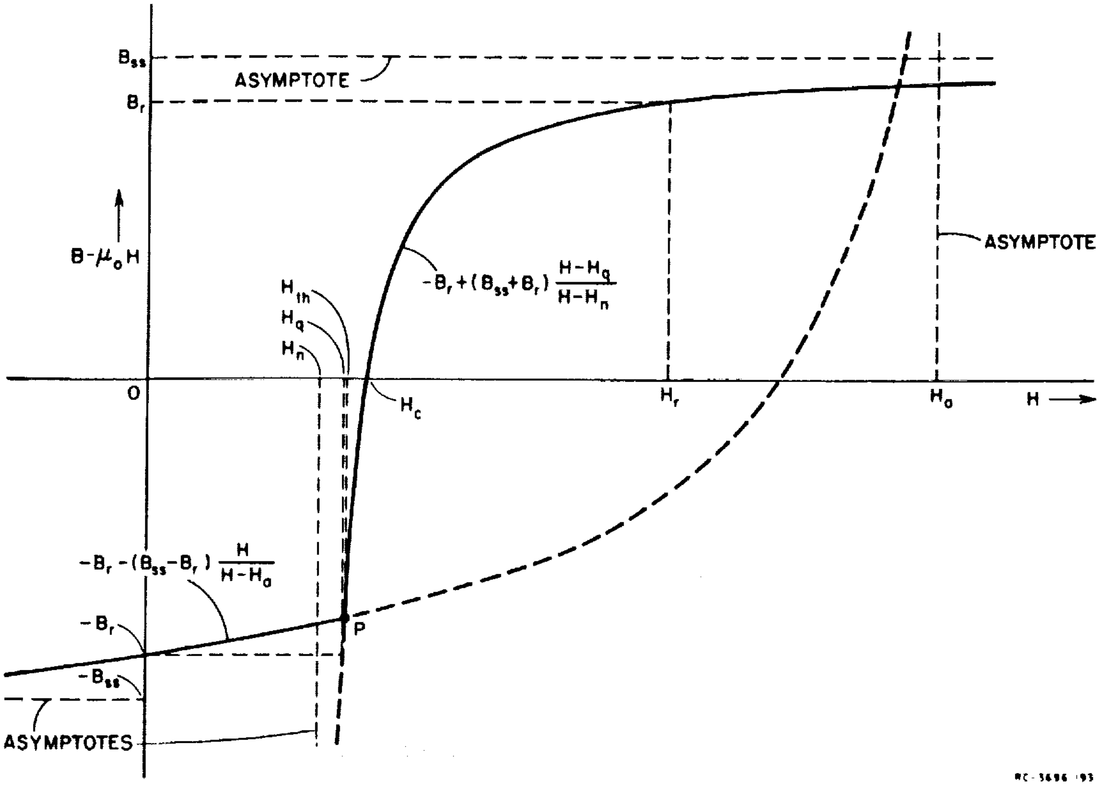

FIG. 2 HYPERBOLIC MODELS FOR STATIC B(H)

where

$$H_s = H_a + H_q + H_n + \frac{B_r}{B_{ss}} (H_a + H_q - H_n) \quad . \tag{13}$$

Note that the plots in Fig. 2 describe only the material contribution to B. By equating $B_u - \mu_0 H$ in Eq. (11) to zero and B_r, we obtain expressions for the coercive field H_c and for H_r:

$$H_c = H_q + \frac{B_r}{B_{ss}} (H_q - H_n) \tag{14}$$

and

$$H_r = \frac{(B_{ss} + B_r)H_q - 2B_r H_n}{B_{ss} - B_r} \quad . \tag{15}$$

The hyperbolic models for $B(H)$ [Eqs. (10) and (11)] are used in Appendix A to calculate a static $\phi(F)$ curve of a constant-width leg. The resulting expressions, Eqs. (A-3), (A-6), and (A-7), describe static $\phi(F)$ in three regions of F: $F \leq H_{th} l_i$, $H_{th} l_i \leq F \leq H_{th} l_o$, and $H_{th} l_o \leq F$. For low-threshold ferrite material, if $|F|$ is lower than, say 1% of $B_{ss} l_i / \mu_0$, some terms in these expressions are negligible. These negligible terms include the so-called air flux and, in the region $H_{th} l_i \leq F \leq H_{th} l_o$, the elastic flux change in the leg section that has not switched inelastically. By ignoring these terms, Eqs. (A-3), (A-6), and (A-7) are reduced to the following expressions:

for $F \leq H_{th} l_i$,

$$\phi = \frac{hw(B_{ss} - B_r)}{(l_o - l_i)H_a} F \ln \left(\frac{F - H_a l_o}{F - H_a l_i} \right) - B_r hw \quad ; \tag{16}$$

for $H_{th} l_i \leq F \leq H_{th} l_o$,

$$\phi = \frac{hw(B_{ss} + B_r)H_q}{(l_o - l_i)H_n} \left\{ \frac{F}{H_{th}} - l_i + F\left(\frac{1}{H_n} - \frac{1}{H_q}\right) ln \left[\frac{F\left(1 - \frac{H_n}{H_{th}}\right)}{F - H_n l_i} \right] \right\} - B_r hw \quad ; \tag{17}$$

and for $H_{th} l_o \leq F$,

$$\phi = \frac{hw(B_{ss} + B_r)H_q}{(l_o - l_i)H_n} \left[l_o - l_i + F\left(\frac{1}{H_n} - \frac{1}{H_q}\right) ln \left(\frac{F - H_n l_o}{F - H_n l_i}\right) \right] - B_r hw \quad . \tag{18}$$

Equations (16), (17), and (18) hold for a large practical range of F. We have assumed this range to be $\pm 0.01(B_{ss} l_i/\mu_0)$ so that B_{air} is less than 1% of B_{ss}. For cores to be described in Sec. II, this amounts to about 50 times $H_{th} l_o$. Beyond this range, the air flux becomes increasingly significant.

For $|F| >> H_{th} l_o$, Eqs. (A-3) and (A-7) may be approximated by

$$\phi = -\phi_{ss} + \phi_{air} \tag{19}$$

and

$$\phi = \phi_{ss} + \phi_{air} \quad , \tag{20}$$

where

$$\phi_{ss} = B_{ss} hw \tag{21}$$

and

$$\phi_{air} = F \frac{hw\mu_0}{l_o - l_i} ln \left(\frac{l_o}{l_i}\right) \quad . \tag{22}$$

The term ϕ_{air} stems from the flux density $\mu_0 H$ in the cross-sectional area hw of the leg.

Experimental verification for Eqs. (16), (17), and (18) will be given in Sec. II-C-3.

3. SUMMARY

Two empirical hyperbolic functions have been proposed for describing the static $B(H)$ curve, requiring five material parameters: B_{ss}, B_r, H_a, H_n, and H_q. The first function, Eq. (10), covers the region of negative saturation, and includes the parameters B_{ss}, B_r, and H_a. The second function, Eq. (11), covers the nonsaturation region as well as the region of positive saturation, and it includes the parameters B_{ss}, B_r, H_n, and H_q. Based on these functions, the static $\phi(F)$ curve was calculated by integrating B over the leg cross section. This curve is composed of three portions that are described by Eqs. (16), (17), and (18). Calculated and measured $\phi(F)$ curves will be compared in Sec. II-C-3.

B. TAPERED LEG

Switching models for a constant-width leg were developed in Ref. 1. In some commercially available multipath cores, leg widths are not constant. For example, the widths of the inner legs (Leg 2 and Leg 3) in a three-hole MAD [Report 1, Fig. 1(b), (p. 2)] are variable. Another example is the Transfluxor, which is an unshaped three-leg core, similar to the core in Fig. 123 of Report 1 (p. 126). In the Transfluxor, all three legs vary in width. The question is, what are the switching parameters of a variable-width leg, and in particular, how do these parameters differ from those of a constant-width leg? The answer to this question is not an easy one. The objective in this section is to discuss the factors that are involved in this problem and to propose a partial solution for a simple case, namely, to calculate the inelastic-switching coefficient ρ of a tapered leg. Before we examine a variable-width leg, it is appropriate to discuss further the limitations of a leg model in general, *i.e.*, limitations that apply to both constant-width and variable-width legs.

1. LEG-MODEL LIMITATIONS

The difficulty in defining the boundaries of relatively short legs was regarded in Report 1 (p. 3) as a limitation on the leg model. The leg model has additional limitations that will be discussed as follows:

(1) A given F is applied across a leg of edge lengths l_i and l_o. Let us denote the variables associated with the short and long edge by subscripts i and o, respectively. Since $l_i < l_o$, $H_i > H_o$ and, hence, $\Delta B_i > \Delta B_o$. This means that the flux switching is not uniformly distributed. A leg model should account for such a nonuniformity by assuming a model for B versus H, and integrating the variation in B across the leg width. In Report 1, this was accomplished for the static characteristics (pp. 36-39) and for the elastic-switching model (Report 1, Appendix B, pp. 187-188). This was also done in Part A of this report in calculating a static $\phi(F)$ curve, based on hyperbolic models for $B(H)$. On the other hand, variation in B across the leg is not accounted for by the inelastic-switching parabolic model[*]

$$\dot{\phi} = \rho(F - F_0) = \rho_p \left(1 - \frac{\phi^2}{\phi_s^2}\right)(F - F_0) \quad . \tag{23}$$

In order to account for such a variation, the parabolic model for inelastic switching should be first written in terms of B and H, rather than ϕ and F, *i.e.*,

$$\dot{B} = \zeta(H - H_0) = \zeta_p \left(1 - \frac{B^2}{B_s^2}\right)(H - H_0) \quad , \tag{24}$$

where, following Eq. (49) in Report 1 (p. 30),

$$\zeta_p \cong 1.6 \frac{2B_r}{S_w} \quad . \tag{25}$$

---

[*] In Report 1, the parabolic model for ρ was written as $\rho = \rho_p[1 - (\phi/\phi_r)^2]$. As pointed out in Report 1 (p. 28), this model implies the absurdity of infinite switching time for $\dot{\phi}$ to reach a peak value, unless the initial flux level is assumed to be $-\phi_{r0}$, slightly above $-\phi_r$, where $\phi_{r0} < \phi_r$. Experimental observation[2] also indicates that the initial value of ρ is slightly above zero. In the present report, we modify the parabolic model into $\rho = \rho_p[1 - (\phi/\phi_s)^2]$, where $\phi_s > \phi_r$ (note that $\phi_s \not\equiv \phi_{ss}$). The value of ϕ_s is so determined as to yield good fit within a range of excess MMF of application, say up to $5F_0$. In this way, the initial flux level, denoted by ϕ_0, could be assumed to be $-\phi_r$. This assumption is supported by the appreciable size of domains of reversed magnetization[3] (positive domains) at the static state of $\phi = -\phi_r$. Additional refinement is based on our assumption that inelastic switching is preceded by elastic switching (*cf.* Report 1, p. 14), and therefore the initial flux level ϕ_0 might be above $-\phi_r$, especially when a high F with a short rise time is applied.

Equation (24) should then be integrated across the leg width. Calculation of this sort for a toroidal core can be found in Ref. 2, but the results are too complicated to be practical. With the use of a modern computer-programming language, such as ALGOL or FORTRAN, this complicated model may become useful.

(2) Due to the nonlinearity associated with the parabolic model, Eq. (24), the nonuniformity in B distribution across the leg cross section becomes worse prior to the time when $B_i(t)$ passes through zero. To understand this, suppose that the leg is initially at negative saturation, and a constant MMF F is applied across the leg. As explained in (1) above, $\Delta B_i > \Delta B_o$, and, hence, $B_i > B_o$. Substitution of the condition $B_i > B_o$ into Eq. (24) results in $\dot{B}_i > \dot{B}_o$, which, in turn, causes ΔB_i to exceed ΔB_o even further. This nonlinear process continues until $\dot{B}_i$ reaches peak (when $B_i = 0$). Beyond this point, $\dot{B}_i$ decreases; the peak of the factor $[1 - (B/B_s)^2]$, *i.e.*, unity, moves radially outwards as time progresses. This peak reaches the outer edge when $[1 - (B_i/B_s)^2]$ is less than unity. By this time, the parabolic model has tended to equalize the distribution of B across the leg cross section, as compared with the time when $B_i = 0$. Thus, if a leg is initially at negative saturation and a positive MMF switches the leg to a partially switched state where B_i is around zero, the distribution of B across the leg cross section is nonuniform ($B_i > B_o$) for two reasons that are embedded in Eq. (24). The first reason is the factor $(H - H_0)$; the second reason is the factor $[1 - (B/B_s)^2]$. The second reason causes B to become more uniform at a later time during switching.

(3) In describing a leg model, it is assumed that the distribution of B appearing at a leg junction is uniform. The validity of this assumption depends on the path of flux closure in the rest of the core. If, for example, the leg under discussion is shunted by a short and wide leg, this assumption may be misleading. In this case, a higher change in B would occur in the inner edge of the shunting leg, so that the distribution of B at the leg junctions would be highly nonuniform.

(4) The leg model ignores flux leakage due to pole distribution on the surface of the leg. We know, however, that an asymmetric position of MMF drive will cause a pole distribution on the leg surface (see Report 1, pp. 128-138), and hence flux leakage will result. As concluded in Report 1, calculation of the leakage flux is too complex a problem to be practically worthwhile. If a leg is very long and thin, the flux leakage may make the leg model invalid.

Additional limitations on the model for a variable-width leg are discussed next.

2. ADDITIONAL MODEL LIMITATIONS OF A VARIABLE-WIDTH LEG

Consider a variable-width leg of constant thickness h. The maximum residual flux level of the whole leg is equal to $B_r A^{min}$, where A^{min} is the constricting cross-sectional area. Throughout the leg, except at the constricting region, the leg is partially switched, *i.e.*, $|\phi| < \phi_r$. Depending on its history, this state may be soft (see Report 1, pp. 25-26 and pp. 48-50). The higher is the previously applied MMF, the larger the number of domains of reversed magnetization is, and the softer the state is. Unless previously driven slowly, a variable-width leg is most likely to be in a soft state; here is where difficulties lie. These difficulties stem from our lack of sufficient information about this complex state, and are listed as follows:

(1) We have discussed previously the general limitations of a leg model from the point of view of nonuniform distribution of B, assuming that the leg is initially in a hard (saturated) state. Some portions of a variable-width leg, on the other hand, are left in a soft state even after a CLEAR pulse. These portions are likely to be found along the longer switching paths of the leg. However, the soft state is characterized by a lower threshold; hence a lower H is needed for a given change in B. This factor, therefore, opposes the original effect of the path-length ratio in making $\Delta B_i > \Delta B_o$. The extent to which this factor makes B more uniform is still to be found.

(2) Static characteristics of a variable-width leg depend directly on soft threshold. We need to know more about soft threshold before we can calculate the static $\phi(F)$ loop of a variable-width leg.

(3) Elastic-switching models have been proposed in Report 1 (pp. 18-23) for a leg in saturation (*i.e.*, $|\phi| > \phi_r$), but not for a partially-switched leg. Here, again, the fact that a variable-width leg is unsaturated (unless biased by very high MMF, in which case surface poles should be accounted for) prevents us from calculating elastic switching.

(4) Consider the parabolic model for inelastic switching in a constant-width leg, Eq. (23). In looking for a similar model for a variable-width leg, we encounter the difficulty of the dependence of F_0 on the softness of the state.

Thus, the only switching parameter of a variable-width leg left to be calculated at this time is the inelastic switching coefficient ρ. In order to calculate ρ of a variable-width leg, we must first determine the equi-F lines and flow lines. The general solution to this problem is very complex; however, solutions in some special cases are feasible. As an introduction to the problem, let us first consider a variable-width leg made of *linear* material.

3. VARIABLE-WIDTH LEG OF LINEAR MATERIAL

For linear material, the relation

$$B = \mu H \tag{26}$$

holds, where the permeability μ is constant. The problem of determining the distribution of B and H is a classical two-dimensional field problem that may be solved by graphical, numerical, and (sometimes) analytical methods. An excellent coverage of this topic can be found in several textbooks.[4,5]

In linear material, reluctance $\mathcal{R}$ is defined as

$$\mathcal{R} = \frac{F}{\phi} \quad . \tag{27}$$

It should be emphasized that the term reluctance is entirely different from ρ or ρ^{-1}. The units of reluctance are (turn^2/ohm second), whereas the units of ρ are (ohm/turn^2).

Since our prime interest in this work is focused on nonlinear square-loop material, rather than on linear material, it is felt that a detailed calculation of $\mathcal{R}$ of a variable-width leg should be deferred to an appendix. A general expression for $\mathcal{R}$ of a leg, whose boundaries can be described by orthogonal curvilinear coordinates, is derived in Appendix B. Examples of typical problems are also included in this appendix.

4. ρ OF A TAPERED LEG

We now come back to the original problem, and assume a square-loop ferromagnetic material. Calculating ρ for a variable-width leg of general shape is much more complex than calculating $\mathcal{R}$, because of the dependence of ρ on B [Eq. (24)]. Suppose that the effect of the flux-closure path on the distribution of B at the leg junctions is negligible. If H were invariant along each equi-F line, then, following Eq. (24), B would be uniformly distributed across the leg width, and the calculation of ρ would become much simpler. This condition is satisfied in the case of a tapered leg. Calculation of ρ for a leg of this shape is our next goal.

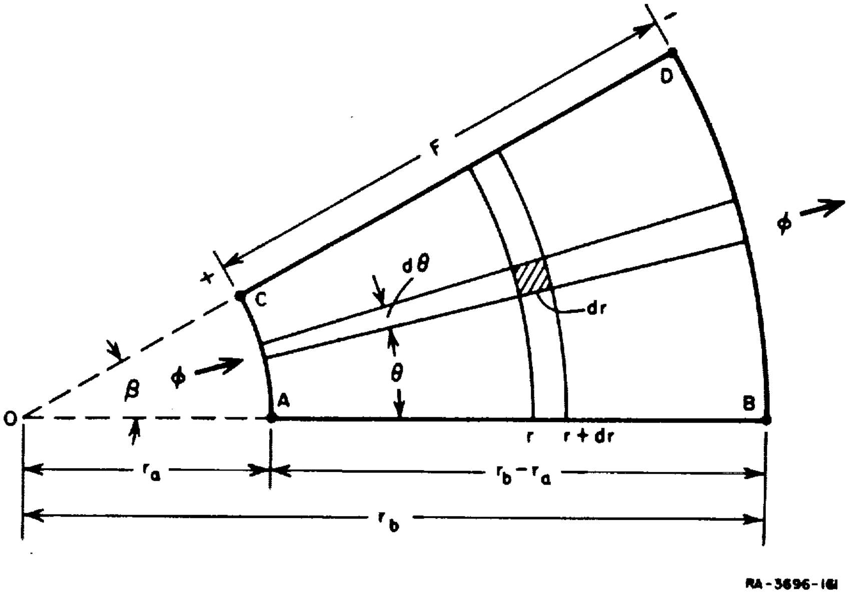

FIG. 3 A TAPERED LEG

The top view of a tapered leg of constant height h is shown in Fig. 3. The leg edges, A-B and C-D, are orthogonal to the leg ends, A-C and B-D. The geometry of the leg may be expressed in terms of three parameters: angle β, small radius r_a, and large radius r_b (the leg length is equal to $r_b - r_a$). We shall assume that the band near the constricting end A-C is not driven far into saturation.

We now divide the leg into curvilinear squares. The equi-F lines fall on concentric circles and the flow lines are radial. The radial lines meet at the center of the circles, Point 0. Each curvilinear square is the top view of a leg element of thickness h, length dr, width $rd\theta$, and cross-sectional area $hrd\theta$. Multiplying Eq. (24) by $hrd\theta$, and substituting $H = dF/dr$, we get

$$\dot{B}hrd\theta = \zeta_p \frac{hrd\theta}{dr}\left(1 - \frac{B^2}{B_s^2}\right)(dF - H_0 dr) \quad . \tag{28}$$

The term $(dF - H_0 dr)$ is the excess MMF applied to the leg element, and the term $\dot{B}hrd\theta$ is the resulting $\dot{\phi}$ in the element. Following the relation $\dot{\phi} = \rho F_{ex}$, ρ of the leg element, denoted by $\Delta\rho$, is

$$\Delta\rho = \zeta_p \frac{hrd\theta}{dr}\left(1 - \frac{B^2}{B_s^2}\right) \quad . \tag{29}$$

The inelastic-switching coefficient of a larger arc-shaped leg element, obtained by moving the previous element at a constant value of r from $\theta = 0$ to $\theta = \beta$, is

$$\delta\rho = \int_0^\beta \Delta\rho = \zeta_p h\beta \frac{r\left[1 - \left(\dfrac{\phi}{B_s h\beta}\right)^2 \dfrac{1}{r^2}\right]}{dr} \quad . \tag{30}$$

Note that B and B_s of Eq. (29) have been multiplied by the cross-sectional area, $h\beta r$. Since the whole leg is composed of a series of such elements, the over-all ρ of the tapered leg is

$$\rho_t = \frac{1}{\displaystyle\int_{r_a}^{r_b} \frac{1}{\delta\rho}} = \frac{2\zeta_p h\beta}{\ln\left[\dfrac{r_b^2 - \left(\dfrac{\phi}{B_s h\beta}\right)^2}{r_a^2 - \left(\dfrac{\phi}{B_s h\beta}\right)^2}\right]} \quad . \tag{31}$$

The value of ϕ_s of the leg is determined by the constricting area, *i.e.*,

$$\phi_s = B_s h r_a \beta \quad . \tag{32}$$

Substituting Eq. (32) into Eq. (31), we obtain

$$\rho_t = \frac{2\zeta_p h\beta}{ln\left[\frac{\left(\frac{r_b}{r_a}\right)^2 - \left(\frac{\phi}{\phi_s}\right)^2}{1 - \left(\frac{\phi}{\phi_s}\right)^2}\right]} . \tag{33}$$

We conclude that for a given ϕ_s, ρ_t is proportional to the angle β. We also conclude that ρ_t is symmetrical with respect to ϕ, reaching a peak, ρ_{tp}, at $\phi = 0$. The expression for ρ_t of Eq. (33) can be written in a more general form as a product of ρ_{tp} and some function η_t that describes the variation of ρ with (ϕ/ϕ_s). Thus,

$$\rho_t = \rho_{tp} \cdot \eta_t \tag{34}$$

where

$$\rho_{tp} = \frac{\zeta_p h\beta}{ln\left(\frac{r_b}{r_a}\right)} \tag{35}$$

and

$$\eta_t = \frac{2\ ln\left(\frac{r_b}{r_a}\right)}{ln\left[\frac{\left(\frac{r_b}{r_a}\right)^2 - \left(\frac{\phi}{\phi_s}\right)^2}{1 - \left(\frac{\phi}{\phi_s}\right)^2}\right]} . \tag{36}$$

Let us now compare these results with ρ of a constant-width leg that has the same value of ϕ_s and comparable dimensions: the same height h, width $w = \beta r_a$ (the constricting width of the tapered leg), and length $l = r_b - r_a$. For this constant-width leg, following the relations $\rho_p = \zeta_p A/l$ and $\rho = \rho_p[1 - (\phi/\phi_s)^2]$, we obtain

$$\rho = \rho_p \cdot \eta \tag{37}$$

where

$$\rho_p = \frac{\zeta_p h\beta}{\dfrac{r_b}{r_a} - 1} \tag{38}$$

and

$$\eta = 1 - \left(\frac{\phi}{\phi_s}\right)^2 \quad . \tag{39}$$

Equations (37), (38), and (39) could also have been derived directly from Eq. (33). Referring to Fig. 3, let us imagine that both r_a and r_b increase indefinitely, while at the same time $r_b - r_a = l$ and $r_a\beta = w$ are kept constant. Substitution of the resulting relation $(r_b/r_a) = 1 + (l/w)\beta$ into Eq. (33), and letting $\beta \to 0$, we obtain (using L'Hospital's rule) Eqs. (37) through (39). Note that the tapered leg has become rectangular.

In comparing Eq. (35) to Eq. (38), and Eq. (36) to Eq. (39), since $r_b > r_a$, we conclude that $(\rho_{tp}/\rho_p) > 1$ and that $(\eta_t/\eta) \geq 1$; thus, $(\rho_t/\rho) > 1$ for any value of ϕ/ϕ_s. A more detailed comparison of these parameters is shown in Figs. 4, 5, and 6. In Fig. 4, calculated ρ_{tp} and ρ_p (both in units

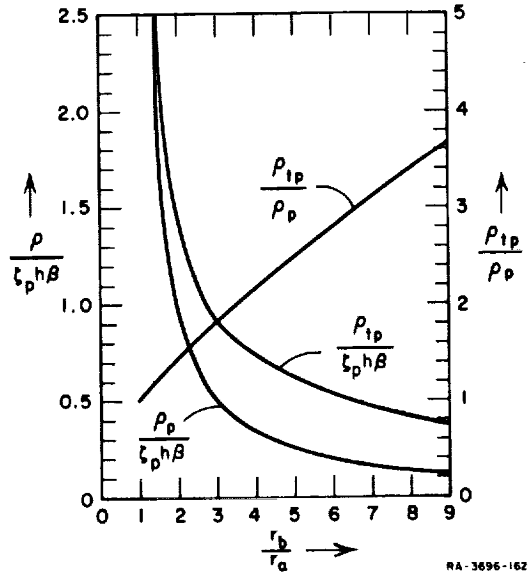

FIG. 4 EFFECT OF r_b/r_a ON ρ_{tp} AND ρ_p

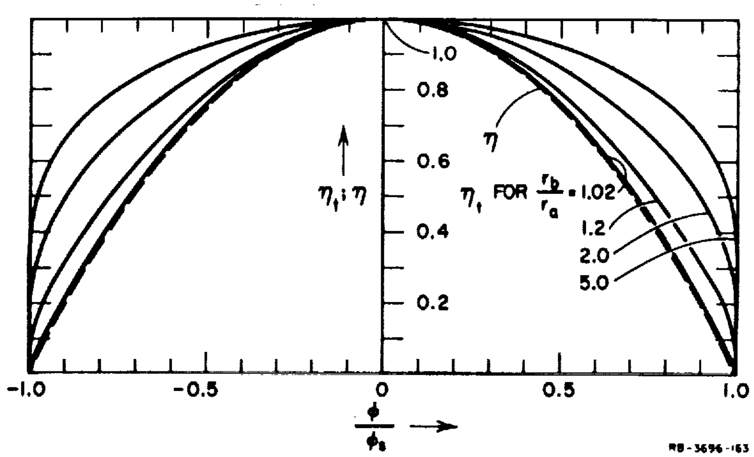

FIG. 5 EFFECT OF r_b/r_a ON η_t AND η vs. ϕ/ϕ_s

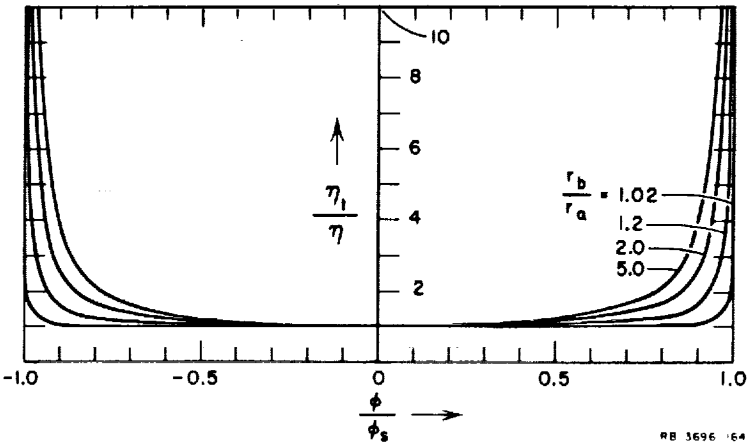

FIG. 6 η_t/η vs. ϕ/ϕ_s WITH r_b/r_a AS A PARAMETER of $\zeta_p h\beta$) and the ratio ρ_{tp}/ρ_p are plotted versus r_b/r_a. In Fig. 5, calculated η_t (for various values of r_b/r_a) and η are plotted versus ϕ/ϕ_s. In Fig. 6, the ratio η_t/η is plotted versus ϕ/ϕ_s, with r_b/r_a as a parameter.

5. SUMMARY

The inelastic coefficient ρ of a leg, which is a proportionality factor in the expression for $\dot{\phi}(F)$, is a product of two factors. The first factor, ρ_p, is a function of the material properties and the geometry of the leg. The second factor, η, is a function of the normalized flux level and, if the cross-sectional area of the leg is not constant, also a function of the leg geometry. If the constricting end of a tapered leg remains unchanged as the other end is enlarged, then flux switching becomes easier and ρ_t increases. This increase in ρ_t is manifested by the increase in both ρ_{tp} and η_t.

C. AVERAGE VALUES OF ρ

1. INTRODUCTION

Average values of ρ were calculated in Report 1 (pp. 28-31). The only reason for using an average, constant value of ρ is to simplify calculations where ρ is involved. As indicated in Report 1 (p. 54), the use of average ρ instead of $\rho(\phi)$ may be a good approximation only when $\Delta\phi$ is calculated, not $\dot{\phi}(t)$ or $\phi(t)$, because calculation of $\Delta\phi$ involves time integration of $\dot{\phi}(t)$.

Two kinds of average ρ were distinguished in Report 1: time-averaged ρ, $\bar{\rho}$ [Eq. (C-7), p. 192], and flux-averaged ρ, $\rho_{\phi,\mathrm{av}}$ [Eq. (C-11), p. 192]. From here on we shall retain the symbol $\bar{\rho}$, but replace $\rho_{\phi,\mathrm{av}}$ by ρ_{av} for the sake of brevity. Our first goal will be to examine the meanings of $\bar{\rho}$ and ρ_{av}, and consider their usefulness.

In Report 1, we calculated $\bar{\rho}$ and ρ_{av}, assuming a complete switching. In many applications, flux switching is only partial, *i.e.*, the flux varies from a CLEAR state to some final value ϕ_f between $-\phi_r$ and $+\phi_s$. In these cases, an average value of ρ is not constant, but rather a function of ϕ_f. Our second objective is to calculate the average ρ for a leg whose flux level varies from $-\phi_r$ to ϕ_f, assuming a parabolic switching model for the material [Eq. (24)]. We shall perform this calculation for a constant-width leg and a tapered leg.

2. $\bar{\rho}$ AND ρ_{av}

Suppose that an MMF pulse F of an arbitrary shape is applied along a leg in the positive direction. The resulting inelastic flux change is $\Delta\phi = \phi_f - \phi_0$, where ϕ_0 is the initial flux and ϕ_f is the final flux. The inelastic-switching coefficient ρ varies during the switching of ϕ. In an attempt to average ρ over $\Delta\phi$, we consider two kinds of averaging process: (1) averaging ρ itself, and (2) averaging the inverse of ρ. The flux-averaged ρ is defined as

$$\rho_{av} = \frac{1}{\Delta\phi}\int_0^{\Delta\phi} \rho d\phi \quad . \tag{40}$$

The flux-averaged $(1/\rho)$ is defined as

$$\left(\frac{1}{\rho}\right)_{av} = \frac{1}{\Delta\phi}\int_0^{\Delta\phi} \left(\frac{1}{\rho}\right) d\phi \quad . \tag{41}$$

We now want to determine which of these average quantities may be applied in calculation of flux switching. Following the basic definition of ρ [*cf.* Eq. (23)], $\dot{\phi} = \rho F_{ex}$, where F_{ex} $(= F - F_0)$ is the excess MMF over the dynamic threshold. Based on this relation,

$$\int_0^{\Delta\phi} \left(\frac{1}{\rho}\right) d\phi = \int_0^{\tau} F_{ex} dt \tag{42}$$

where τ is the switching time. Note that if the switching is time-limited (as opposed to flux-limited), then τ is the time during which $F > F_0$. Because of its dimensions, the term $\int_0^{\tau} F_{ex} dt$ is called "excess charge-turns," or in short, "excess charge." Combining Eqs. (41) and (42),

$$\Delta\phi = \frac{1}{\left(\frac{1}{\rho}\right)_{av}} \int_0^{\tau} F_{ex} dt \quad . \tag{43}$$

Thus, in order to compute $\Delta\phi$ that results from a drive of a given amount of excess charge, we have to use the flux-averaged value of $(1/\rho)$, Eq. (41). On the other hand, the flux-averaged ρ [Eq. (40)] does not relate F_{ex} to the resulting change in ϕ. We, therefore, conclude that $(1/\rho)_{av}$ (and not ρ_{av}) is the useful average value for calculation of ρ.

In Report 1 (Appendix C), $\bar{\rho}$ was calculated for switching from $\phi_0 = -\phi_r$ to $\phi_f = +\phi_r$ due to a constant F. Examination of Eq. (C-8) [Report 1, p. 192] leads to a more general definition of $\bar{\rho}$, *i.e.*,

$$\bar{\rho} = \frac{\Delta\phi}{\int_0^{\tau} F_{ex} dt} \quad . \tag{44}$$

A comparison between Eq. (43) and Eq. (44) reveals that $1/\bar{\rho} = (1/\rho)_{av}$. Following Eq. (41), we conclude that

$$\bar{\rho} = \frac{\Delta\phi}{\int_0^{\Delta\phi} \left(\frac{1}{\rho}\right) d\phi} \quad . \tag{45}$$

In Report 1, $\bar{\rho}$ was called "time-averaged ρ," yet Eq. (45) indicates that $\bar{\rho}$ is the inverse of the flux-averaged $(1/\rho)$. We observe, however, that Eq. (44) may be written as

$$\Delta\phi = \bar{\rho}\bar{F}_{ex}\tau \tag{46}$$

where $\bar{F}_{ex}$ is the time-averaged F_{ex}. For this reason we shall continue to call $\bar{\rho}$ "time-averaged ρ," although its evaluation will be based on Eq. (45).

We have concluded that $\bar{\rho}$, not ρ_{av}, is the useful parameter. However, if ρ does not vary too much during switching, then to a rough approximation, $1/\rho_{av} \cong (1/\rho)_{av}$. Under this condition, $\bar{\rho}$ may be approximated by ρ_{av} (*cf.* Report 1, p. 29).

3. $\bar{\rho}$ OF CONSTANT-WIDTH AND TAPERED LEGS

We shall now use Eq. (45) in order to calculate $\bar{\rho}$ of a constant-width leg and $\bar{\rho}$ of a tapered leg (to be denoted by $\bar{\rho}_t$). But first, let us rewrite Eq. (45) in terms of normalized flux u, where $u = \phi/\phi_s$. In addition, initial value of u, u_0 $(= \phi_0/\phi_s)$, and final value of u, u_f $(= \phi_f/\phi_s)$, will be spelled out. Thus, Eq. (45) is rewritten as

$$\bar{\rho} = \frac{u_f - u_0}{\int_{u_0}^{u_f} \left[\frac{1}{\rho(u)}\right] du} \quad . \tag{47}$$

a. CALCULATION OF $\bar{\rho}$

The parabolic model for ρ of a constant-width leg is [*cf.* Eq. (23)]

$$\rho = \rho_p(1 - u^2) \quad . \tag{48}$$

Substitution of Eq. (48) into Eq. (47) gives

$$\bar{\rho} = \rho_p \frac{u_f - u_0}{\tanh^{-1} u_f - \tanh^{-1} u_0} \quad . \tag{49}$$

Let us examine Eq. (49). For $-u_0 = u_f = u_r$ $(= \phi_r/\phi_s)$, Eq. (49) is reduced to $\bar{\rho} = \rho_p u_r/\tanh^{-1} u_r$, which, as expected, is identical with $\bar{\rho}$ for similar switching conditions [Report 1, Eq. (43), p. 28]. For $u_0 = u_f = -u_r$ (no inelastic switching), Eq. (49) is reduced to $\bar{\rho} = \rho_p(1 - u_r^2)$ by using L'Hospital's rule; this result agrees with the parabolic model for ρ [Eq. (48)], in which $u = -u_r$. We note that $\bar{\rho} \rightarrow 0$ as $u_f \rightarrow 1$. This can be explained by referring to Fig. 30, Report 1, and to Eq. (44). As $u_f \rightarrow 1$, $\tau \rightarrow \infty$, and since $\Delta\phi$ is finite, $\bar{\rho} \rightarrow 0$.

In most cases, a leg is initially in a CLEAR state, so that $u_0 = -u_r$. Under this condition, Eq. (49) is modified to the following.

$$\bar{\rho} = \rho_p \frac{u_f + u_r}{\tanh^{-1} u_f + \tanh^{-1} u_r} \quad . \tag{49a}$$

Note that $\bar{\rho}(u_f)$ reaches a maximum. Assuming that u_r (= ϕ_r/ϕ_s) = 0.9, $\bar{\rho}/\rho_p$ *vs.* u_f (= ϕ_f/ϕ_s) is calculated from Eq. (49a) and plotted in Fig. 7. A maximum value of $(\bar{\rho}/\rho_p)$ = 0.695 is reached at $u_f \cong 0.55$. Since $u_0 = -u_r$, there is no physical meaning to the plot where $u_f < -u_r$; hence, the region $-1 \leq u_f \leq -0.9$ is marked by dotted line.

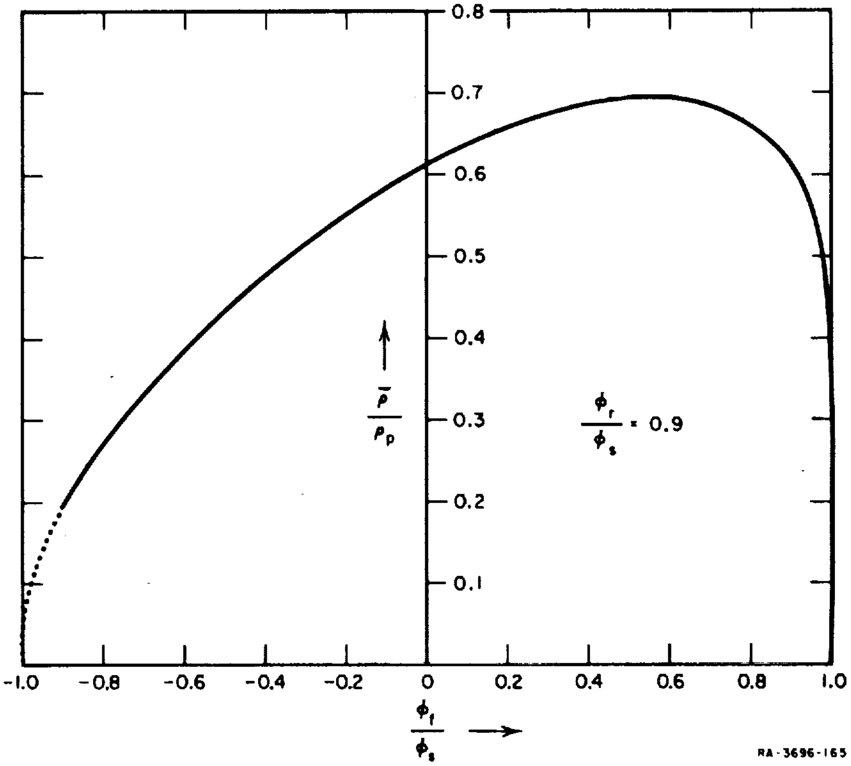

FIG. 7 $\bar{\rho}/\rho_p$ vs. ϕ_f/ϕ_s FOR A CONSTANT-WIDTH LEG

The value of u_r in Eq. (49a) must be known *a priori* in order to calculate $\bar{\rho}$. Unfortunately, u_r may vary (around ~0.9) among different materials. The effect of u_r on $\bar{\rho}$ is shown in Fig. 8, where $\bar{\rho}/\rho_p$ is plotted *vs.* u_f with u_r as a parameter. As u_r increases from 0.80 to 0.98, the maximum value of $(\bar{\rho}/\rho_p)$ decreases from 0.79 to 0.53 in the range $0.48 \leq u_f \leq 0.7$. Where dotted lines are drawn, the calculated curves have no physical meaning.

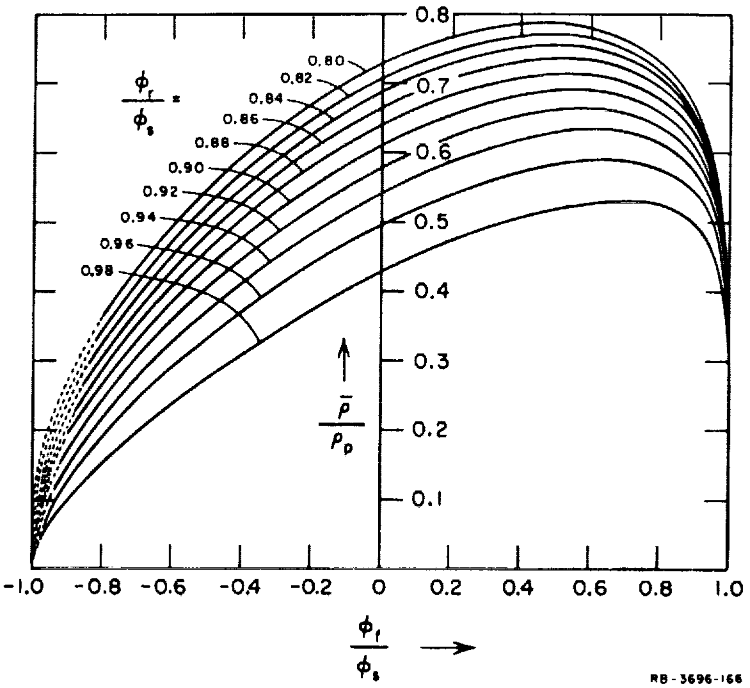

FIG. 8 PLOTS OF $\bar\rho/\rho_p$ vs. ϕ_f/ϕ_s WITH ϕ_r/ϕ_s AS A PARAMETER (Constant-Width Leg)

b. CALCULATION OF $\bar\rho_t$

Substitution of Eq. (33) into Eq. (47) (*cf*. Appendix C) results in the following expression, assuming that $u_0 = -u_r$.

$$\bar\rho_t = 2\zeta_p h\beta \frac{u_f + u_r}{\ln\left[\frac{(c+u_f)^{c+u_f}(1-u_f)^{1-u_f}(c+u_r)^{c+u_r}(1-u_r)^{1-u_r}}{(c-u_f)^{c-u_f}(1+u_f)^{1+u_f}(c-u_r)^{c-u_r}(1+u_r)^{1+u_r}}\right]} \qquad (50)$$

where

$$c = \frac{r_b}{r_a} \quad .$$

As $u_f \to 1$, $\bar\rho_t \to 0$ (due to infinite switching time). For the case in which $-u_0 = u_f = u_r$, Eq. (50) is reduced to

$$\bar{\rho}_t = 2\zeta_p h\beta \frac{u_r}{\ln\left[\dfrac{(c+u_r)^{c+u_r}(1-u_r)^{1-u_r}}{(c-u_r)^{c-u_r}(1+u_r)^{1+u_r}}\right]} \tag{50a}$$

and for $u_r = 0.9$ it is further reduced to

$$\bar{\rho}_t = \frac{1.8\zeta_p h\beta}{\ln\left[0.2344\,\dfrac{(c+0.9)^{c+0.9}}{(c-0.9)^{c-0.9}}\right]} \quad . \tag{50b}$$

Let us check Eq. (50) by letting $r_a \to \infty$ and $r_b \to \infty$ in such a way that l ($= r_b - r_a$) and w ($= r_a\beta$) are kept constant. Substituting $c = 1 + (l/w)\beta$ into Eq. (50) and letting $\beta \to 0$, the use of L'Hospital's rule results in $\bar{\rho}_t$ being equal to $\bar{\rho}$ of a constant-width leg, Eq. (49), as expected.

Assuming that $u_r = 0.9$, $\bar{\rho}_t/\rho_{tp}$ versus ϕ_f/ϕ_s is calculated from Eq. (50) and plotted in Fig. 9 for different values of c ($= r_b/r_a$). As c increases, $\bar{\rho}_t/\rho_{tp}$ increases due to the increase of η_t with c (*cf.* in Fig. 5).

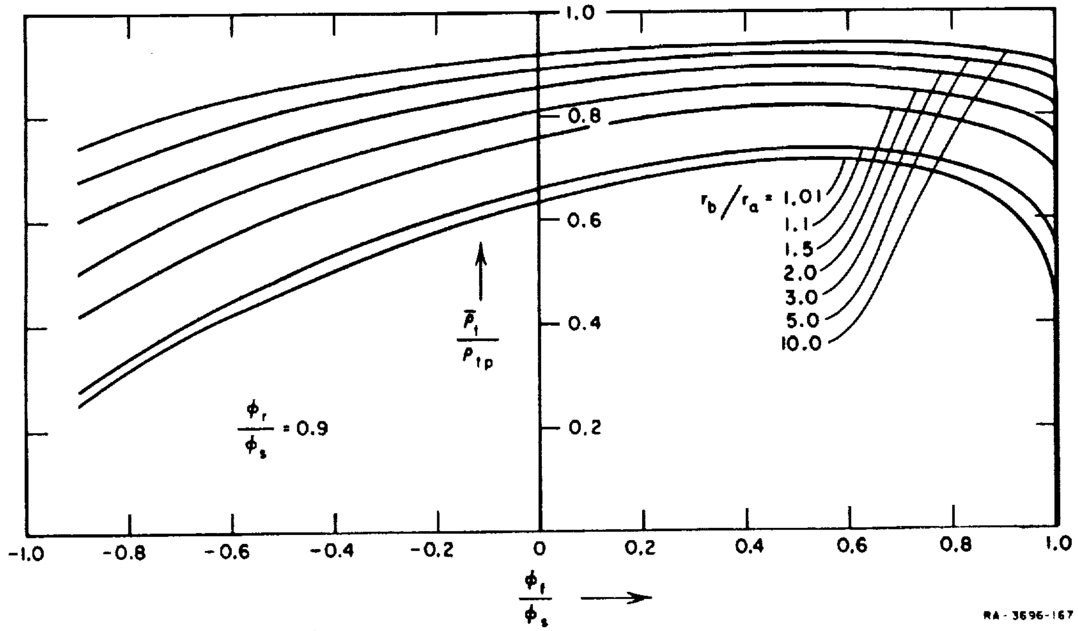

FIG. 9 $\bar{\rho}_t/\rho_{tp}$ vs. ϕ_f/ϕ_s WITH r_b/r_a AS A PARAMETER (Tapered Leg)

4. SUMMARY

Compared with flux-averaged ρ (denoted by ρ_{av}), time-averaged ρ (denoted by $\bar{\rho}$) is essentially the inverse of flux-averaged $(1/\rho)$. In calculation of $\Delta\phi$ due to an excess charge $\int_0^T F_{ex}dt$, $\bar{\rho}$ (and not ρ_{av}) is the useful parameter. If ρ does not change by a relatively large amount during switching, $\bar{\rho}$ may be approximated by ρ_{av}.

Calculated plots of $\bar{\rho}/\rho_p$ *vs.* ϕ_f/ϕ_s of a constant-width leg are shown in Fig. 8 for various values of ϕ_r/ϕ_s. Calculated plots of $\bar{\rho}_t/\rho_{tp}$ *vs.* ϕ_f/ϕ_s of a tapered leg are shown in Fig. 9 for various values of r_b/r_a.

D. FLUX DIVISION IN A SATURABLE CORE

1. INTRODUCTION

The problem of flux division[6] (see Report 1, pp. 75-85) is briefly as follows: Magnetomotive force *NI* is applied to one leg in a three-leg core, and the resulting $\Delta\phi$ in the driven leg is divided into the other two legs. Experimental data show that the ratio between the net amounts of $\Delta\phi$ in the two legs is far from being equal to the inverse of their path-length ratio. The question of why this is so and how to calculate such a division of flux in various types of multipath cores presents itself.

Multipath cores may be classified by whether or not all legs in the core can be brought to a saturation residual state, *i.e.*, to $\phi = \pm\phi_r$. We shall thereby distinguish between saturable and nonsaturable cores. Two extreme cases of such a classification are the Laddic and the shaped MAD (see Report 1, Fig. 1, p. 2).

In the Laddic, all legs have equal cross-sectional area; thus, it is impossible to have residual states of $|\phi| = \phi_r$ in all legs simultaneously. For example, if in two legs of a two-hole Laddic (Report 1, Fig. 1, p. 2) $\phi = \phi_r$, then in the third leg, $\phi = 0$. To illustrate another example refer to Fig. 94 of Report 1 (p. 99), in which a three-hole Laddic is shown. Although $|\phi| = \phi_r$ in Legs 1, 2, 3, and 4, Leg *m* (comprised of the two horizontal middle legs) is in a demagnetized state of $\phi = 0$. Note that the flux level in Leg *m* (or the third leg in the previous example) may certainly be other than zero, but then $|\phi| \neq \phi_r$ in the other legs. We thus conclude that it is impossible to bring a Laddic (of any number of holes) to a residual state in which all legs are in a CLEAR state, $|\phi| = \phi_r$. A Laddic is, therefore, a nonsaturable core. The leg(s) in a partially-switched state of $|\phi| \neq \phi_r$ may have a soft threshold, which is a complex phenomenon (*cf.* Report 1, pp. 48-50). Since flux division is highly dependent on soft threshold, calculation of flux division in a Laddic is a rather difficult task. Experimental data on flux division in a two-hole Laddic was reported in Refs. 6 and 7, but no attempt was made to explain this phenomenon.

In a MAD (later, Fig. 42), leg cross sections are so shaped that it is possible to bring all legs to a CLEAR state, $|\phi| = \phi_r$. This shaped MAD is, therefore, a saturable core. With no legs initially in a soft state, the analysis of the flux division is easier than in the case of a Laddic. Calculation of flux division in a saturable core was first reported in Ref. 8, but was incomplete for the following reasons (*cf.* Report 1, pp. 153-154): First, a square-root parabolic model for ρ was used; although leading to simpler mathematics, this model is less accurate than the parabolic model for ρ. Second, it was unjustifiably assumed that H in each leg is constant during the switching time. Third, rather than being solved for, the values of H in the two parallel legs were included as parameters in the final expression for flux division; furthermore, the applied MMF to the third (main) leg and the parameters of the third leg were completely ignored. Fourth, no experimental verification was given.

Our objective here is to calculate flux division in a three-leg core as a function of leg parameters (assuming a parabolic model for ρ) and applied MMF, and to compare this calculation with experimental data. Lacking flux-switching models for a leg initially in a soft state, we cannot at the present time analyze flux division in a Laddic. We shall, therefore, narrow our scope in this report to calculate flux division in a saturable core whose legs are initially in a CLEAR state. However, in order to be more general, we shall assume that the output leg is loaded by resistance R_L across N_L turns; flux division in an unloaded core would later be determined as a special case of $(N_L^2/R_L) = 0$.

2. ASSUMPTIONS

The analysis of the flux division is based on the following assumptions (see Fig. 10):

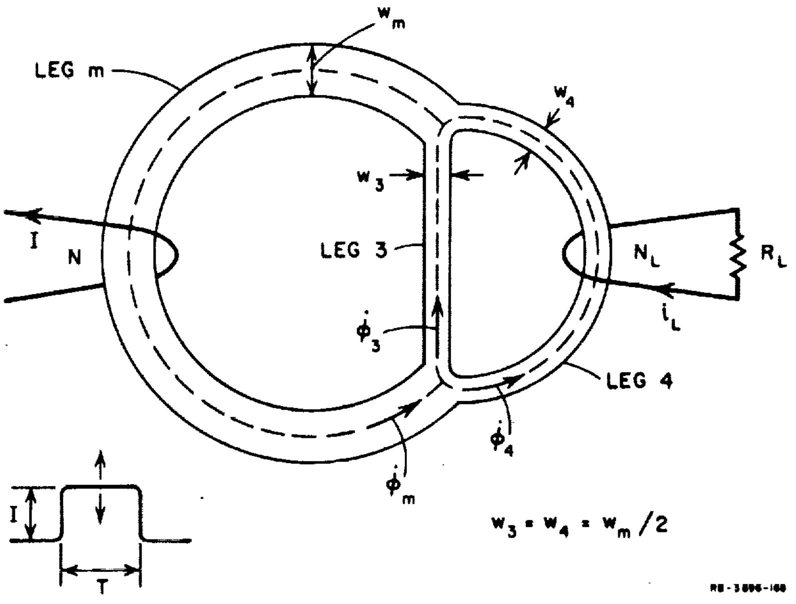

FIG. 10 FLUX DIVISION IN A SATURABLE THREE-LEG CORE

(1) The core is saturable. Thickness h is common to all legs, and $w_3 = w_4 = w_m/2$; hence

$$\phi_{rm} = 2\phi_{r3} = 2\phi_{r4} \equiv 2\phi_r \quad . \tag{51}$$

(2) Resistance R_L loads Leg 4 across N_L turns.

(3) The core is initially in a CLEAR state, *i.e.*,

$$\phi_m = -2\phi_r \ , \qquad \phi_3 = \phi_4 = -\phi_r \quad .$$

(4) The SET current pulse, applied to N turns on Leg m, is rectangular and of amplitude I and duration T so adjusted that the resulting flux change in Leg m, $\Delta\phi_m$, is equal to $2\phi_r$. [This assumption of time-limited switching could have been eliminated by assuming that NI was applied to Leg 1 of a five-leg core, as in Fig. 102(a) of Report 1 (p. 107). Such an alternative assumption would make the calculations more complicated without helping to understand the mechanism of flux division. We prefer, therefore, to maintain the assumption that NI is applied to Leg m and is adjusted both in magnitude and duration to yield $\Delta\phi_m = 2\phi_r$.]

(5) Since flux division is defined in terms of residual flux, we shall neglect the difference between $\Delta\phi_\epsilon$ during the rise of I and $\Delta\phi_\epsilon$ during the fall of I, and consider only inelastic switching.

3. CALCULATION OF FLUX-DIVISION RATIO

The method of calculating the flux division ($\Delta\phi_3/\Delta\phi_4$) is outlined as follows. An electrical-circuit analogue is drawn, and node and loop equations are written. The parabolic model for ρ, $\rho = \rho_p[1 - (\phi/\phi_s)^2]$, is employed in the equations for $\dot{\phi}$ of each leg. In this way, $\dot{\phi}_4$ gets to be smaller than $\dot{\phi}_3$ not only because $l_3 < l_4$ (and hence $H_4 < H_3$), but also because $\rho_3 > \rho_4$ during most of the switching time as a result of ϕ_3 being higher than ϕ_4. The flux division is expressed in terms of the final flux level of Leg 3, ϕ_{3f}. The remainder of this calculation is devoted to solution for ϕ_{3f} and to expression of $\Delta\phi_3/\Delta\phi_4$ in terms of NI and the leg parameters.

Based on Assumption (5), only the inelastic parameters F_0 and ρ of each leg are considered. The general electrical-circuit analogue for the loaded core in Fig. 10 (*cf*. Fig. 37, Report 1, p. 35) then becomes simpler, because all the "capacitors" are omitted. Since only the SET time is of interest, the electrical-circuit analogue is further simplified by omitting redundant components (*cf*. Report 1, Fig. 37, p. 35) as shown in Fig. 11. Since in an electrical-circuit analogue MMF is treated as "voltage" and $\dot{\phi}$ is treated as "current," the SET MMF, NI, appears as a "voltage source"

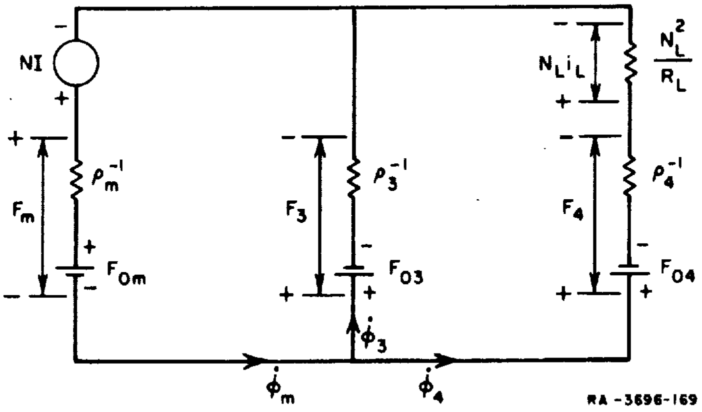

FIG. 11 ELECTRICAL-CIRCUIT ANALOGUE FOR A DRIVEN LOADED CORE

in series with Leg m, and the back MMF, $N_L i_L$, appears as a "voltage drop" across a "resistance" N_L^2/R_L in series with Leg 4. A special case is that of no load on Leg 4, *i.e.*, $N_L^2/R_L = 0$; this case can be obtained by letting either $R_L = \infty$ (open circuit) or $N_L = 0$ (no coupling).

One node equation and two loop equations are written by inspection of the electrical-circuit analogue, Fig. 11, as follows.

$$\dot{\phi}_m = \dot{\phi}_3 + \dot{\phi}_4 \quad , \tag{52}$$

$$NI = F_m + F_3 \quad , \tag{53}$$

and

$$F_4 = F_3 - \frac{N_L^2}{R_L}\dot{\phi}_4 \quad . \tag{54}$$

Using a parabolic model for ρ [*cf.* Eq. (23)],

$$\dot{\phi}_m = \rho_{mp}\left[1 - \left(\frac{\phi_m}{2\phi_s}\right)^2\right](F_m - F_{0m}) \quad , \tag{55}$$

$$\dot{\phi}_3 = \rho_{3p}\left[1 - \left(\frac{\phi_3}{\phi_s}\right)^2\right](F_3 - F_{03}) \quad , \tag{56}$$

and

$$\dot{\phi}_4 = \rho_{4p}\left[1 - \left(\frac{\phi_4}{\phi_s}\right)^2\right](F_4 - F_{04}) \quad . \tag{57}$$

Equations (52) through (57) contain six unknowns: $\dot{\phi}_m$, $\dot{\phi}_3$, $\dot{\phi}_4$, F_m, F_3, and F_4. Although these unknowns can be solved for, there is no need for these solutions in calculating the flux division, as will be shown next.

Let flux-division ratio be defined as

$$D = \frac{\Delta\phi_3}{\Delta\phi_4} \tag{58}$$

where $\Delta\phi_3$ and $\Delta\phi_4$ are the inelastic changes in flux in Legs 3 and 4, respectively. Since both of these legs are initially at $\phi = -\phi_r$,

$$\Delta\phi_3 = \phi_{3f} + \phi_r \tag{59}$$

and

$$\Delta\phi_4 = \phi_{4f} + \phi_r \tag{60}$$

where subscript f denotes final flux level. Following Eq. (52) and Assumption (4),

$$\Delta\phi_3 + \Delta\phi_4 = \Delta\phi_m = 2\phi_r \quad . \tag{61}$$

From the substitution of Eqs. (59) and (60) into Eq. (61), we conclude that

$$\phi_{3f} = -\phi_{4f} \quad . \tag{62}$$

Typical variations of ϕ versus F of the three legs during the SET time are plotted in Fig. 12, superimposed on the corresponding static $\phi(F)$ loops. These plots illustrate why $\phi_{3f} = -\phi_{4f}$, as stated in Eq. (62). Substituting Eqs. (59), (60), and (62) into Eq. (58), the flux-division ratio is found to be

$$D = \frac{1 + \dfrac{\phi_{3f}}{\phi_r}}{1 - \dfrac{\phi_{3f}}{\phi_r}} \quad . \tag{63}$$

Our next objective is to calculate ϕ_{3f}.

During the switching time T, ϕ_3 changes from $-\phi_r$ to ϕ_{3f} (*cf*. Fig. 12). Following Eq. (56),

$$\int_{-\phi_r}^{\phi_{3f}} \frac{d\phi_3}{1 - \left(\dfrac{\phi_3}{\phi_s}\right)^2} = \rho_{3p} \int_0^T (F_3 - F_{03})dt \quad . \tag{64}$$

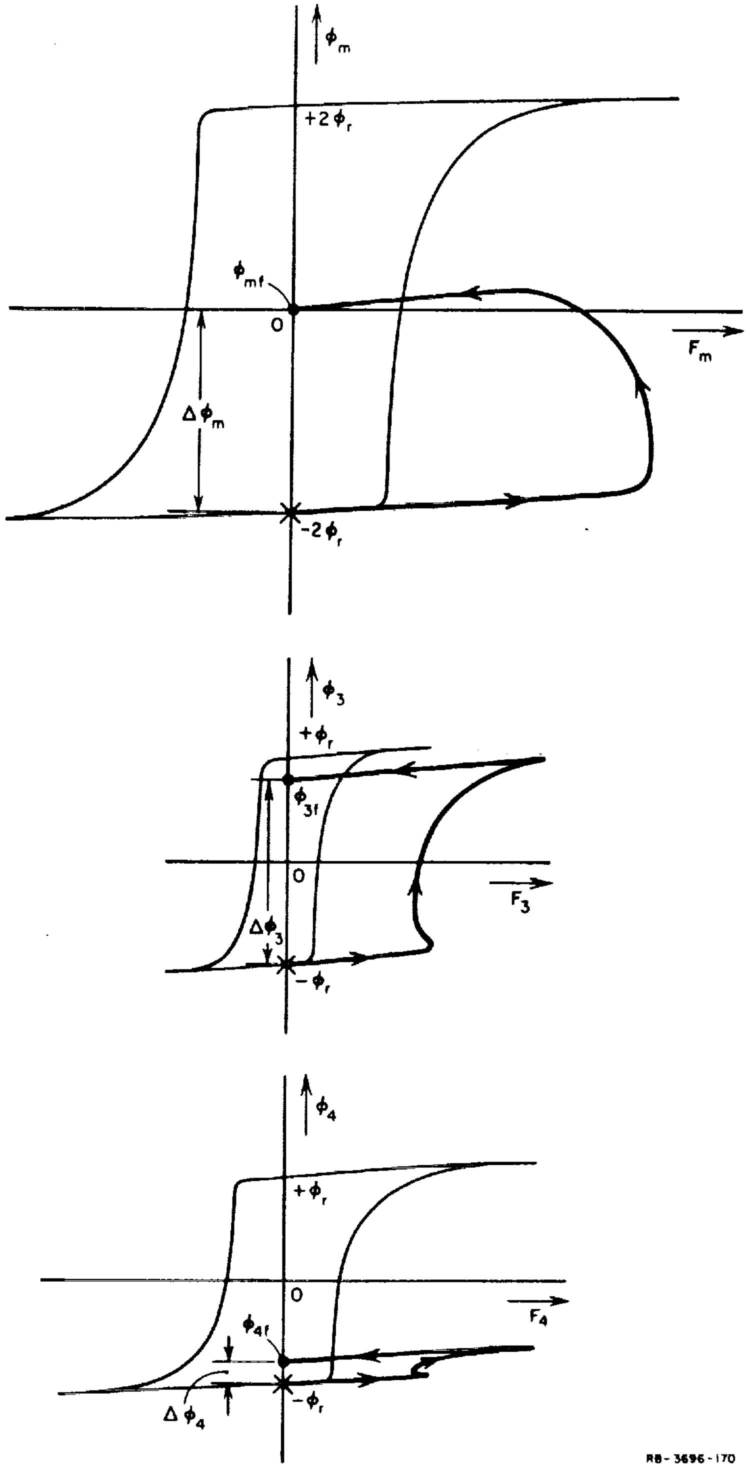

FIG. 12 VARIATION OF φ AND F OF EACH LEG IN FLUX-DIVISION EXPERIMENT

After integration, we get

$$\frac{\phi_{3f}}{\phi_s} = \tanh\left(\frac{\gamma}{2}\right) = \frac{e^{\gamma} - 1}{e^{\gamma} + 1} \tag{65}$$

in which

$$\gamma = 2\left[\frac{\rho_{3p}}{\phi_s}\int_0^T (F_3 - F_{03})dt - \tanh^{-1}\left(\frac{\phi_r}{\phi_s}\right)\right] . \tag{66}$$

Substitution of Eq. (65) into Eq. (63) gives

$$D = \frac{e^{\gamma} - \delta}{1 - \delta e^{\gamma}} \tag{67}$$

in which

$$\delta = \frac{1 - \dfrac{\phi_r}{\phi_s}}{1 + \dfrac{\phi_r}{\phi_s}} . \tag{68}$$

Calculation of γ is performed in Appendix D. It is shown there that

$$\gamma = p - q \; ln \; \delta \tag{69}$$

where

$$p = \frac{2\left(\dfrac{N_L^2}{R_L}\right)\rho_{3p}\rho_{4p}(NI - F_{0m} - F_{03})\left(\dfrac{\phi_r}{\phi_s} - \dfrac{\phi_{3f}}{\phi_s}\right)}{(NI - F_{0m})(\rho_{3p} + \rho_{4p}) - F_{04}\rho_{4p} - F_{03}\rho_{3p}} \tag{70}$$

and

$$q = \frac{(NI - F_{0m})(\rho_{3p} - \rho_{4p}) + F_{04}\rho_{4p}\left(1 + 2\dfrac{\rho_{3p}}{\rho_{mp}}\right) - F_{03}\rho_{3p}\left(1 + 2\dfrac{\rho_{4p}}{\rho_{mp}}\right)}{(NI - F_{0m})(\rho_{3p} + \rho_{4p}) - F_{04}\rho_{4p} - F_{03}\rho_{3p}} . \tag{71}$$

Note that the expressions for p and q have the same denominator. The value of q is independent of N_L^2/R_L and can be determined directly from Eq. (71), but the expression for p [Eq. (70)] includes the still-unknown term ϕ_{3f}/ϕ_s. By combining Eqs. (65) and (69), we obtain

$$\frac{\phi_{3f}}{\phi_s} = \tanh\left(\frac{p - q\ ln\ \delta}{2}\right) \quad . \tag{72}$$

After q is determined, substituting Eq. (72) into Eq. (70) results in a transcendental equation in p. A numerical solution for p can be obtained without any difficulty.

Substitution of Eq. (69) into Eq. (67) results in the final expression for the flux-division ratio:

$$D = \frac{e^p - \delta^{q+1}}{\delta^q - \delta e^p} \quad . \tag{73}$$

in which δ is expressed in Eq. (68), p is expressed transcendentally in Eqs. (70) and (72), and q is expressed in Eq. (71).

The larger the load N_L^2/R_L is, the smaller $\Delta\phi_4$ is, and hence D becomes higher. Mathematically, for the same values of NI and core parameters, if N_L^2/R_L increases, then p [Eq. (70)] increases as well; hence, e^p increases. An increase in e^p causes D [Eq. (73)] to increase because of an increase in the numerator and a decrease in the denominator.

4. FLUX-DIVISION RATIO UNDER SPECIAL CASES

The general expression for D [Eq. (73)] will now be reduced under special cases.

a. UNLOADED CORE

As explained before, if either $N_L = 0$ (no coupling) or $R_L = \infty$ (open circuit), Leg 4 is unloaded. Substituting $(N_L^2/R_L) = 0$ into Eq. (70), we find that $p = 0$. Recall that q is independent of N_L^2/R_L. The expression for D [Eq. (73)] is then reduced to

$$D_{NL} = \frac{1 - \delta^{q+1}}{\delta^{q} - \delta} \qquad (74)$$

where δ and q are expressed in Eqs. (68) and (71), respectively.

b. $D \to \infty$

When $\Delta\phi_4 \to 0$ and $\Delta\phi_3 > 0$, $D \to \infty$. This condition is physically realizable, since if l_4^{min}/l_3^{max} is large enough, *NI* may be so adjusted as to cause inelastic switching to occur in Leg 3 only. Since $\Delta\phi_3 + \Delta\phi_4 = 2\phi_r$ and $\Delta\phi_4 = 0$, then $\Delta\phi_3 = 2\phi_r$; hence, following Eq. (59), $\phi_{3f} = \phi_r$, and therefore, p [Eq. (70)] is zero. Substituting $D \to \infty$ *and* $p = 0$ into Eq. (73) results in $q = 1$. By equating q [Eq. (71)] to unity, the value of *NI* for which $D \to \infty$ is found to be

$$NI_{D\to\infty} = F_{0m} - F_{03}\frac{\rho_{3p}}{\rho_{mp}} + F_{04}\left(1 + \frac{\rho_{3p}}{\rho_{mp}}\right) . \qquad (75)$$

The expression for $NI_{D\to\infty}$ [Eq. (75)] is obviously not a function of the loading factor, N_L^2/R_L. This stems from having p, the only parameter where N_L^2/R_L has an effect, be equal to zero. The physical interpretation is rather simple: If $\Delta\phi_4 = 0$, the presence of a load on Leg 4 is irrelevant; hence, the magnitude of N_L^2/R_L has no effect. We also notice that $NI_{D\to\infty}$ is not a function of δ (since q is not a function of δ).

c. $NI \to \infty$

It was reported[6] that the flux-division ratio in a Laddic core approaches an asymptote as $NI \to \infty$. Let us now calculate the asymptotic value of D [Eq. (73)] for a saturable core.

As $NI \to \infty$, p and q [Eqs. (70) and (71)] are reduced to the following:

$$p_{NI\to\infty} = 2\frac{N_L^2}{R_L}\,\frac{\rho_{3p}\rho_{4p}}{\rho_{3p} + \rho_{4p}}\left(\frac{\phi_r}{\phi_s} - \frac{\phi_{3f}}{\phi_s}\right) \qquad (76)$$

and

$$q_{NI\to\infty} = \frac{\rho_{3p} - \rho_{4p}}{\rho_{3p} + \rho_{4p}} \quad . \tag{77}$$

After $q_{NI\to\infty}$ is determined, Eq. (72) is substituted into Eq. (76) and $p_{NI\to\infty}$ is solved for transcendentally. The values of $p_{NI\to\infty}$ and $q_{NI\to\infty}$ are then substituted into Eq. (73) to calculate $D_{NI\to\infty}$.

The larger the load N_L^2/R_L is, the larger is $p_{NI\to\infty}$ [Eq. (76)]; hence, following Eq. (73), the larger is $D_{NI\to\infty}$. The lowest $D_{NI\to\infty}$ is obtained when the core is not loaded. In the no-load case, $p = 0$ and $q_{NI\to\infty}$ [Eq. (77)] is substituted into Eq. (74) in order to calculate the asymptotic value for D_{NL}, *i.e.*,

$$D_{NL\,,NI\to\infty} = \frac{1 - \delta^{\left(\frac{2\rho_{3p}}{\rho_{3p}+\rho_{4p}}\right)}}{\delta^{\left(\frac{\rho_{3p}-\rho_{4p}}{\rho_{3p}+\rho_{4p}}\right)} - \delta} \tag{78}$$

d. $\delta \to 1$

Following Eq. (68), if $(\phi_r/\phi_s) \to 0$, then $\delta \to 1$. Before determining how D would be affected by the condition $\delta \to 1$, let us examine the physical meaning of having $(\phi_r/\phi_s) \to 0$.

Our analysis has been based on the assumption that initially $\phi_m = -2\phi_r$ and $\phi_3 = \phi_4 = -\phi_r$. In calculating $\Delta\phi$ of each leg, the parabolic model $\rho = \rho_p[1 - (\phi/\phi_s)^2]$ was employed. Suppose that ϕ_r is replaced by ϕ_{res}, where ϕ_{res} is an arbitrary residual flux level, so that initially $\phi_m = -2\phi_{res}$ and $\phi_3 = \phi_4 = -\phi_{res}$. If this initial state were obtained by slow, gentle switching, calculation of $\dot{\phi}$ in each leg may still follow Eq. (23). Under this condition, our analysis still holds, except that δ [Eq. (68)] is modified by replacing ϕ_r by ϕ_{res}; hence, $\delta \to 1$ when $(\phi_{res}/\phi_s) \to 0$. Modifying Assumption (4), $\Delta\phi_m = 2\phi_{res}$. The physical interpretation of the condition $(\phi_{res}/\phi_s) \to 0$ is, therefore, as follows: All legs switch by a very small amount near the demagnetized state of $\phi = 0$, and hence the inelastic-switching coefficient ρ of each leg remains practically constant at its peak value, as illustrated in Fig. 13. Mathematically,

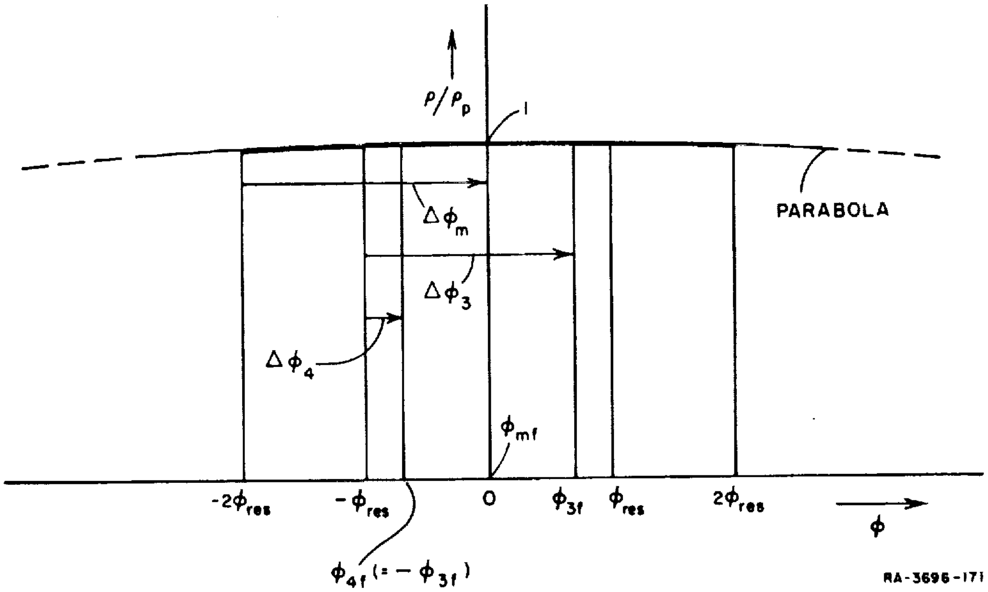

FIG. 13 ρ/ρ_p vs. ϕ OF EACH LEG WHEN $\delta \to 1$

each of the bracketed terms $[1 - (\phi_m/2\phi_s)^2]$, $[1 - (\phi_3/\phi_s)^2]$, and $[1 - (\phi_4/\phi_s)^2]$ in Eqs. (55), (56), and (57), is replaced by unity.

We now want to derive an expression for D under the condition that $\delta \to 1$. The transcendental solution to Eq. (D-21), as $(\phi_r/\phi_s) \to 0$, yields $\gamma \to 0$. Derivation of D from Eq. (67) and Eq. (D-21) is then based on L'Hospital's rule, which gives

$$\lim_{(\phi_r/\phi_s)\to 0} D = \frac{a_3 + a_2 + 2a_1}{a_3 - a_2}$$

where a_1, a_2, and a_3 are expressed in Eqs. (D-17), (D-18), and (D-19); thus,

$$D_{\delta\to 1} = \frac{\rho_{3p}}{\rho_{4p}/[1 + (\rho_{4p}N_L^2/R_L)]} \; \frac{(NI - F_{0m} - F_{03})\rho_{mp} + (F_{04} - F_{03})\rho_{4p}/[1 + (\rho_{4p}N_L^2/R_L)]}{(NI - F_{0m} - F_{04})\rho_{mp} + (F_{03} - F_{04})\rho_{3p}} \qquad (79)$$

It can be shown by simple calculation that Eq. (79) would result if constant ρ was assumed in the original equations [Eqs. (55) through (57)], *i.e.*, if $\rho_{\blacksquare} = \rho_{\blacksquare p}$, $\rho_3 = \rho_{3p}$, and $\rho_4 = \rho_{4p}$.

By equating the denominator of Eq. (79) to zero, the asymptotic expression for NI, for which $D_{\delta\rightarrow 1} \rightarrow \infty$, is determined. This expression is identical with the expression in Eq. (75), as expected, since the latter was shown to be independent of δ.

In the no-load case, $(N_L^2/R_L) = 0$, and Eq. (79) may be reduced to

$$D_{NL,\delta\rightarrow 1} = \left(\frac{\rho_{3p}}{\rho_{4p}}\right) \frac{(NI - F_{0\blacksquare} - F_{03})\rho_{\blacksquare p} + (F_{04} - F_{03})\rho_{4p}}{(NI - F_{0\blacksquare} - F_{04})\rho_{\blacksquare p} + (F_{03} - F_{04})\rho_{3p}} \quad . \tag{80}$$

When $NI \rightarrow \infty$, Eq. (79) may be reduced to

$$D_{\delta\rightarrow 1, NI\rightarrow\infty} = \frac{\rho_{3p}}{\rho_{4p}} [1 + (\rho_{4p} N_L^2/R_L)] \tag{81}$$

In the no-load case, Eq. (81) may be further reduced to

$$D_{NL,\delta\rightarrow 1, NI\rightarrow\infty} = \frac{\rho_{3p}}{\rho_{4p}} \quad . \tag{81a}$$

In conclusion, following Eq. (79), $D_{\delta\rightarrow 1}$ *vs.* NI is a hyperbola whose two asymptotes are defined by $NI = NI_{D\rightarrow\infty}$ [Eq. (75)] and by $D = D_{\delta\rightarrow 1, NI\rightarrow\infty}$ [Eq. (81)].

Let us summarize what we have found so far. D versus NI has been calculated in terms of leg parameters. We have seen that for a given value of NI, D decreases if the loading factor N_L^2/R_L decreases, reaching minimum when the core is unloaded, *i.e.*, when $N_L^2/R_L = 0$. The asymptotic value of NI, for which $D \rightarrow \infty$, was found to be independent of N_L^2/R_L or δ. The asymptotic value of D as $NI \rightarrow \infty$ decreases when N_L^2/R_L decreases, reaching minimum when the core is unloaded. This asymptotic value of D for $NI \rightarrow \infty$ also decreases as δ increases, reaching minimum when $\delta \rightarrow 1$, *i.e.*, when in each leg $\Delta\varphi$ is very small around $\varphi = 0$, and

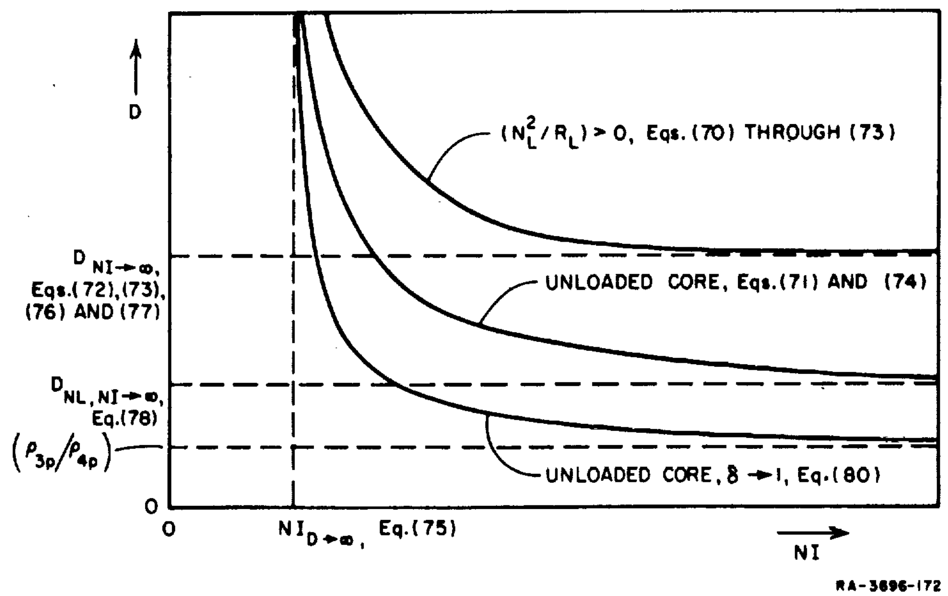

FIG. 14 D vs. NI IN THREE CASES

$\rho \simeq \rho_p$ = constant. All this is summarized graphically in Fig. 14 (assuming that the leg parameters are known) by sketching D versus NI in three cases: $N_L^2/R_L > 0$; $N_L^2/R_L = 0$; and $\delta \to 1$ in the case of $N_L^2/R_L = 0$.

5. EFFECTS OF LEG DIMENSIONS

Up to the present, calculation of flux division has been based on the leg parameters F_{0m}, F_{03}, F_{04}, ρ_{mp}, ρ_{3p}, and ρ_{4p}. Our next problem is to determine these parameters. Since the three legs are of the same material, the leg parameters differ from each other only because of differences in leg dimensions. Determination of the effect of the leg dimensions on D, a problem that was first introduced in connection with the Laddic,[6] amounts, therefore, to determination of the effect of the leg dimensions on the leg parameters. Before we determine this effect, let us improve our inelastic switching models in the region of low F.

a. LINEAR AND NONLINEAR REGIONS OF $\dot{B}_p$ VERSUS H

Material inelastic-switching properties have been discussed in Part B. Following Eq. (24), when $B = 0$, $\dot{B}$ reaches a peak value of

$$\dot{B}_p = \zeta_p (H - H_0) \quad . \tag{82}$$

A typical plot of $\dot{B}_p$ versus H is shown in Fig. 15. This plot is divided into two regions that have a common boundary at $H = H_B$: a linear region for $H \geq H_B$, and a nonlinear region for $H_0'' \leq H \leq H_B$. Since the parameters H_0 and ζ_p in Eq. (82) are assumed constant, Eq. (82) describes only the linear region of $\dot{B}_p$ versus H, where $H \geq H_B$. The extrapolated linear region intersects the H axis at $H = H_0$ with a slope of ζ_p.

The nonlinear region of $\dot{B}_p$ versus H may be approximately described by the following function:

$$\dot{B}_p = \kappa(H - H_0'')^{\nu} \quad . \tag{83}$$

Equation (83) follows the formulation $\dot{\phi} = b(F - F_0)^{1/a_3}$ described elsewhere.[9] For a given value of H, $\dot{B}_p(H)$ may be modified to a form similar to Eq. (82), *i.e.*,

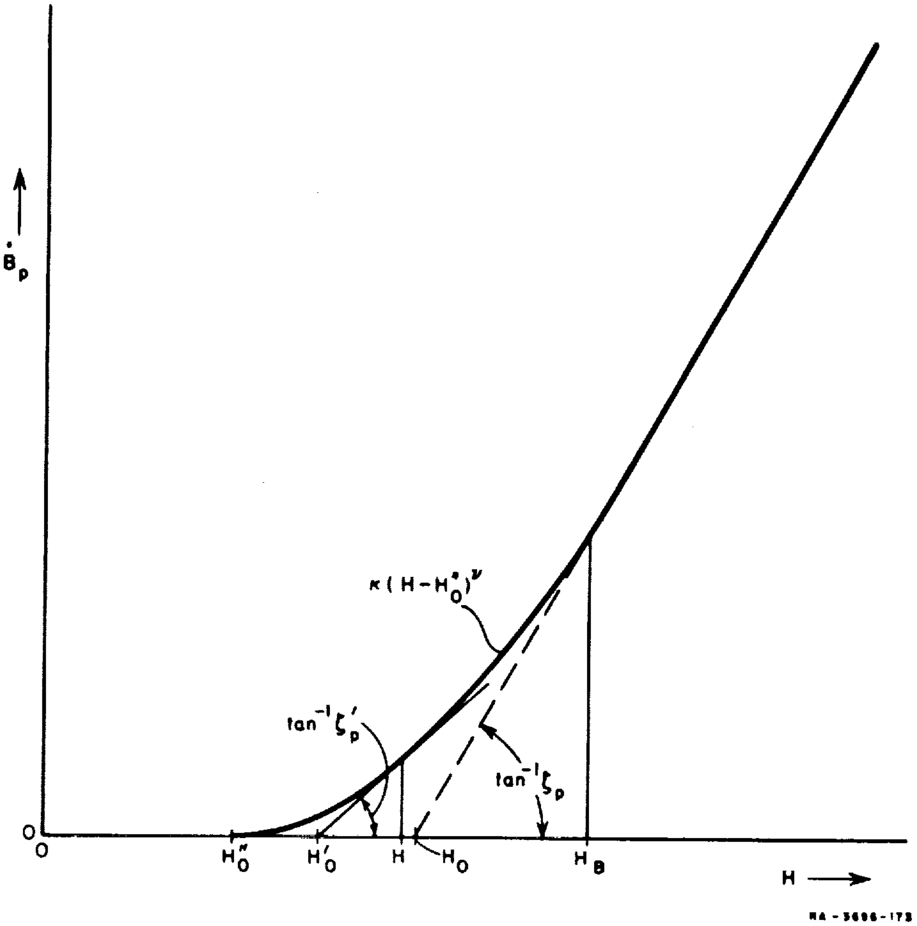

FIG. 15 $\dot{B}_p$ vs. H

$$\dot{B}_p = \zeta'_p(H - H'_0) \tag{84}$$

where H'_0 is the intersection with the H axis and ζ'_p is the slope of the tangent to the nonlinear portion of $\dot{B}_p$ versus H, as shown in Fig. 15. Note that H_0 and ζ_p may be looked at as a special case of H'_0 and ζ'_p in which $\dot{B}_p$ versus H is linear. Equating $d\dot{B}_p/dH$ of Eq. (83) to $d\dot{B}_p/dH$ of Eq. (84) gives

$$\zeta'_p = \kappa\nu(H - H''_0)^{\nu-1} \quad . \tag{85}$$

Substituting the expression for $\dot{B}_p$ [Eq. (83)] and ζ'_p [Eq. (85)] into Eq. (84) gives

$$H'_0 = H\left(1 - \frac{1}{\nu}\right) + \frac{H''_0}{\nu} \quad . \tag{86}$$

Inelastic switching may also occur for $H \leq H''_0$. However, the parabolic model for ζ [Eq. (24)] does not hold for this region of slow switching. Further investigation is needed in order to determine models for such a slow inelastic switching.

b. GEOMETRICAL RELATIONS

We now introduce leg dimensions in order to describe inelastic switching in terms of $\dot{\phi}_p$ versus F rather than $\dot{B}_p$ versus H. Integration of $\dot{B}$ across a leg cross section could not be expressed by a closed form. Because of this mathematical difficulty, we shall ignore the *variations* of H and B across the leg. Replacing H by F/l (for the sake of brevity, the symbol l^{av} is replaced by l) and $\dot{B}_p$ by $\dot{\phi}_p/A$, Eqs. (82) through (86) are transformed into the following: The linear region of $\dot{\phi}_p$ versus F is described by

$$\dot{\phi}_p = \rho_p(F - F_0) \tag{87}$$

where

$$\rho_p = \zeta_p \frac{A}{l} \tag{88}$$

and

$$F_0 = H_0 l \quad . \tag{89}$$

The nonlinear region of $\dot{\phi}_p$ versus F is described by

$$\dot{\phi}_p = \lambda(F - F''_0)^{\nu} \tag{90}$$

where

$$\lambda = \kappa \frac{A}{l^{\nu}} \tag{91}$$

and

$$F''_0 = H''_0 l \quad . \tag{92}$$

For a given value of F, $\dot{\phi}_p(F)$ may be described alternatively by

$$\dot{\phi}_p = \rho'_p(F - F'_0) \tag{93}$$

where

$$\rho'_p = \lambda\nu(F - F''_0)^{\nu-1} \tag{94}$$

and

$$F'_0 = F\left(1 - \frac{1}{\nu}\right) + \frac{F''_0}{\nu} \quad . \tag{95}$$

The relations between the leg parameters can now be derived. These relations may later be used to express D as a function of the leg dimensions. Let us refer the leg parameters to one of the legs, *e.g.*, to Leg 3. If the legs to be compared operate in their respective linear regions of $\dot{\phi}_p$ versus F, then, following Eqs. (88) and (89),

$$\rho_{\ast p} = \rho_{3p} \frac{A_{\ast} l_3}{A_3 l_{\ast}} = \rho_{3p}\ 2 \frac{l_3}{l_{\ast}} \quad , \tag{96}$$

$$\rho_{4p} = \rho_{3p} \frac{A_4}{A_3} \frac{l_3}{l_4} = \rho_{3p} \frac{l_3}{l_4} \quad , \tag{97}$$

$$F_{0m} = F_{03}\,\frac{l_m}{l_3}\quad, \tag{98}$$

and

$$F_{04} = F_{03}\,\frac{l_4}{l_3}\quad. \tag{99}$$

If the legs to be compared operate in the nonlinear regions of $\dot{\phi}_p$ versus F, then, following Eqs. (91) and (92),

$$\lambda_m = \lambda_3\,\frac{A_m}{A_3}\left(\frac{l_3}{l_m}\right)^{\nu} = \lambda_3\,2\left(\frac{l_3}{l_m}\right)^{\nu}\quad, \tag{100}$$

$$\lambda_4 = \lambda_3\,\frac{A_4}{A_3}\left(\frac{l_3}{l_4}\right)^{\nu} = \lambda_3\left(\frac{l_3}{l_4}\right)^{\nu}\quad, \tag{101}$$

$$F''_{0m} = F''_{03}\,\frac{l_m}{l_3}\quad, \tag{102}$$

and

$$F''_{04} = F''_{03}\,\frac{l_4}{l_3}\quad. \tag{103}$$

Before the relations between the leg parameters are substituted into the expressions for D, we need to derive the conditions that determine whether each leg operates in the linear or nonlinear region. This derivation is performed next.

c. VARIATIONS OF *H* IN EACH LEG

Suppose that the cross-sectional areas of Legs m, 3, and 4, as well as the lengths of Legs m and 3, are fixed, but the length of Leg 4 is varied. We shall first assume that $l_4 \geq l_3$, and examine two extreme cases: In Case *a*, $l_4 = l_3$; in Case *b*, $l_4 \to \infty$. We shall assume that Leg 4 is unloaded, since loading Leg 4 has essentially the same effect on flux division as increasing l_4 of an unloaded core,[8] and thus the case of loaded Leg 4 (of finite length) lies between Case *a* and Case *b*.

When $l_4 = l_3$ (Case *a*), Legs 3 and 4 in parallel appear as a single leg whose cross-sectional area is equal to A_m. In this case, the applied *NI* would divide uniformly along all legs, and $H_3 = H_4 = H_m$.

When $l_4 \to \infty$ (Case *b*), the core is essentially composed of Leg *m* and Leg 3 in series. Substitution of $\rho_p = \zeta_p A/l$, $F = Hl$, and $F_0 = H_0 l$ into Eqs. (55) and (56) yields expressions for $\dot{\phi}_m$ and $\dot{\phi}_3$. These expressions are equated, since $\dot{\phi}_m = \dot{\phi}_3$, yielding the following relation:

$$\frac{H_m - H_0}{H_3 - H_0} = \frac{A_3}{A_m} \frac{1 - \left(\frac{\phi_3}{\phi_s}\right)^2}{1 - \left(\frac{\phi_m}{2\phi_s}\right)^2} . \tag{104}$$

It is evident from Eq. (104) that the relationship between H_m and H_3 is affected by the cross-sectional areas of Legs *m* and 3, but not by the lengths of these legs. Substituting the relations $(A_3/A_m) = 1/2$, $\phi_m = -2\phi_r + \Delta\phi_m$, and $\phi_3 = -\phi_r + \Delta\phi_3 = -\phi_r + \Delta\phi_m$ into Eq. (104), we get:

$$\frac{H_m - H_0}{H_3 - H_0} = \frac{1}{2} \frac{1 - \left(\frac{\Delta\phi_m}{\phi_s} - \frac{\phi_r}{\phi_s}\right)^2}{1 - \left(\frac{\Delta\phi_m}{2\phi_s} - \frac{\phi_r}{\phi_s}\right)^2} . \tag{105}$$

As switching progresses in time, $\Delta\phi_m$ varies from zero to $2\phi_r$. The curve $(H_m - H_0)/(H_3 - H_0)$ versus $(\Delta\phi_m/2\phi_s)$ [Eq. (105)] is plotted in Fig. 16, assuming that $(\phi_r/\phi_s) = 0.9$ [hence $(\Delta\phi_m/2\phi_s) = 0.9$ corresponds to $\Delta\phi_m = 2\phi_r$]. Note that the curve is below unity during the whole switching time, and that it reaches a peak of ~0.735 when $\Delta\phi_m \cong 0.4\phi_s = 0.444\phi_r$, *i.e.*, when Leg *m* completes about 22.2% of its total switching.

It was shown previously that in Case *a* (where $l_4 = l_3$), $H_m = H_3$, and hence $(H_m - H_0)/(H_3 - H_0) = 1$. The plots of $(H_m - H_0)/(H_3 - H_0)$ versus $(\Delta\phi_m/2\phi_s)$ in the two extreme cases are compared in Fig. 16. Any intermediate case of $l_3 < l_4 < \infty$ would result in a plot that lies between these two plots. Thus, if $l_4 > l_3$, then $H_m < H_3$ throughout the switching time.

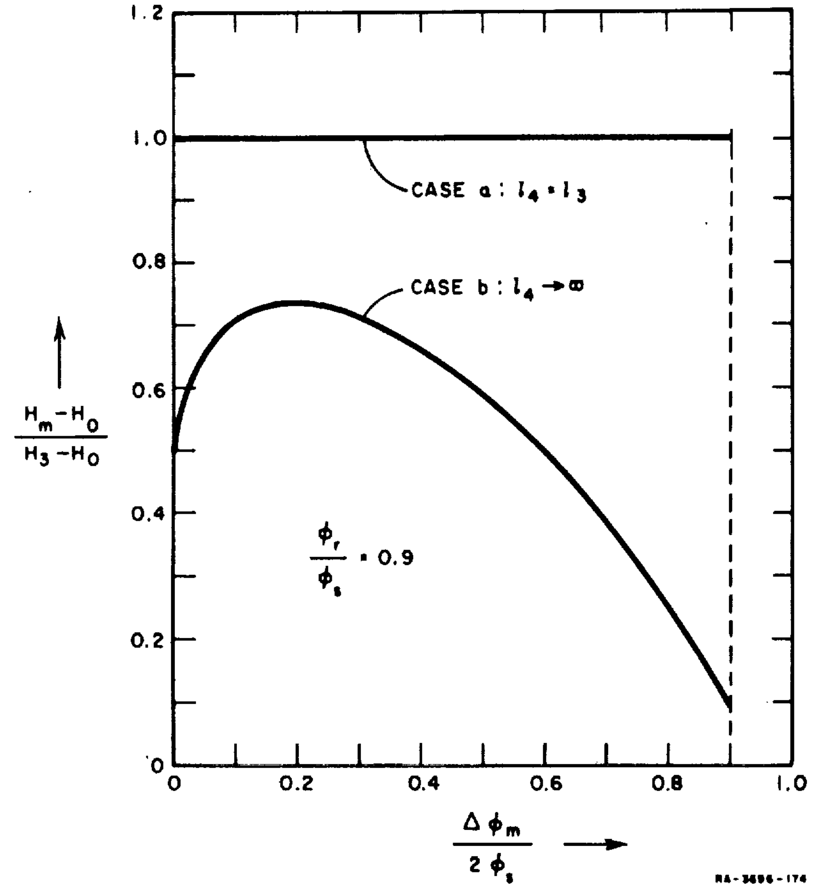

FIG. 16 $(H_m - H_0)/(H_3 - H_0)$ vs. $(\Delta\phi_m/2\phi_s)$

From the way $(H_m - H_0)/(H_3 - H_0)$ versus $(\Delta\phi_m/2\phi_s)$ varies in Fig. 16 as l_4 is decreased from ∞ to l_3, it may be deduced that if l_4 is decreased below l_3, the ratio $(H_m - H_0)/(H_3 - H_0)$ would rise above unity. Suppose now that Leg 3 and Leg 4 interchange functions, and we plot $(H_m - H_0)/(H_4 - H_0)$ versus $\Delta\phi_m/2\phi_s$. Then, the curve above unity will correspond to $l_3 < l_4$. Applying this observation to our previous case in which $l_3 < l_4$, we infer that $H_m > H_4$. In conclusion, for any value of NI large enough to switch flux inelastically in a three-leg saturable core $(A_3 = A_4 = A_m/2)$, if $l_4 > l_3$, then $H_3 > H_m > H_4$ during the whole switching time. Since $H_3 > H_m > H_4$ at any instant of switching time, we deduce that $\overline{H}_3 > \overline{H}_m > \overline{H}_4$, where $\overline{H}$ indicates a time-averaged value of H over the switching time T.

These inequalities are of interest, but additional information about the magnitude of H in each leg relative to H_B (Fig. 15) is needed in order to determine the region of operation. Since calculation of instantaneous H in each leg and its effect on D is quite involved, we shall simplify the problem by replacing H by $\overline{H}$. Calculation of $\overline{H}_3$, $\overline{H}_{\blacksquare}$, and $\overline{H}_4$ (assuming that Leg 4 is unloaded) will be done next.

With no load on Leg 4,

$$\overline{F}_3 = \overline{F}_4 = \frac{\int_0^T F_3 dt}{T} \quad . \tag{106}$$

Substitution of the expressions for $\int_0^T F_3 dt$ [Eq. (D-12)] and T [Eq. (D-14)] into Eq. (106) gives

$$\overline{F}_3 = \overline{F}_4 = \frac{(NI - F_{0\blacksquare})\rho_{\blacksquare p} + F_{04}\rho_{4p} + F_{03}\rho_{3p}}{\rho_{\blacksquare p} + \rho_{3p} + \rho_{4p}} \quad . \tag{107}$$

Since $F_{\blacksquare} = NI - F_3$, then $\overline{F}_{\blacksquare} = NI - \overline{F}_3$; hence, $\overline{F}_{\blacksquare}$ can be obtained by subtracting $\overline{F}_3$ [Eq. (107)] from NI. Following the relation $\overline{H} = \overline{F}/l$, we calculate $\overline{H}_3 = \overline{F}_3/l_3$, $\overline{H}_4 = \overline{F}_4/l_4$, and $\overline{H}_{\blacksquare} = \overline{F}_{\blacksquare}/l_{\blacksquare}$. Each of these $\overline{H}$ values may be compared with H_B, Fig. 15, in order to determine whether operation occurs in the linear portion of $\dot{B}_p$ versus H (or $\dot{\phi}_p$ versus F). It should be emphasized that the conclusion drawn by this step is only an approximation, because the instantaneous value of H was replaced by its time-averaged value, $\overline{H}$.

It was shown previously that if $l_3 < l_4$, then $\overline{H}_3 > \overline{H}_{\blacksquare} > \overline{H}_4$. Therefore, if $\overline{H}_4 > H_B$, then all three legs operate in their respective linear portions. This condition is satisfied when $NI \geq NI_{B4}$, where NI_{B4} is the value of NI for which $(\overline{F}_4/l_4) = H_B$. Under this condition, the relations between the leg parameters follow Eqs. (96) through (99), and by equating $\overline{F}_4$ [Eq. (107)] to $H_B l_4$, we find that

$$NI_{B4} = H_B l_4 \left[1 + \frac{1}{2}\left(\frac{l_{\blacksquare}}{l_3} + \frac{l_{\blacksquare}}{l_4}\right)\right] \quad . \tag{108}$$

As NI is reduced below NI_{B4}, $\bar{H}_4 < H_B$, $\bar{H}_3 > H_B$, and $\bar{H}_*$ remains above H_B until NI reaches NI_{B*}, when $\bar{H}_*$ becomes equal to H_B. A further reduction in NI to NI_{B3} lowers $\bar{H}_3$ to H_B, and if $NI < NI_{B3}$, then $\bar{H} < H_B$ in every leg. Calculation of NI_{B*} and NI_{B3} is more complex than calculation of NI_{B4}, because of the dependence of some or all the leg parameters on the F values [Eqs. (94) and (95)].

To summarize, there are four regions of NI:

(1) $NI \geq NI_{B4}$, where $\bar{H}_3 > \bar{H}_* > \bar{H}_4 \geq H_B$.

(2) $NI_{B4} \geq NI \geq NI_{B*}$, where $\bar{H}_3 > \bar{H}_* \geq H_B \geq \bar{H}_4$.

(3) $NI_{B*} \geq NI \geq NI_{B3}$, where $\bar{H}_3 \geq H_B \geq \bar{H}_* > \bar{H}_4$.

(4) $NI_{B3} \geq NI$, where $H_B \geq \bar{H}_3 > \bar{H}_* > \bar{H}_4$.

In calculating D versus NI, the parameters of each leg will be assumed ρ_p and F_0 [Eqs. (88) and (89)] if $\bar{H} \geq H_B$, but if $\bar{H} < H_B$, then the parameters to be assumed are ρ_p' and F_0' [Eqs. (94) and (95)]. Computation of this type is extremely tedious when done manually, but is quite simple when performed on a computer. We notice, however, that in the region where $NI \geq NI_{B4}$, all leg parameters are constant; hence, calculation of D in this region should be simpler, as we shall see next.

d. D VERSUS (l_4/l_3) FOR $NI > NI_{B4}$

If $NI > NI_{B4}$ [Eq. (108)], then the leg parameters ρ_p and F_0 [Eqs. (88) and (89)] are independent of NI. These leg parameters differ from each other only because of variation in dimensions, as expressed in Eqs. (96) through (99). Our objective now is to substitute Eqs. (96) through (99) into the previous derivations in order to express D versus leg-length ratios in a more direct fashion.

The general solution, Eqs. (70) through (73), remains unchanged, except that the expressions for p and q are reduced to the following.

$$p = \frac{2\dfrac{N_L^2}{R_L}\rho_{4p}\left[1 - \dfrac{F_{03}}{NI}\left(1 + \dfrac{l_*}{l_3}\right)\right]\left(\dfrac{\phi_r}{\phi_s} - \dfrac{\phi_{3f}}{\phi_s}\right)}{1 + \dfrac{l_3}{l_4} - \dfrac{F_{03}}{NI}\left(2 + \dfrac{l_*}{l_3} + \dfrac{l_*}{l_4}\right)} \tag{109}$$

and

$$q = \frac{1 - \dfrac{l_3}{l_4}}{1 + \dfrac{l_3}{l_4} - \dfrac{F_{03}}{NI}\left(2 + \dfrac{l_a}{l_3} + \dfrac{l_a}{l_4}\right)} \qquad (110)$$

We shall now examine several special cases.

When the core is unloaded, Eq. (110) is substituted into Eq. (74) directly in order to calculate D_{NL}.

For $NI \to \infty$, substitution of the relation $(\rho_{4p}/\rho_{3p}) = (l_3/l_4)$ [Eq. (97)] into Eqs. (76) and (77) gives

$$p_{NI\to\infty} = \frac{2\dfrac{N_L^2}{R_L}\rho_{4p}}{1 + \dfrac{l_3}{l_4}}\left(\frac{\phi_r}{\phi_s} - \frac{\phi_{3f}}{\phi_s}\right) \qquad (111)$$

and

$$q_{NI\to\infty} = \frac{1 - \dfrac{l_3}{l_4}}{1 + \dfrac{l_3}{l_4}} \quad . \qquad (112)$$

Substituting Eq. (72) into Eq. (111) results in a transcendental equation in $p_{NI\to\infty}$. A numerical solution for $p_{NI\to\infty}$ can be obtained without any difficulty. The values of $p_{NI\to\infty}$ and $q_{NI\to\infty}$ [Eqs. (111) and (112)] are substituted into Eq. (73) in order to compute $D_{NI\to\infty}$. For the no-load case, Eq. (78) becomes

$$D_{NL,NI\to\infty} = \frac{1 - \delta^{\left[\frac{2}{1+(l_3/l_4)}\right]}}{\delta^{\left[\frac{1-(l_3/l_4)}{1+(l_3/l_4)}\right]} - \delta} \qquad (113)$$

For the case of $\delta \to 1$, substitution of Eqs. (96) through (99) into Eqs. (79), (80), (81), and (81a) results in the following expressions:

$$D_{\delta \to 1} = \frac{2\left[NI - F_{03}\left(1 + \frac{l_m}{l_3}\right)\right]\left(1 + \rho_{3p}\frac{l_3}{l_4}\frac{N_L^2}{R_L}\right) + F_{03}\left(\frac{l_m}{l_3} - \frac{l_m}{l_4}\right)}{2NI\frac{l_3}{l_4} - F_{03}\left(2 + \frac{l_m}{l_3} + \frac{l_m}{l_4}\right)} , \qquad (114)$$

$$D_{NL,\delta \to 1} = \frac{2 - \frac{F_{03}}{NI}\left(2 + \frac{l_m}{l_3} + \frac{l_m}{l_4}\right)}{2\frac{l_3}{l_4} - \frac{F_{03}}{NI}\left(2 + \frac{l_m}{l_3} + \frac{l_m}{l_4}\right)} , \qquad (115)$$

$$D_{\delta \to 1, NI \to \infty} = \frac{l_4}{l_3} + \rho_{3p}\frac{N_L^2}{R_L} , \qquad (116)$$

and

$$D_{NL, \delta \to 1, NI \to \infty} = \frac{l_4}{l_3} . \qquad (117)$$

Note that only Eq. (117) yields the value of D that was expected when the problem of flux division was first introduced.^{6} But one should recall that Eq. (117) was derived assuming no variation of ρ with flux in every leg, a condition valid only for small variations of ϕ around $\phi = 0$ in each leg, as was shown in Fig. 13.

6. SUMMARY

An analysis of flux division ratio D in a loaded saturable core has been developed, assuming that $w_3 = w_4 = w_m/2$ and that $\Delta\phi_m = 2\phi_r$. The calculation of $\Delta\phi$ in a leg was based on a parabolic model for ρ. The final expression for D [Eq. (73)] is a function of three terms: δ, which depends on the ratio of ϕ_r to ϕ_s; q, which is a function of the inelastic-switching parameters of each leg and SET MMF NI; and p, which is a function of the leg parameters, NI, N_L^2/R_L, and ϕ_r/ϕ_s. Computation of a general case involves a transcendental solution for p [Eqs. (70) through (72)]; if, in addition, NI is low, the six leg parameters are determined by an iteration process that involves calculation of $\overline{F}$ in each leg and the nonlinearity of $\dot{B}_p$ versus H. In the no-load case, the computation is simpler, because $p = 0$; hence, no transcendental solution for p is needed. The expression for D in the no-load case is given in Eq. (74), and if, in addition, $NI \to \infty$, this expression is reduced further, Eq. (78). It was shown in connection with variation of leg parameters with NI that, since $A_m > A_3 = A_4$ and $l_3 < l_4$, then $H_3 > H_m > H_4$ during the whole switching time. The effect of l_4/l_3 on D is manifested indirectly by affecting the relative magnitudes of the leg parameters. Only in the no-load case, when NI is large enough to switch Leg 4 in its linear region, can the effect of l_4/l_3 on D be expressed directly [Eqs. (74) and (110)]; *e.g.*, Eq. (113) for D_{NL} as $NI \to \infty$.

The validity of this analysis will be checked in Sec. II-D by comparing computed and measured D versus NI for various load values.

E. CONCLUSIONS

The objectives in this section may be classified into two categories: switching models (Parts A, B, and C) and the application of nonlinear switching models to the analysis of flux division (Part D).

In an attempt to improve our tools in dealing with switching properties of a constant-width leg, the static $\phi(F)$ curve was calculated from assumed two hyperbolic $B(H)$ functions, one for $H \leq H_{th}$ and the other for $H \geq H_{th}$. These hyperbolic functions are superior to the common linear approximation of $B(H)$ [*cf.* Report 1, Fig. 4(b), p. 4], and were chosen simply from experimental observation. It is well recognized that analytic derivation of such models, based on some fundamental rules in physics, would be more elegant. However, until such models are derived analytically, having these empirical hyperbolic models is better for certain engineering purposes than having no models at all.

Most of our switching models of a leg assume that the leg width, or rather cross-sectional area, is constant. Practical multipath cores, on the other hand, include variable-width legs. A typical example is the Transfluxor. Another example is the shaped MAD (see later, Fig. 42, p. 96) whose legs around the minor apertures, especially the inner ones, are variable in width. Calculation of switching parameters for a variable-width leg of an arbitrary shape is very complex. For this reason we have simplified the problem by calculating ρ (a very important switching parameter in common application) of a tapered leg as a function of geometry and flux level. Approximating half of the main leg in a Transfluxor, or Leg 3 in a MAD, by a tapered leg is more accurate than by a constant-width leg. Calculation of ρ of a tapered leg has, therefore, practical applications.

Average ρ which is constant in time is useful when $\Delta\phi$ is calculated. In Report 1 (pp. 28-30), $\bar{\rho}$ and ρ_{av} of a constant-width leg were calculated only for full switching, *i.e.*, for $\Delta\phi = 2\phi_r$. In analyzing analog circuits, where ϕ changes from $-\phi_r$ to an arbitrary level ϕ_f, there is a need for the average ρ as a function of ϕ_f. We have shown that $\rho_{av} = (1/\Delta\phi)\int_0^{\Delta\phi} \rho d\phi$ and $\bar{\rho} = \Delta\phi/[\int_0^{\Delta\phi}(1/\rho)d\phi]$ and that $\bar{\rho}$, not ρ_{av}, is the useful parameter for calculating $\Delta\phi$. For this reason we have calculated families of $\bar{\rho}$ versus ϕ_f/ϕ_s, with ϕ_r/ϕ_s as a parameter for both a constant-width leg and a tapered leg. The point where $\bar{\rho}/\rho_p$ reaches maximum is the point where we can get the maximum $\Delta\phi$ per unit of DRIVE excess charge-turns.

No attempt has been made to use the expression for $\bar{\rho}$ in order to calculate flux division in a saturable core. However, inspection of the plot of $\bar{\rho}/\rho_p$ versus ϕ_f/ϕ_s (*cf*. Fig. 7) reveals the essential mechanism associated with flux division. Since $l_3 < l_4$, then $F_{03} < F_{04}$ and $\rho_{3p} > \rho_{4p}$; hence, $\Delta\phi_3 > \Delta\phi_4$. This, in turn, calls for $\bar{\rho}_3/\rho_{3p}$ to be larger than $\bar{\rho}_4/\rho_{4p}$, which serves as another reason for $\Delta\phi_3$ to exceed $\Delta\phi_4$. It is this factor that complicates the dependence of D on l_4/l_3 and yields higher values of D than expected by simple considerations that ignore the parabolic relation between ρ and ϕ.

We shall see in Sec. II-D how calculated D versus NI compare with measured data. This analysis will be extended in the future to a non-saturable core, such as a Laddic, once we have better switching models for a leg that is initially in a partially switched state.

II EXPERIMENTATION AND DISCUSSION

The purpose of this section of the report is to verify experimentally and discuss some of the theory and calculation of Report 1 and Sec. I of this report. In Part A, some measurements of toroidal core switching properties are presented and discussed. Part B treats the design and geometrical considerations of two multipath cores that are to be used for experimentation on flux switching in multipath cores. The two final core designs, one saturable and the other nonsaturable, are also given in this section. In Part C, test procedures for obtaining the switching parameters of a leg are described in general, and an example is given using one of the designed cores. Experiments on flux division are described in Part D, using the two designed cores. The results for the nonsaturable core are compared with the published data on flux division in a Laddic (*cf*, Report 1 pp. 75-80). The results for the saturable core are compared with the analysis of flux division developed in Sec. I-D of this report. Finally, in Part E, the phenomenon of unsetting effect (*cf*. Report 1, pp. 96-99) is verified experimentally.

A. PROPERTIES OF TOROIDAL CORES

Most of the magnetic material properties can best be determined by choosing a simple geometry so as not to introduce superfluous complications. Thus, toroidal cores are used when material properties are to be studied.

1. EFFECT OF SWITCHING RATE ON STATIC $\phi(F)$ CURVES

One of the fundamental properties that is needed is the static $\phi(F)$ curve. The technique for obtaining this characteristic consists of using a positive dc MMF to set the core, and a negative rectangular pulse, superimposed upon the dc MMF, to clear the core, as shown in Fig. 17(a) with Switch Sw open. The dc MMF acts during a time T between CLEAR pulses. Thus, for a low repetition rate (*e.g.*, 60 cps), $\phi(F)$ is essentially the static $\phi(F)$ curve. The flux change is measured during the CLEAR pulse, since the high CLEAR MMF produces a $\dot{\phi}(t)$ of short duration and high amplitude, which is easy to integrate in order to determine $\Delta\phi$. The setting begins at the time when the magnitude of the CLEAR pulse falls below the

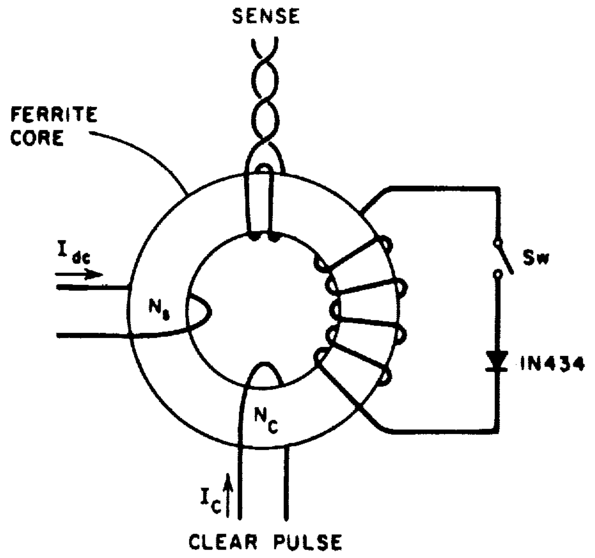

(a) CIRCUIT

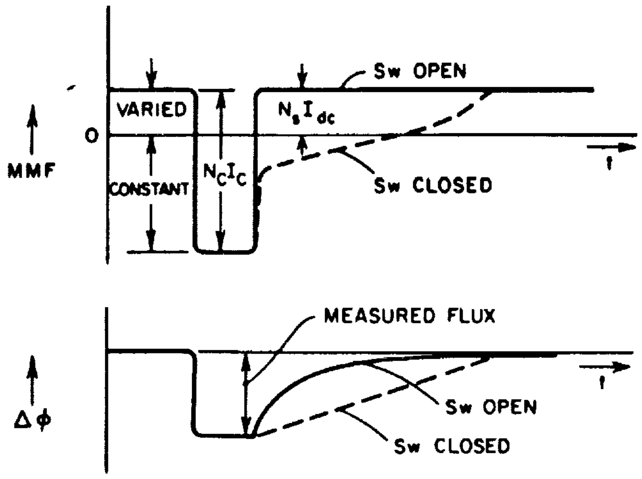

(b) NET MMF APPLIED AND FLUX WAVEFORM

RA-3696-147

FIG. 17 MEASUREMENT OF STATIC ϕ(F) CURVE dc MMF. The fall time of the CLEAR pulse is typically of the order of 0.1 μsec to 1 μsec, so that the dc SET MMF effectively comes on relatively fast. It was questioned whether this short rise time of the SET MMF significantly affects the resulting static $\phi(F)$ curve. There was no particular reason to expect a difference, but there was also no assurance that no difference existed. The following experiment was performed to see if there was any difference in the static $\phi(F)$ curve obtained with a short rise time compared with a very long rise time.

The static $\phi(F)$ curve of a MAD, treated as a toroid, was determined for two different conditions. The first condition was the usual one described above. In the second condition, Switch Sw was closed, so that the 100-turn winding, which is in series with a diode, would constitute a short-circuited winding during the SET time, and an open-circuited winding during the CLEAR time. Alternatively, one could have increased the fall time of the CLEAR pulse, but this would have required a modification of the pulser. The current induced in this 100-turn winding slowed down the switching rate during the SET time by an appreciable amount. A comparison between the MMF's and $\Delta\phi$'s *versus* time in the two cases is shown in Fig. 17(b). An additional comparison of the two cases is made in the ϕ-F plane in Fig. 18. The resulting two static $\phi(F)$ curves are shown in Fig. 19. These curves are in agreement with each other for values of F below the midpoint of the upper knee. Above this point, the curve for Sw closed is about 2.7% lower. It is not known presently whether this small difference is due to the difference in the switching rates, or due to an unaccounted-for experimental error. The extra wiggle in the steep part of Fig. 19 is a result of the existence of minor apertures in the MAD. It is concluded that the $\phi(F)$ curves taken with Sw open (without the diode) can be considered as being essentially static.

2. TESTING BLANK DISKS

Special multipath cores, which were to be used in a study of flux division (to be described in Part D), were ultrasonically cut from ½-inch diameter Telemeter Magnetics T-5 ferrite disks. To ensure that no excessive radial variations in material properties existed in these disks, they were individually tested as toroids of very high OD/ID ratio before the cutting process. This was done by recording a 10 μsec $\phi(F)$ curve of each disk (each disk had a 0.050-inch-diameter hole in the center through which the SET and CLEAR windings could be wound). Disks having a sharp

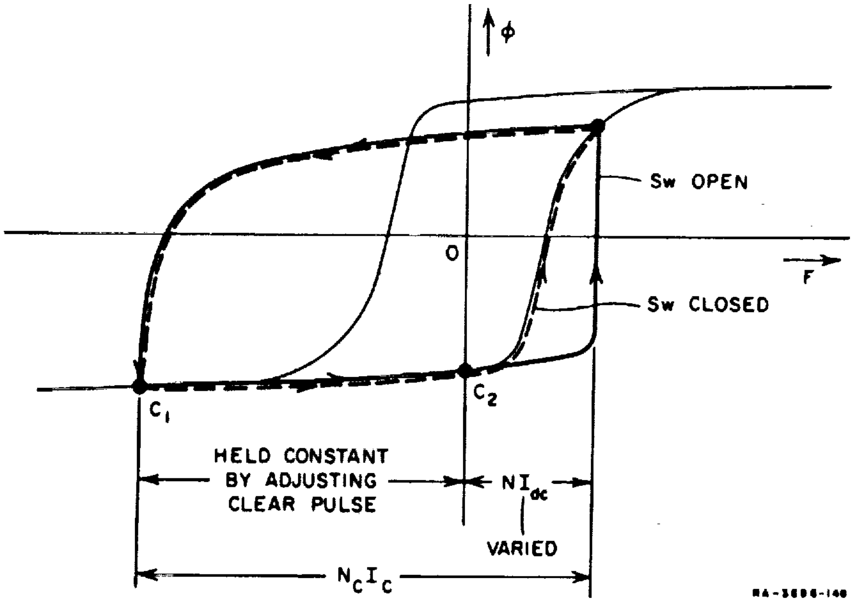

FIG. 18 PATHS OF OPERATION FOR TWO CASES OF STATIC ϕ(F) CURVE MEASUREMENT

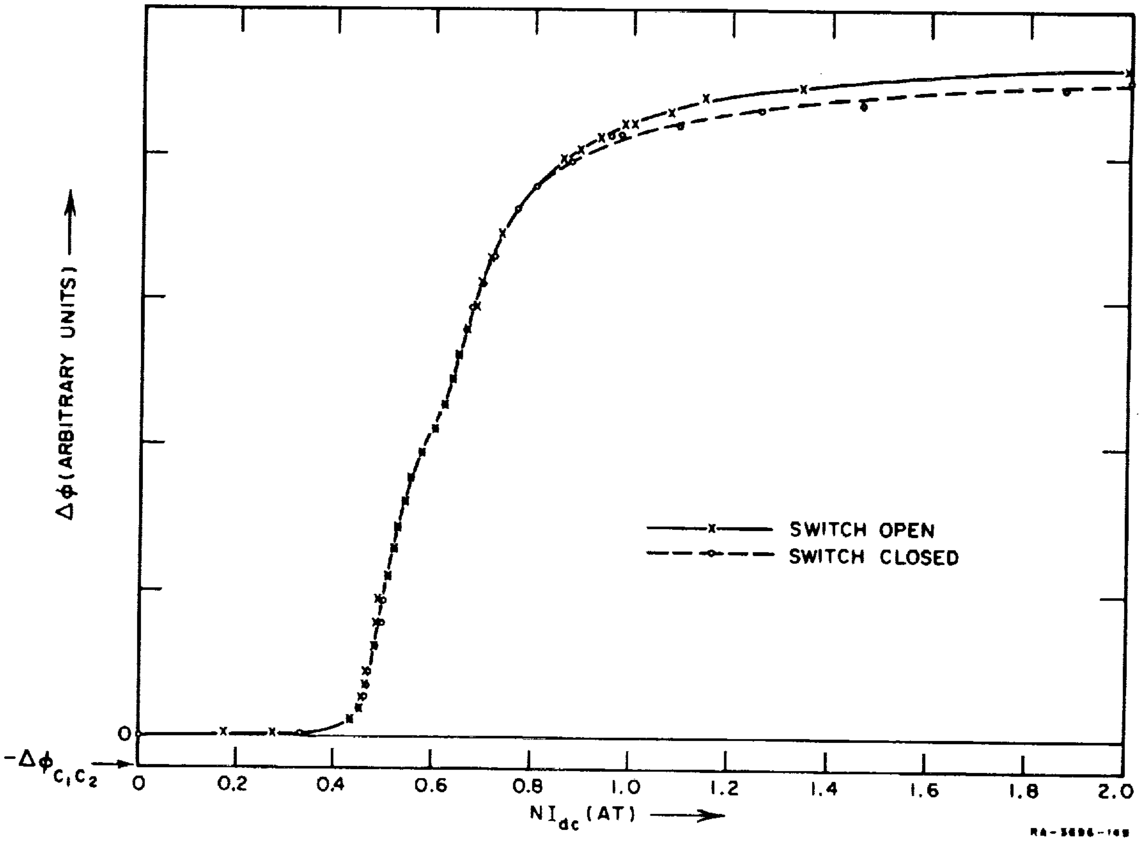

FIG. 19 STATIC ϕ(F) CURVES WITH Sw OPEN AND CLOSED
AMP Incorporated, Core No. 395813-1, Geometry is given in Fig. 42

radial variation in coercivity, resulting in a $\phi(F)$ curve with a kink in the steep part of the curve, were rejected.

3. MODIFICATION OF THE PARABOLIC MODEL

The parabolic switching model,

$$\dot{\phi} = \rho(F - F_0) \quad , \tag{118}$$

where

$$\rho = \rho_p\left[1 - \left(\frac{\phi}{\phi_s}\right)^2\right] , \tag{119}$$

agrees with experimental data at high F values, but is poor at low values of F [*i.e.*, F slightly greater than the lower knee of the static $\phi(F)$ curve]. This is evidenced both by the static $\phi(F)$ loop, which does not have vertical sides as is assumed in the model, and by the $\dot{\phi}_p(F)$ curve, which is not linear at low F values, as is assumed by the model. It would be valuable to know for what reasons the model does not agree at low F values, at least phenomonologically, and what approach one might use in modifying the model to obtain better agreement. For these reasons, experimental $\dot{\phi}(\phi)$ curves of a thin ring were examined for each of several constant F values. Oscillograms of these experimental $\dot{\phi}(\phi)$ curves can be obtained by the technique described in Appendix G. The thin ring had an OD/ID ratio of 1.06 and was made of a low-threshold ferrite (Telemeter Magnetics T-5). The $\dot{\phi}(\phi)$ curve obtained from Eqs. (118) and (119) for constant F is parabolic and is, therefore, symmetrical in ϕ. The experimental $\dot{\phi}(\phi)$ curves were symmetrical (except for the initial spike) at high F values, but very asymmetrical at low F values, with the peak to the left of the center of $\Delta\phi$. One possible way of accounting for this asymmetry is to consider F_0 [Eq. (118)] to be some appropriate function of ϕ. F_0 must increase as ϕ varies from $-\phi_r$ to ϕ_s in order to shift the peak of the $\dot{\phi}(\phi)$ curve to the left. Such an $F_0(\phi)$ variation also results in a static $\phi(F)$ loop whose sides are not vertical, but have finite positive slopes. This is observed experimentally even for very thin rings. It is possible that the effects of radial variations of H resulting from an OD/ID ratio significantly greater than unity can also be accounted for by an appropriate $F_0(\phi)$ function. Since the final value of ϕ attained for each constant value of F is described by the static $\phi(F)$ curve, it is likely that the inverse of the static $\phi(F)$ curve is a reasonable approximation for $F_0(\phi)$, especially toward the end of the switching.

An attempt was made to account for the $F_0(\phi)$ variation by assuming that F_0 is equal to d of the static $\phi(F)$ curve (*cf.* Report 1, Fig. 9, p. 8). It is also assumed that the initial value of ϕ, ϕ_0, was equal to $-\phi_r$. The resulting calculated $\dot{\phi}(\phi)$ curves, which contained a constant ρ_p, yielded a nonlinear $\dot{\phi}_p(F)$ function that was still different from the experimental $\dot{\phi}_p(F)$ curve. Therefore, to obtain a reasonable comparison of computed and experimental $\dot{\phi}(\phi)$ curves, ρ_p was assumed to be nonconstant with F and its value calculated for each value of F by equating the computed and experimental $\dot{\phi}_p$. The resulting calculated and experimental $\dot{\phi}(\phi)$ curves are shown in Fig. 20 for three values of F. The values of ρ_p are also given in Fig. 20. The $\dot{\phi}(\phi)$ curves are plotted normalized to ϕ_s, whose value is obtained from the experimental static $\phi(F)$ curve [Fig. 21(a)] at $5F_0$, or $F = 7.5$ ampere-turns. Also shown in Fig. 21(a) are the values of F corresponding to the $\dot{\phi}(\phi)$ curves of Fig. 20. This static $\phi(F)$ curve is the one that was used for the $F_0(\phi)$ variation in computing the $\dot{\phi}(\phi)$ curves of Fig. 20. Note that if F_0 had been assumed constant [*i.e.*, the static $\phi(F)$ loop had vertical sides], then the $\dot{\phi}(\phi)$ curves of Fig. 20 would all terminate at $\phi/\phi_s = 1$. The experimental $\dot{\phi}_p(F)$ curve for this core is shown in Fig. 21(b). Note that the values of F in Fig. 20 are in the very nonlinear region of this $\dot{\phi}_p(F)$ curve. The initial spike observed in the calculated $\dot{\phi}(\phi)$ curves of Fig. 20 is a result of the low values of F_0 obtained from the static $\phi(F)$ curve near $\phi = -\phi_r$ [see Fig. 21(a)].

It is concluded that the parabolic model can be significantly improved for low F values by considering variation of ρ_p with F and variations of F_0 with ϕ, but that some disagreement still persists. The next step in the modification is the determination of analytical functions for $\rho_p(F)$ and $F_0(\phi)$. The major disadvantage of the modification of the parabolic model is, of course, the added complexity, which in some cases may not be justified. It may be helpful for some cases to introduce $\rho_p(F)$, but not $F_0(\phi)$. In this case, $\rho_p(F)$ can be determined from the $\dot{\phi}_p(F)$ curve, as was done in Sec. I-C.

4. SUMMARY

The effect of switching rate during the setting time of the static $\phi(F)$ experiment was found to be very small (*cf.* Fig. 19). Blank disks, from which multipath cores were cut (for use in the flux-division experiments), were selected on the basis of their $\phi(F)$ property. Experimental

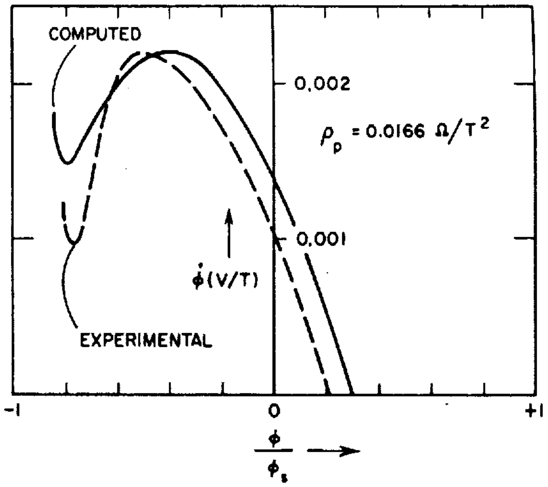

(a) F = 1.00 AT

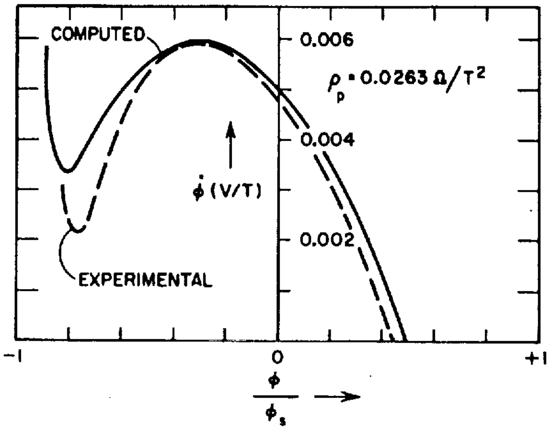

(b) F = 1.106 AT

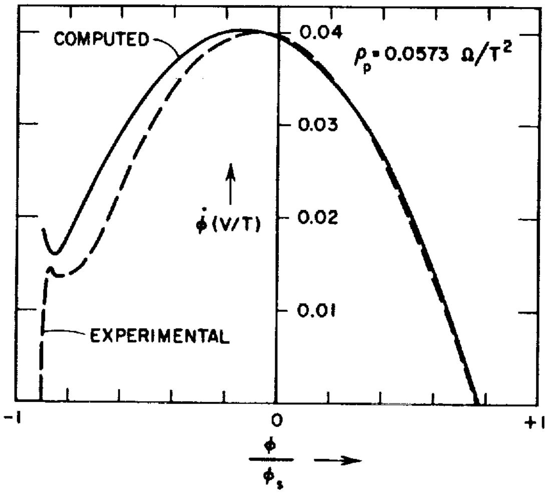

(c) F = 1.60 AT

RD-3696-175

FIG. 20 COMPARISON OF EXPERIMENTAL AND COMPUTED $\dot{\phi}(\phi)$ CURVES FOR FERRITE THIN-RING E-6
r_i = 3.53mm; r_o = 3.75mm; r_{av} = 3.64mm; r_o/r_i = 1.06; h = 0.688mm

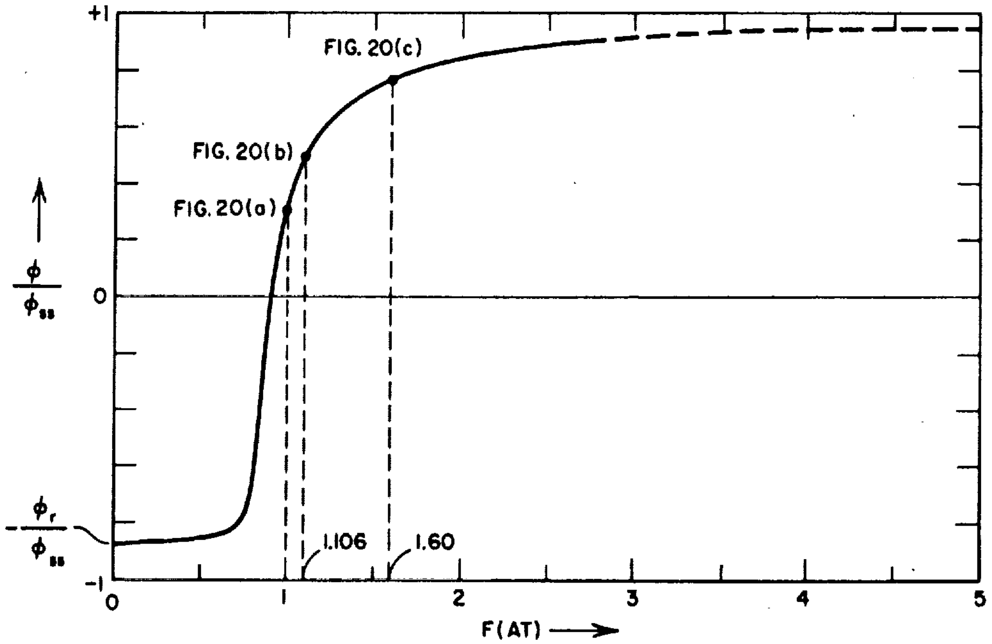

(a) STATIC $\phi(F)$ CURVE

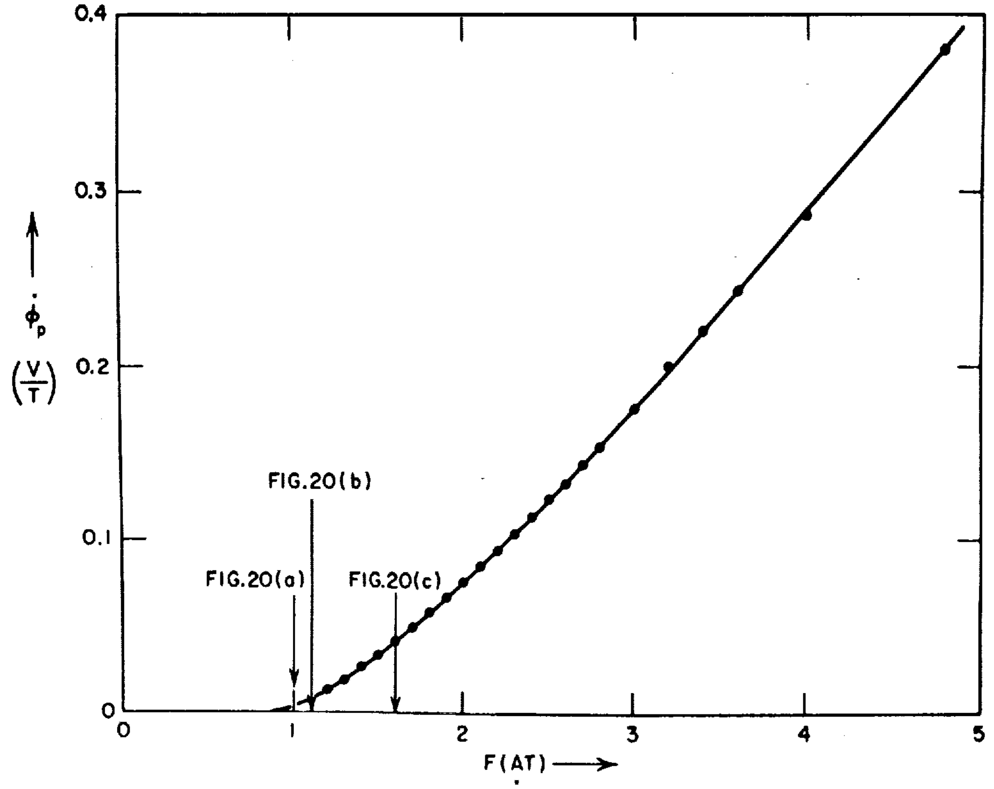

(b) $\dot{\phi}_p(F)$

RC-3696-150

FIG. 21 OPERATION IN FIG. 20 RELATIVE TO STATIC AND DYNAMIC CHARACTERISTICS

$\dot{\phi}(\phi)$ curves of thin ferrite ring are compared with curves calculated from the parabolic model (Fig. 20), with the following modifications: The F_0 of the parabolic model is assumed to be a function of ϕ. This $F_0(\phi)$ function is approximated by the inverse of the static $\phi(F)$ curve. The values of ρ_p in the parabolic model were assumed to be some function of F and are determined by equating calculated and measured peak $\dot{\phi}$ values.

B. GEOMETRY CONSIDERATIONS OF MULTIPATH CORES

As discussed in Report 1, p. 1, a multipath core can be divided into legs; each leg is characterized by appropriate switching models. Assuming uniform material, the switching properties of the legs differ from each other only due to variations in geometry. Unfortunately, the geometry of a leg is sometimes not well defined. We wish to discuss this problem in connection with the design of two multipath cores that were used for experimental verification of phenomena associated with core geometry in general, and flux division in particular. The design and analysis of these two cores involved a number of geometrical considerations that will now be discussed.

1. DESIGN CONSIDERATIONS

a. SATURABLE AND NONSATURABLE CORES

Two three-leg cores were designed for the flux-division experiment. The first core was intended for use in measuring flux division in a nonsaturable core. With this core, we checked and supplemented the experimental data on another core (Laddic) that was reported in the past.[6,7] We also hope to use these data for comparison with future analysis. The second core was saturable and served to verify experimentally the analysis of flux division developed in Sec. I-D. Both cores were ultrasonically cut from ferrite disks of constant thickness.

b. CROSS-SECTIONAL AREA OF A LEG

One of the most important geometrical properties of a leg to consider is the variation of its cross-sectional area or, if the thickness is constant, the variation of its width. There are many problems associated with the description of flux switching in a variable-width leg. These problems were discussed in Sec. I-B-2. Because of these problems, the experimental work on flux division was performed on multipath cores that were specially designed so that each leg had constant width for as much of its length as possible. Once flux division for such cores is well understood and predictable, there is a possibility of understanding flux division in less ideal cores.

c. JUNCTION PROBLEMS

Ideally, the legs of a multipath core should have dimensions that are uniquely defined, irrespective of the switching paths in the core. These switching paths are determined not only by the location of the drive windings, but also by the amplitudes of the drive currents. Each leg should have a well defined short edge of length l_i, (*cf.* Fig. 19, Report 1, p. 18), long edge of length l_o, and cross section of area A. In addition, the midpaths of all legs should meet at nodes, or junction points, from which the values of l^{av} may be obtained [actually for very thick legs, a path somewhat inside of the midpath should be chosen,[10] because of the difference between $1/(l^{av})$ and $(1/l)^{av}$]. These ideal conditions are assumed by the leg model, but cannot be realized physically. However, by designing cores that minimize the junction problems and by making suitable approximations in the determination of leg dimensions, the leg model can still be very useful. The alternative to using the leg model, *i.e.*, solving the non-linear field problem, is a very complex problem. In order to minimize junction problems, the junction volume should be made as small as possible, so that the percentage of a leg dimension that is ambiguous is minimized. This is done primarily by making the ratio of leg length to width, l/w, as high as possible. However, a high l/w ratio has the problem of flux leakage when a lumped drive winding is used. As a compromise, a value of $l/w \cong 18$ was chosen for the longest leg. Fillets should be avoided, since they also increase the junction volume. In designing a multipath core for which all legs have the same width, there are two advantages in having the three legs radiate from the junctions at approximately equal angles from each other: First, flux leakage is minimized; second, the location of the junction node is less dependent on where switching takes place.

d. LEG CONTOUR

The presence of sharp inside corners in a leg is not desirable because of leakage flux that bypasses the corner (Report 1, Fig. 106, p. 109). For this reason, unnecessary sharp corners were eliminated in the core designs.

e. FINAL CORE DESIGNS

The nonsaturable core, Core *N*, and the saturable core, Core *S*, were designed on the basis of the above discussion. The dimensions of these cores are shown in Fig. 22. Note that Core *N* has three legs of the same width, whereas Core *S* has two legs of the same width and a third leg of twice that width.

2. DETERMINATION OF l_i, l_o, AND l^{av}

In order to obtain the switching parameters of the legs in the cores under discussion, we must first determine the dimensions l_i, l_o, and l^{av} of each leg. However, the exact dimensions of each leg depend upon the paths of switching. To illustrate the problem, consider Core *N* and compare the case when the drive is on Leg 1 with the case when the drive is on Leg 2. The values of l_i and l_o of each leg are different in these two cases, as shown in Fig. 23. These particular choices of dimensions involve compromises and approximations, some of which will be discussed in the next part.

3. FLUX SWITCHING IN A CORE HAVING A RE-ENTRANT SHAPE

Discussion of the topic of this section requires the use of terminology that first must be defined.

A *switching line* in a magnetic core is a line at every point of which the vector $\dot{\mathbf{M}}$ is tangential. A *switching path* in a magnetic core is a group of switching lines.

The leg length l^{min} is determined by the line along which inelastic switching first occurs in a cleared leg ($\phi = -\phi_r$) as the MMF is slowly increased from zero. The leg length l^{max} is determined by the line along which inelastic switching last occurs as the MMF continues to increase slowly. Thus, l^{min} and l^{max} are determined by lines that may or may not follow the short and the long edges of the leg, as will be illustrated next.

Consider a core having a re-entrant shape, such as obtained by removing Leg 1 of Core *N* [*cf*. Figs. 22(a) and 24]. Assume that this core is initially well cleared in a clockwise sense, and that a dc current is applied to the winding on Leg 3 as shown in Fig. 24. The magnitude of this current is slowly increased until switching just begins in Leg 2. The initial switching line will be the shortest closed line linking the drive winding,

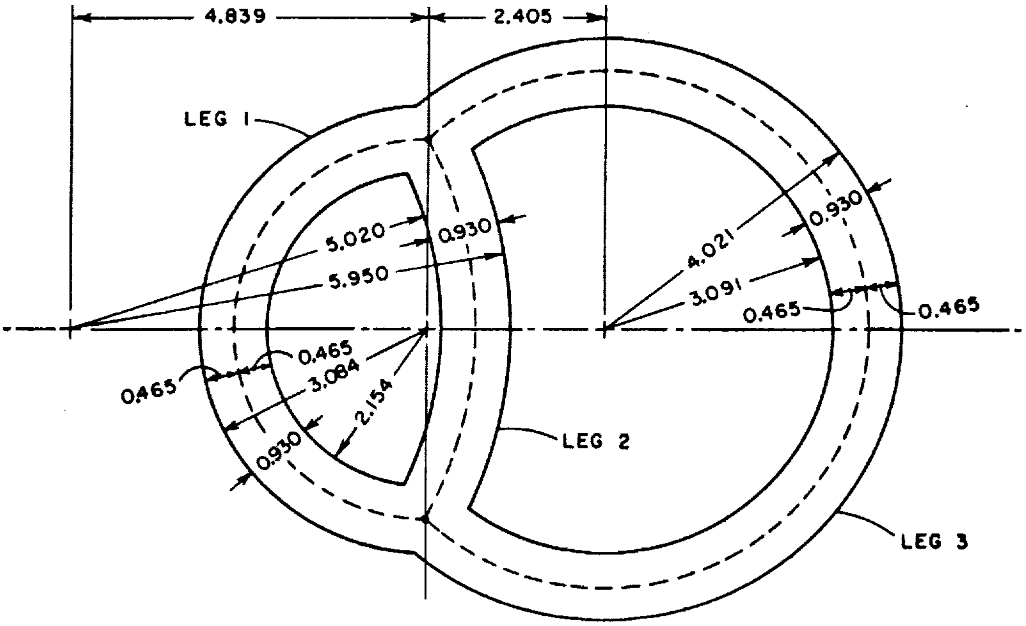

(a) CORE N (NONSATURABLE)
$[l_1^{av} = 7.75;\ l_2^{av} = 5.77;\ l_3^{av} = 16.835;]$

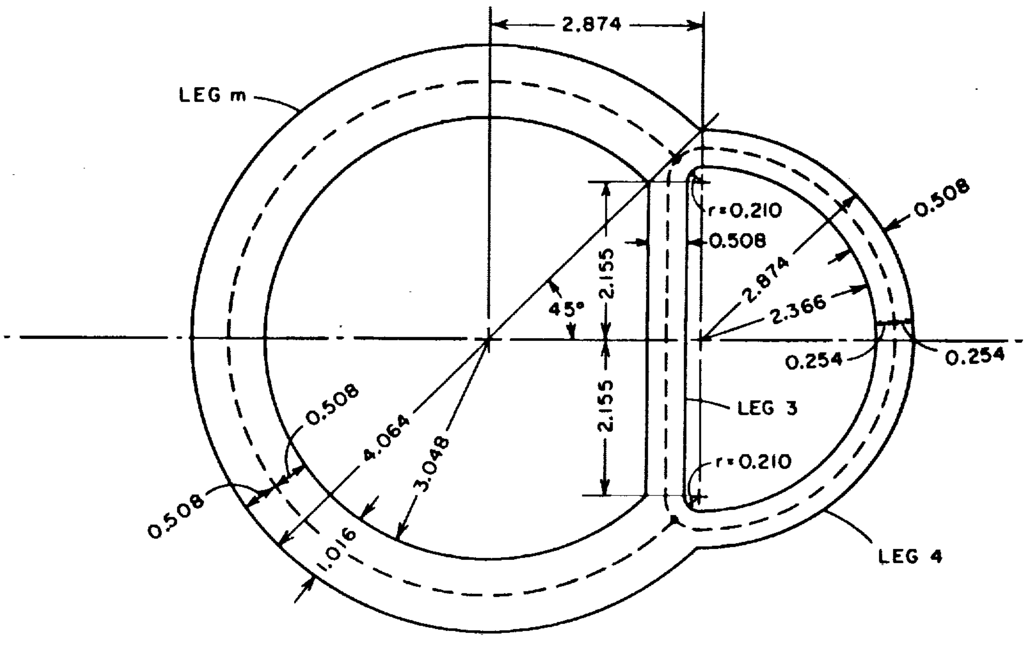

(b) CORE S (SATURABLE)
$[l_m^{av} = 16.845;\ l_3^{av} = 5.040;\ l_4^{av} = 8.960;]$

RB-3696-151

FIG. 22 DESIGNS OF CORES FOR EXPERIMENTATION
Dimensions in mm; h = 1.31mm; Tolerance = ±0.010mm

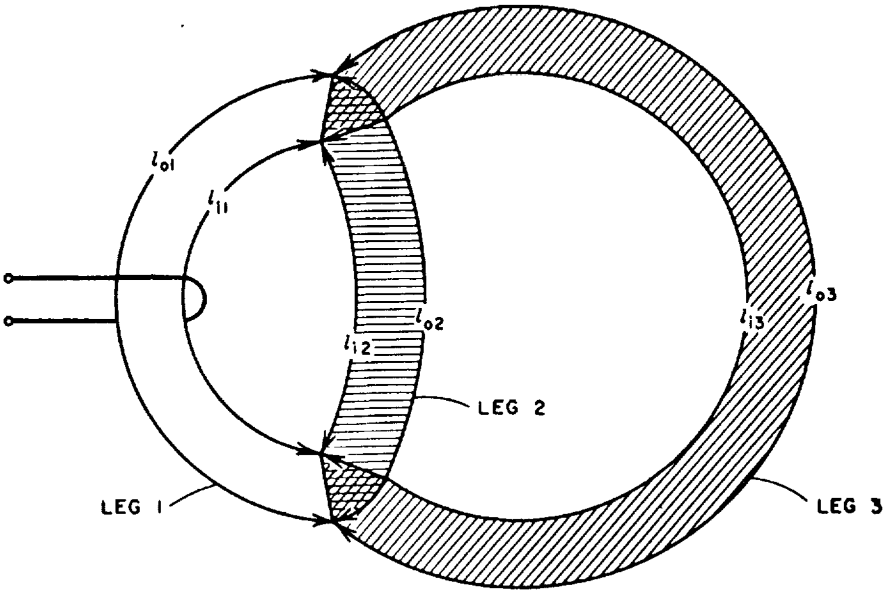

(a) DRIVE ON LEG 1

$$\begin{bmatrix} l_{i1} = 6.18 & l_{i2} = 4.38 & l_{i3} = 15.45 \\ l_{o1} = 9.32 & l_{o2} = 7.16 & l_{o3} = 18.22 \end{bmatrix}$$

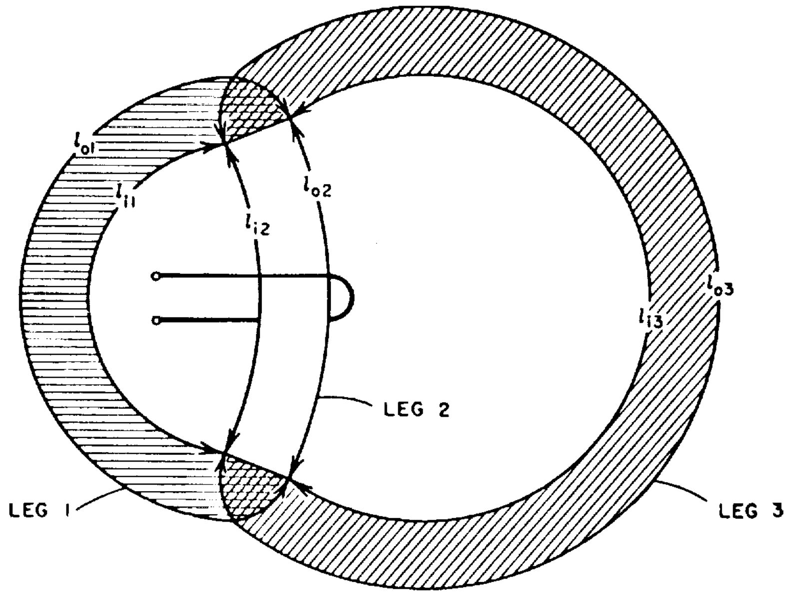

(b) DRIVE ON LEG 2

$$\begin{bmatrix} l_{i1} = 6.18 & l_{i2} = 4.38 & l_{i3} = 13.64 \\ l_{o1} = 11.31 & l_{o2} = 5.15 & l_{o3} = 20.19 \end{bmatrix}$$

RB-3696-152

FIG. 23 DETERMINATION OF l_i AND l_o (in mm) FOR EACH LEG OF CORE N *i.e.*, Line *A-B-C-D-A* in Fig. 24. Thus, $l_2^{\min}$ is equal to the length of Line *C-D-A*, whereas l_{i2} is the length of Line *C-F-A*. As the current is increased further, flux will be switched along lines that are longer than Line *A-B-C-D-A*, *e.g.*, Line *G-H-I-J-G*. The longest switching line continues to expand as the current is increased until it touches the left-hand surface of Leg 2, Point *T*. As the current is increased still further, the longest switching line must cross over the previous switching lines, as illustrated in Fig. 24 by Line *K-L-M-N-K*. The final switching line will resemble Line *O-P-Q-R-S-O*. The net result is that $l_2^{\min}$ is smaller than l_{i2} and $l_2^{\max}$ is larger than l_{o2}. Thus, the static $\phi(F)$ curve for this core would not be as steep as the static $\phi(F)$ curve that would be calculated by using l_i and l_o in Eqs. (16), (17), and (18).

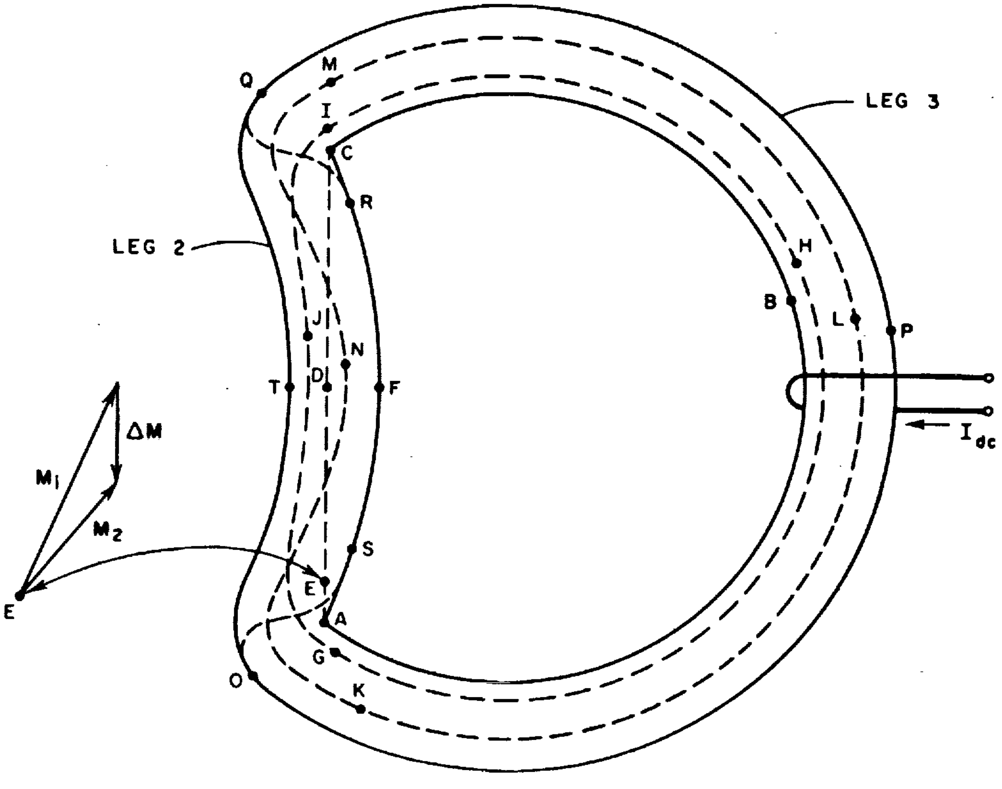

RA-3696-153

FIG. 24 SWITCHING LINES IN A CORE HAVING A RE-ENTRANT SHAPE

Consider Point *E* in Fig. 24. Since the core was initially well cleared, the magnetization $\mathbf{M}$ followed the contour of the core. Thus, the initial magnetization at Point *E* can be represented by the vector $\mathbf{M}_i$ in Fig. 24. When the MMF is increased just enough to establish switching in Line *A-B-C-D-E-A*, $\mathbf{M}$ changes from initial value $\mathbf{M}_i$ to an intermediate value $\mathbf{M}_2$. The vector difference $\Delta\mathbf{M}$ is parallel to $\dot{\mathbf{M}}$, which is tangential to the switching Line *A-B-C-D-E-A*. Whenever $\mathbf{M}$ at a point in a magnetic material changes direction by an angle other than 180°, some transverse switching is occurring and $\dot{\mathbf{M}}$ at that point is non-parallel to $\mathbf{M}$. In the absence of bulk anisotropy, this transverse switching must be accompanied by a transverse *H* field. The source of such an *H* field is, in general, made up of two components: the applied *H*, and the *H* due to div $\mathbf{M}$ (effective magnetic pole density), which develops on the surfaces and inside the magnetic material (see Report 1, p. 128; also Ref. 11), The properties of transverse switching need further investigation.

The above description is intended only to present the problems in understanding the switching in a core, such as the one of Fig. 24, and to estimate the location of the switching lines for slow switching. If, instead of the slow switching, fast switching is produced as a result of applying a relatively high-amplitude rectangular current pulse, then different switching lines would be obtained because switching would be occurring simultaneously, though at different rates, throughout the entire core. Several other examples in which the re-entrant shape is also encountered are the following:

(1) Driving on either Leg 2 [see Fig. 23(b)] or Leg 3 of Core *N* involves switching in the series combination of Legs 2 and 3, which has a re-entrant shape.

(2) In determining l_{i3} inside the junction of Fig. 23(a), the problem is mixed with the junction problem.

(3) The re-entrant shape also occurs in Legs 2 and 3 of the multi-aperture core shown in Fig. 97(a), (p. 102) of Report 1.

The detailed process of switching in a core as in Fig. 24 is difficult to determine, even for slow switching. However, if the shape of the core is made more re-entrant, as in the core shown in Fig. 25, and the material is assumed to have a static *B*(*H*) loop with vertical sides, then a simple model for slow switching can be proposed. This model has the zone pattern shown in Fig. 25, which provides magnetization closure and crossover switching paths (*i.e.*, switching paths which cross over from

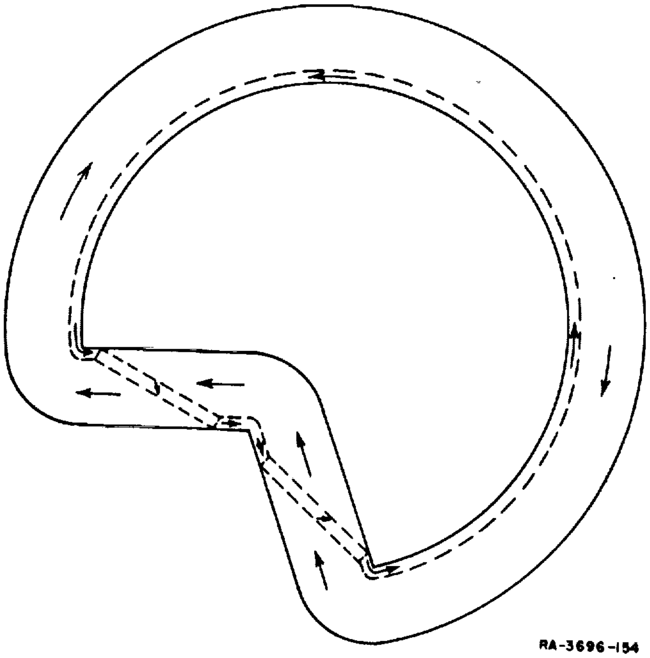

FIG. 25 SWITCHING PATH CROSSOVER ZONES IN A CORE HAVING A RE-ENTRANT SHAPE
Arrows Indicate Directions of M

one edge of the leg to the other edge). For a closer examination of these zones, refer to Figs. 26(a), (b) and (c). The dashed lines in these figures represent the zone boundaries. Note that the relative directions of the magnetization **M** and the zone boundaries are such that no magnetic poles exist at any of the zone boundaries (*cf.* Report 1, p. 122). The switching paths are identified by arrows in Fig. 26(c). Each switching path is bound by a dashed line and a dash-dot line. Note that the switching path could not pass diagonally through the rectangular zone without establishing new zone boundaries within the existing zone. Figure 26(c) also illustrates the motion of the zone boundaries. Consider the three points, P_1, P_2, and P_3 in Fig. 26(c). The initial **M**, $\mathbf{M}_i$, the final **M**, $\mathbf{M}_f$, and several intermediate values of **M** at each of these points are shown in Fig. 26(d). The physical mechanism of the switching required at Points P_2 and P_3 has not been thoroughly investigated. The vector $\mathbf{M}_f$ at Point P_2 is parallel to $\mathbf{M}_i$ at Point P_3. Note that as the zone boundary moves past Point P_1, **M** switches by 180°, whereas at Points P_2 and P_3, **M** switches by less than 180°. Material at a point near the rectangular zone switches first as at Point P_2 and later finishes switching as at Point P_3, resulting in a net 180° switching after both zone boundaries have passed the point.

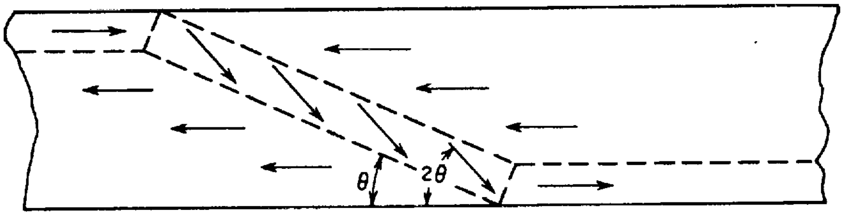

(a) DIRECTION OF MAGNETIZATION **M**

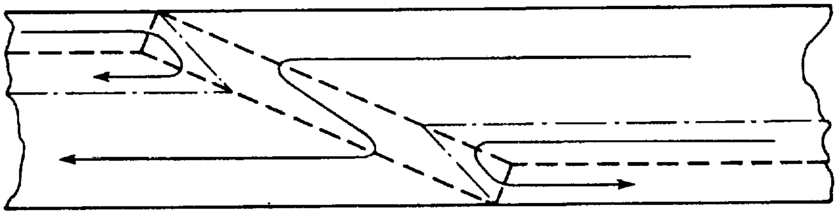

(b) MAGNETIZATION CLOSURE

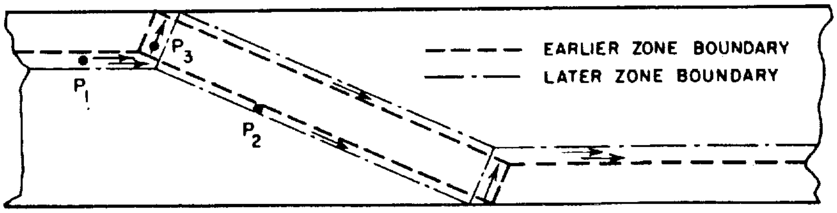

(c) SWITCHING PATHS

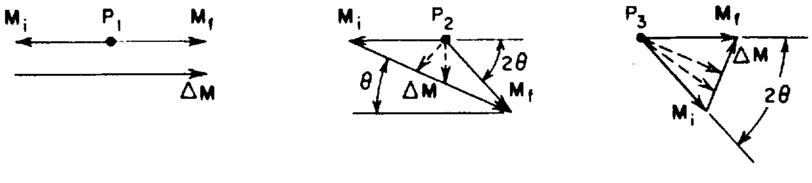

(d) SWITCHING OF **M** AT SEVERAL POINTS IN (c)

RB-3696-155

FIG. 26 SWITCHING PATH CROSSOVER ZONE

Also notice that the vectors ΔM, which are parallel to $\dot{M}$ have the same directions as the zone boundaries. Based on the definition of a switching path, these zone boundaries coincide with the switching paths. The zone boundaries at a later time in the switching process are compared in Fig. 27 to the ones obtained earlier. The angle θ that the boundary of the rectangular zone makes with the edge of the core will be determined for a particular core shape by minimization of the total magnetic energy of the system. This includes primarily zone-boundary energy and magnetostatic energy, which results from both the applied H and the H due to the existence of magnetic poles. For different angles θ, the relative widths of the switching paths near Points P_2 and P_3 in Fig. 26(c) will be different. Also, the angle between the initial and final direction of M at Points P_2 and P_3 in Fig. 26(d) will be different. These two effects change with θ in such a way as to provide the required continuity of $\dot{\phi}$ in the switching path, and also to divide $\dot{\phi}$ equally between the two branches of the switching path.

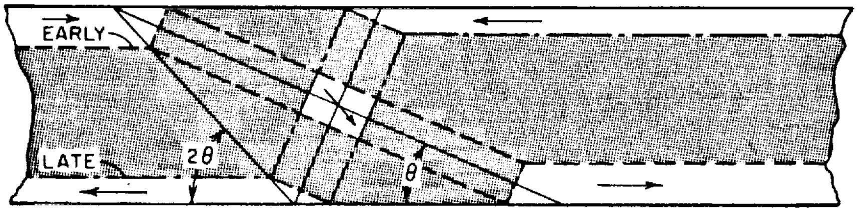

FIG. 27 COMPARISON OF CROSSOVER ZONES EARLY AND LATE IN SWITCHING

The extension of this zone model to materials whose static $B(H)$ loops do not have vertical sides results in a configuration in which all of the material between two zone patterns (the shaded regions in Fig. 27) is in the process of switching. These two zone patterns then represent the initiation and completion of switching.

This switching path crossover zone model has not been verified experimentally. It represents a first attempt at describing the details of crossover switching.

4. MACHINING OF MULTIPATH CORES

The multipath cores were ultrasonically cut from 0.050-inch thick ferrite disks. The ultrasonic tool was machined with a three dimensional pantograph from an enlarged (32x) plastic and metal pattern. This technique, although quite workable, has several problems. The major problem is the development of a taper in the cross section of a core leg. This problem is not easily remedied, and is most pronounced for very thin legs. Another problem stems from inaccurate dimensions. A leg width can easily be off by 0.05 mm, unless special care is taken in designing and constructing the ultrasonic tool. Cores N and S, used in the experiments of this report, have dimensions that are within ±0.010 mm of the design dimensions shown in Figs. 22 and 23. This accuracy was accomplished with considerable difficulty.

5. SUMMARY

The various considerations involved in designing two cores for experiments of flux switching in multipath cores are discussed. The most significant of these considerations is the junction problem. The two final core designs are shown in Fig. 22.

The problems associated with determining the leg parameters l_i, l_o, and l^{av} are considered, and an illustration of the different results corresponding to two different drive conditions on Core N (Fig. 23) is given.

The terms *switching line* and *switching path* are defined, and then used in examination of switching on cores having re-entrant shapes. Only a crude picture is given for switching in one core (Fig. 24), whereas a model is proposed for describing switching in a second core (Fig. 25).

C. DETERMINATION OF LEG PARAMETERS

A number of leg parameters must be determined for each leg of a multipath core so that switching models can be used to describe the switching phenomena (such as flux division). If the material parameters are known, these leg parameters can generally be calculated from the leg dimensions; however, typically there are significant variations in material parameters from core to core (and even from point to point within a core). Therefore, it is desirable that tne leg parameters be determined on the same core that is used in the experiments. The particular disks from which

Cores *N* and *S* were cut are believed to have had some radial variations in threshold. It is difficult, however, to measure leg parameters separately for each leg of a core. As a compromise, the material parameters were experimentally determined for two legs in series (comprising the closed path needed for the experimental measurements); these same material parameters were then used to calculate the leg parameters for each leg of of the same core. Material variations from core to core were thus accounted for, but material variations within a core were neglected.

This section describes experimental techniques for determination of the required leg parameters. The details of the experimental measurements are included in Appendix H.

1. PARAMETERS TO BE DETERMINED

A list of leg parameters is given in Table I, together with the material parameters from which these leg parameters are determined and the experiments from which the material parameters are determined.

Table I

DETERMINATION OF SWITCHING PARAMETERS

EXPERIMENTS	MATERIAL PARAMETERS	LEG PARAMETERS OR PROPERTY
(1.) Static $\phi(F)$		
(a) elastic flux switching	B_{ss} H_a	Static $\phi(F)$
(b) inelastic (and elastic) flux switching	B_r H_n H_q	
	B_s	ϕ_s
(2.) $\dot{\phi}_p(F)$	ζ_p	ρ_p
	H_0	F_0
	κ	λ
	H_0''	F_0''
	ν	ν

2. CLOSED PATH FOR TESTING

The basic experiments listed above must be performed on a closed magnetic path. Thus, some closed path in the multipath core must be chosen and flux switching in any other paths must be blocked. One way in which this blocking can be accomplished is by putting a short-circuited winding around the legs in which no switching is wanted. For example, the parameters of Core *N* [Fig. 22(a)] were determined by choosing Legs 1 and 2 for the closed path and putting a short-circuited winding on Leg 3. Similarly, for Core *S* [Fig. 22(b)], Legs 3 and 4 were chosen for the closed path and Leg *m* was linked by a short-circuited winding. If possible, this closed path should have the same cross-sectional area over its entire length, otherwise the determination of material parameters would become more involved and less accurate (*cf.* Report 1, pp. 109-112).

Blocking $\dot{\phi}$ in the legs where no switching is wanted may present a problem because of the resistance and leakage inductance of the short-circuited winding. The effectiveness of a short-circuited winding for preventing switching in a leg, if the leakage inductance of the winding is neglected, is a function of N^2/R, where N is the number of turns of the winding and R is its internal resistance. Assuming that the available aperture is filled with the short-circuited winding, R is approximately proportional to N^2, so that the effectiveness of the short-circuit is not significantly dependent upon the number of turns used in the winding. On the other hand, if the resistance of the winding is assumed to be zero and the effect of leakage inductance of the winding is calculated, the pertinent quantity is N^2/L. The leakage inductance is approximately of form $N^2K_1[ln(K_2\sqrt{N})-K_3]$, where K_1, K_2, and K_3 are constants, so that a winding of one turn that fills the aperture is better than a multiturn winding that also fills the aperture. Additional factors in favor of a single turn are (a) a better filling factor, and (b) the possibility of using a copper strap, heavier than the wire inside the aperture, in order to complete the short-circuited turn and thereby lower the resistance and leakage inductance. The short-circuited turn might also be made by immersing the leg to be blocked in mercury or some other liquid conductor. When performing the experiments, it is a good idea to check for flux switching in the blocked leg by putting a sense winding on it. Another possible means of blocking a leg in which no switching is wanted is the physical removal of the leg. This means requires either that the flux division experiments be done before the leg is removed for the determination of leg parameters, or that two separate cores are used, in which case they must be known to have the same magnetic properties.

3. STATIC $\phi(F)$ EXPERIMENT

The static $\phi(F)$ experiment consists of two measurements:

(1) Measurement of the total flux change (inelastic plus elastic) from negative remanence to any intermediate level up to positive saturation.

(2) Measurement of the elastic flux switched from negative remanence toward negative saturation.

In the first measurement, the core is set with a positive dc MMF and cleared with a negative MMF pulse whose amplitude is sufficient to attain a reproducible residual state. The flux change is measured during the CLEAR pulse, since the high CLEAR MMF produces a $\dot{\phi}(t)$ of short duration and high amplitude, which is easy to integrate. In the second measurement, the dc MMF is removed and the amplitude of the CLEAR pulse is varied. The test procedure for obtaining the static $\phi(F)$ curve is outlined in Appendix H.

The resulting static $\phi(F)$ curve is then used to determine the material parameters B_r, B_{ss}, H_a, H_n, and H_q (*cf.* Fig. 2, Sec. I-A). First, B_r is determined from

$$B_r = \frac{\phi_r}{hw} \quad . \tag{120}$$

Next, Eq. (16) is used to determine B_{ss} and H_a from the second experiment. This can be done either by using two experimental points, or by the method of least mean squares using all of the experimental data. For most applications, Eqs. (17) and (18) can be used instead of the more complicated Eqs. (A-6) and (A-7) for the determination of H_n and H_q. This can be done either by using two appropriate experimental points, one for Eq. (17) and the other for Eq. (18), or by the method of least mean squares using all of the experimental data from the first static $\phi(F)$ curve.

Once the material parameters B_{ss}, B_r, H_a, H_n, and H_q are determined, H_{th} is calculated from Eqs. (12) and (13), and then the static $\phi(F)$ curve can be computed for any leg of the same material by applying these parameters and the leg dimensions to Eqs. (16), (17), and (18).

As an example, the computed $B(H)$ curves of Core N are shown in Figs. 28(a) and (b), and experimental and computed static $\phi(F)$ curves of Legs 1 and 2 of Core N in series are compared in Figs. 28(c) and (d). The values of the material parameters are given in Fig. 28.

The agreement between the measured and the calculated static $\phi(F)$ curves is very good, except where $0 < F < H_{th}l_i$ and where $|F| \gtrsim 10\,H_{th}l_o$. The agreement for $0 < F < 0.37$ AT is not good because of some inelastic flux switching that is neglected by the model. For $|F| \gtrsim 5$ AT, the computed curve (even if ϕ_{air} is included) has poorer agreement with the experimental data than for $|F| \lesssim 5$ AT. If the experimental data were fitted for the range of values -100 $AT < F < 0$, then the value of B_{ss} obtained would be larger than the value required to obtain good agreement for $H_{th}l_i < F \lesssim 10H_{th}l_i$. We thus conclude that for the range of F values most frequently used in computer applications, the static $\phi(F)$ curve may well be described by Eqs. (16), (17) and (18).

The material parameter B_s is obtained from the experimental static $\phi(F)$ curve by choosing the value of ϕ_s to be at about five times F_0. Thus,

$$B_s = \frac{\phi_s}{hw} \quad . \tag{121}$$

From this value of B_s, one can calculate the ϕ_s value for any leg by using the h and w of the leg.

4. $\dot{\phi}_p(F)$ EXPERIMENT

The $\dot{\phi}_p(F)$ experiment consists of setting and clearing the core with rectangular pulses and measuring the peak $\dot{\phi}$ as a function of the SET pulse amplitude. The test procedure is outlined in Appendix H. As discussed in Sec. I-D-5, the resulting experimental $\dot{\phi}_p(F)$ curve is described by Eq. (87) in the high-F linear portion, and by Eq. (90) in the low-F nonlinear portion (*cf.* Fig. 15). The nonlinear approximation defines λ, F_0'', and ν. Which of these approximations is used depends upon the accuracy needed, the range of F for which the parabolic switching model is to be used, and the degree of complexity one can handle for a particular application. From these experimental parameters (which apply to the entire closed magnetic path) the corresponding material parameters can be calculated by using Eqs. (88) and (89) or Eqs. (91) and (92). These material parameters can then be used to calculate the leg parameters for any other leg of the core.

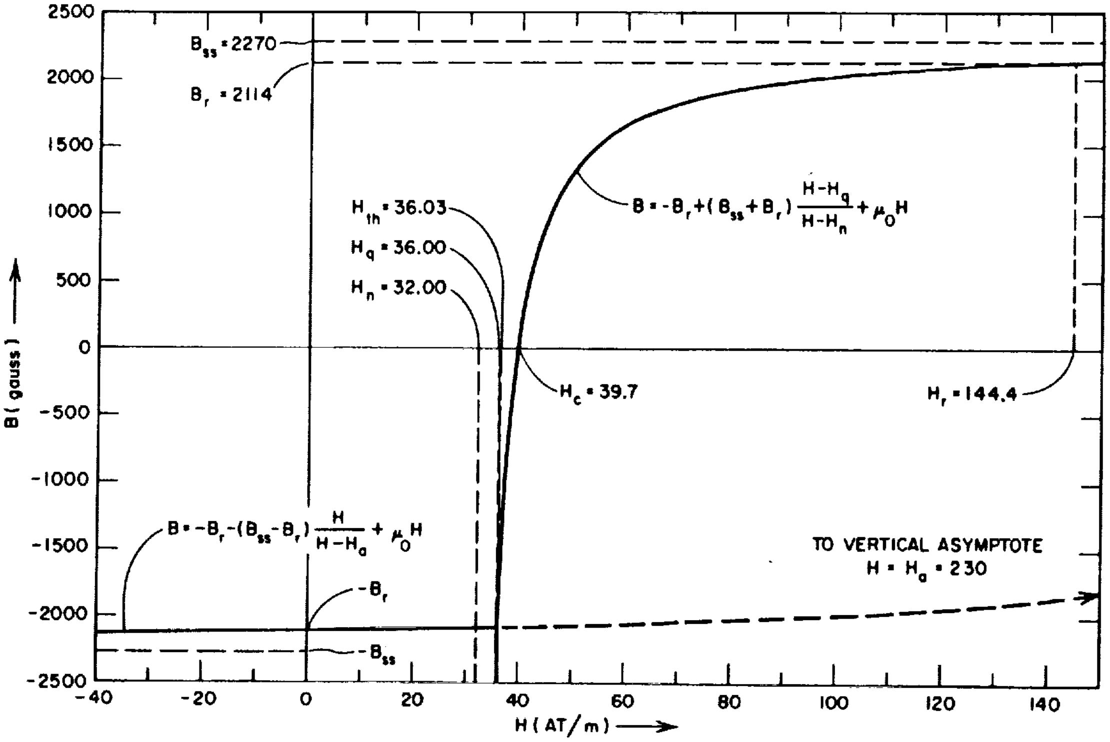

(a) B(H) CURVE

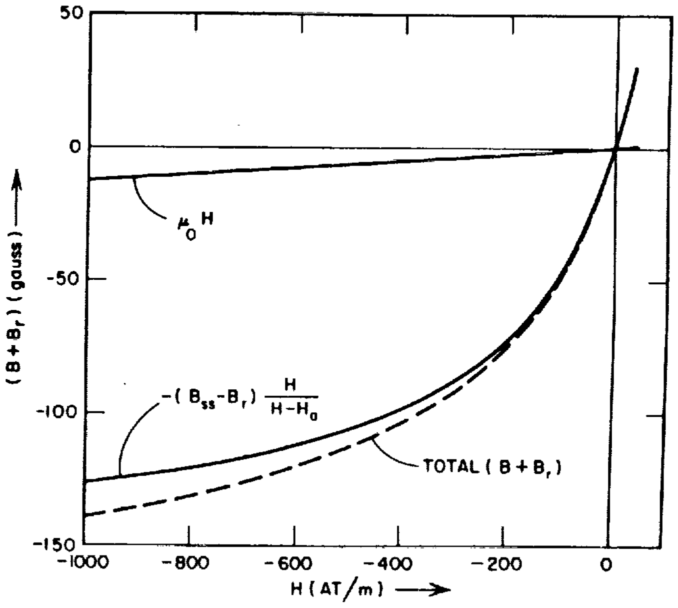

(b) B(H) IN NEGATIVE SATURATION

RD-3696 176

FIG. 28 CALCULATED AND MEASURED STATIC B(H) AND ϕ(F) CURVES FOR LEGS 1 AND 2 OF CORE N IN SERIES
$B_{ss} = 0.2270$ wb/m^2; $B_r = 0.2114$ wb/m^2; $\phi_r = 0.2567 \cdot 10^{-6}$ wb;
$H_n = 32.0$ A/m; $H_q \cong H_{th} = 36.0$ A/m; $H_a = 230$ A/m;
$l_{i12} = 10.56$mm; $l_{o23} = 16.47$mm; w = 0.927mm; h = 1.31mm.

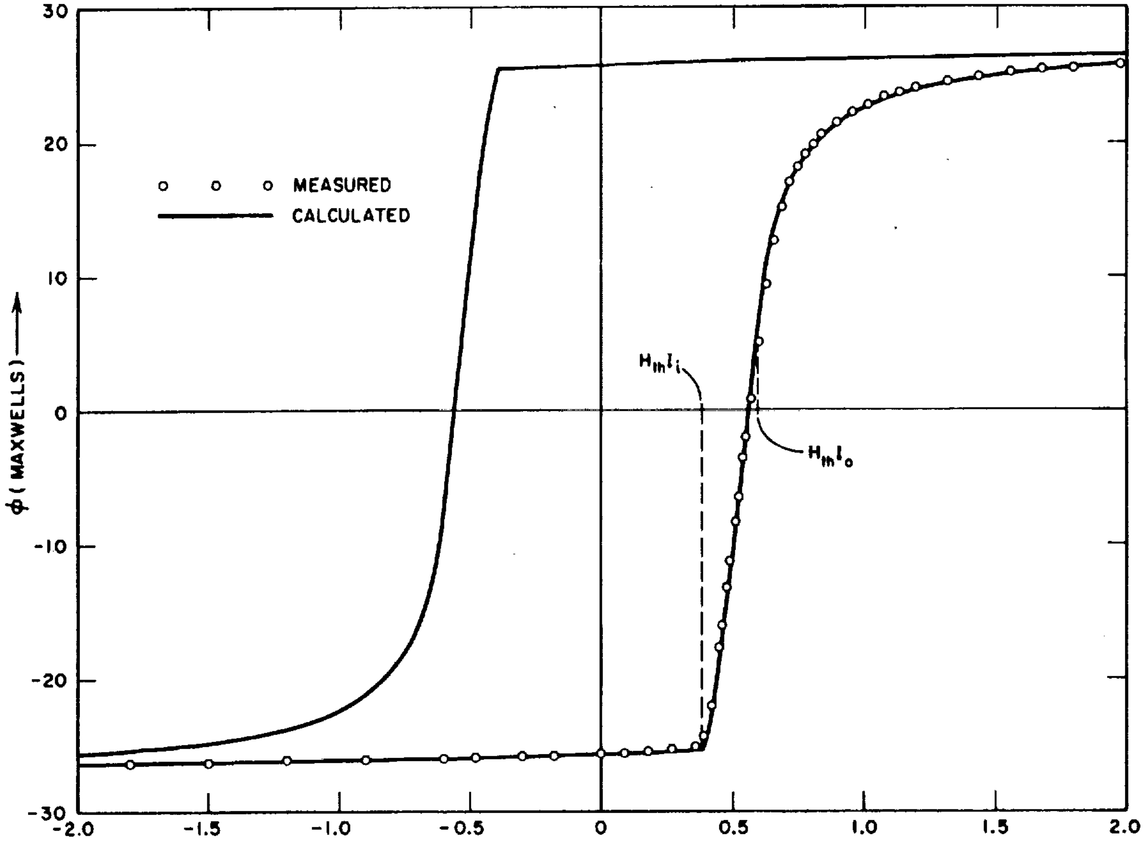

(c) φ(F) LOOP

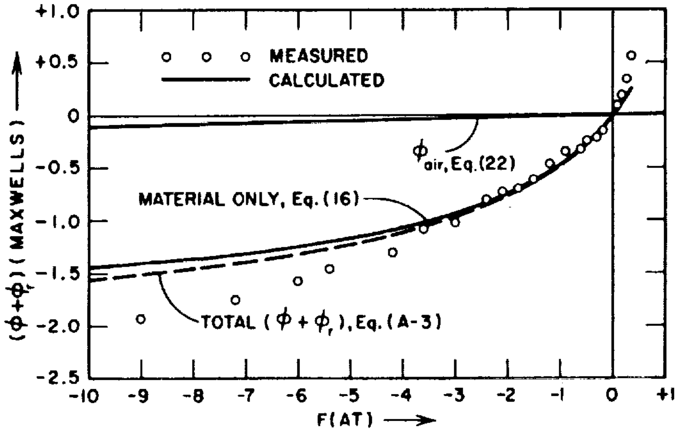

(d) φ (F) IN NEGATIVE SATURATION

RD-3696-177

FIG. 28 Concluded

A numerical example can be found in Fig. 35, where measured and calculated $\dot{\phi}_p(F)$ of Legs 3 and 4 of Core S are compared.

5. SUMMARY

The parameters which need to be determined for each leg were summarized in Table I, together with the corresponding material parameters and also the two experiments used to determine these material parameters. The requirement of choosing a closed path in the core to be tested and the problem of preventing flux switching in all other paths were treated. Both of the two experiments, the static $\phi(F)$ experiment, and the $\dot{\phi}_p(F)$ experiment, are presented and the process of using the experimental data to obtain the parameters for any leg of the same core is discussed.

D. FLUX DIVISION

1. INTRODUCTION

In dealing with flux division, we distinguish between a saturable and a nonsaturable multipath core. As explained in Sec. I-D-1, all the legs of a saturable multipath core can be brought simultaneously into saturation residual state of $\phi = \pm\phi_r$, whereas in a nonsaturable core, at least one leg is unsaturated. Flux division in a saturable core was analyzed in Sec. I-D. Due to the lack of switching models for a leg initially in a partially-switched state, flux division in a nonsaturable core has not been analyzed. Experimental data on flux division in a nonsaturable core (the Laddic) was described when the problem of flux division was first introduced.[6]

In this part, we first show results from extending the experimental investigation of flux division in a nonsaturable core. Second, verification for the analysis of flux division in a saturable core (Sec. I-D) is given by comparing measured and computed plots of D versus NI for various load levels. Along with this verification, the effects of various factors (such as ϕ_r/ϕ_s, leg parameters, load levels, and l_4/l_3) on D are investigated.

2. FLUX DIVISION IN A NONSATURABLE CORE

a. EXPERIMENTATION

The nonsaturable core used in the experiments on flux division was Core N [Fig. 22(a)], whose three legs are equal in cross-sectional area, but different in length. As explained in Part B-1, this three-leg core was especially designed and fabricated for the experiment on flux division. The manner of dividing Core *N* into legs and the lengths of these legs are given in Fig. 23.

In order to obtain a reproducible initial state, Core *N* was heated to slightly above its Curie temperature for about two minutes. In this way, the entire core was brought into a uniformly demagnetized state before any measurement was performed.

First, MMF *NI* was applied to Leg 1 [Fig. 23(a)], and the resulting $\dot{\phi}_1$, $\dot{\phi}_2$, and $\dot{\phi}_3$ were sensed and integrated. With no load on either leg, the experimental setup was similar to the one shown in Report 1, Fig. 72(a), p. 75. The bipolar SET and CLEAR current pulses were equal in amplitude and duration (5 microseconds). As *NI* was monotonically increased from zero, residual $\Delta\phi_1$, $\Delta\phi_2$, and $\Delta\phi_3$ were measured as a function of *NI*, using the flux-reference technique (*cf.* Appendix F). The same procedure was then repeated with the *NI* drive applied to Leg 3.

b. RESULTS

Plots of measured $\Delta\phi_1$, $\Delta\phi_2$, and $\Delta\phi_3$ versus *NI* are shown in Fig. 29. Figure 29(a) is for *NI* applied to Leg 1, and Fig. 29(b) is for *NI* applied to Leg 3. Corresponding plots of flux division ratio versus *NI* are shown in Fig. 30.

Oscillograms of $\dot{\phi}_1$, $\dot{\phi}_2$, $\dot{\phi}_3$ and *NI* for the case of drive on Leg 1 are shown in Fig. 31 for $NI = 0.7\ AT$, and in Fig. 32 for $NI = 3.0\ AT$. These oscillograms were taken at a temperature of 29°C and repetition rate of 500 cps. The waveforms of $\dot{\phi}_1$, $\dot{\phi}_2$, and $\dot{\phi}_3$ during the SET time for the case of $NI = 3.0\ AT$ are shown in Fig. 32(a), an enlargement of $\dot{\phi}_3$ during the SET time is shown in Fig. 32(b), and the waveforms of $\dot{\phi}_1$, $\dot{\phi}_2$, and $\dot{\phi}_3$ during the fall time are shown in Fig. 32(c).

These experimental data will now be discussed.

c. DISCUSSION

(1) In examining Fig. 30, the inaccuracy of the $\Delta\phi$ measurement should be considered. The flux change in each leg was measured by means of the flux reference (*cf.* Appendix F), whose error is less than ±0.1 maxwell turns. The lower *NI* is, the smaller is the measured $\Delta\phi$ in the longer leg; hence, the

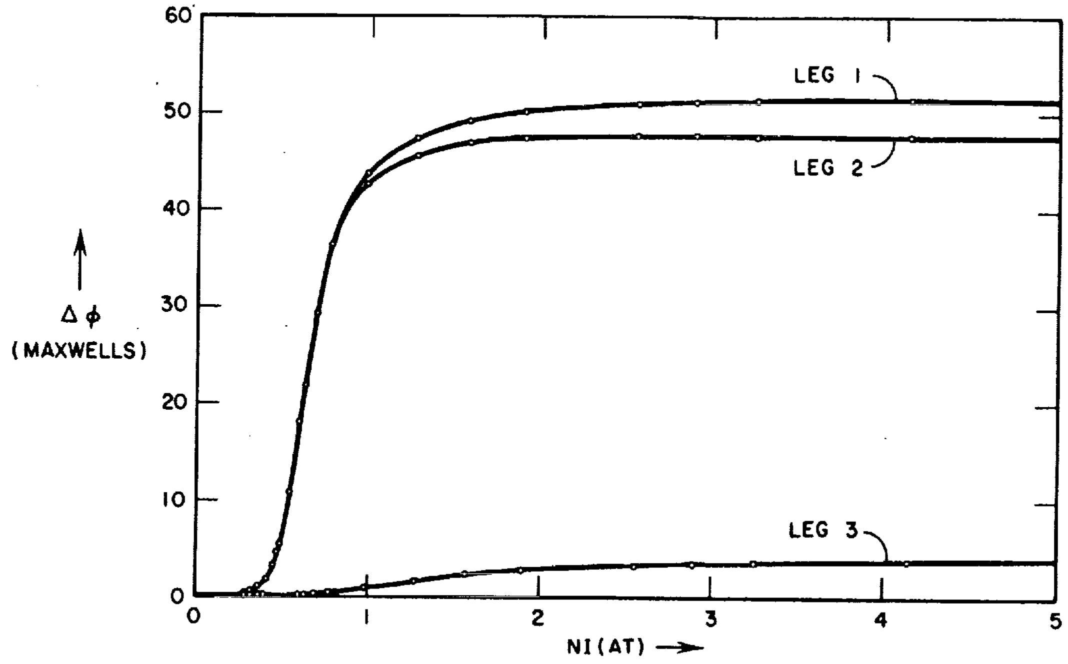

(a) DRIVE ON LEG 1

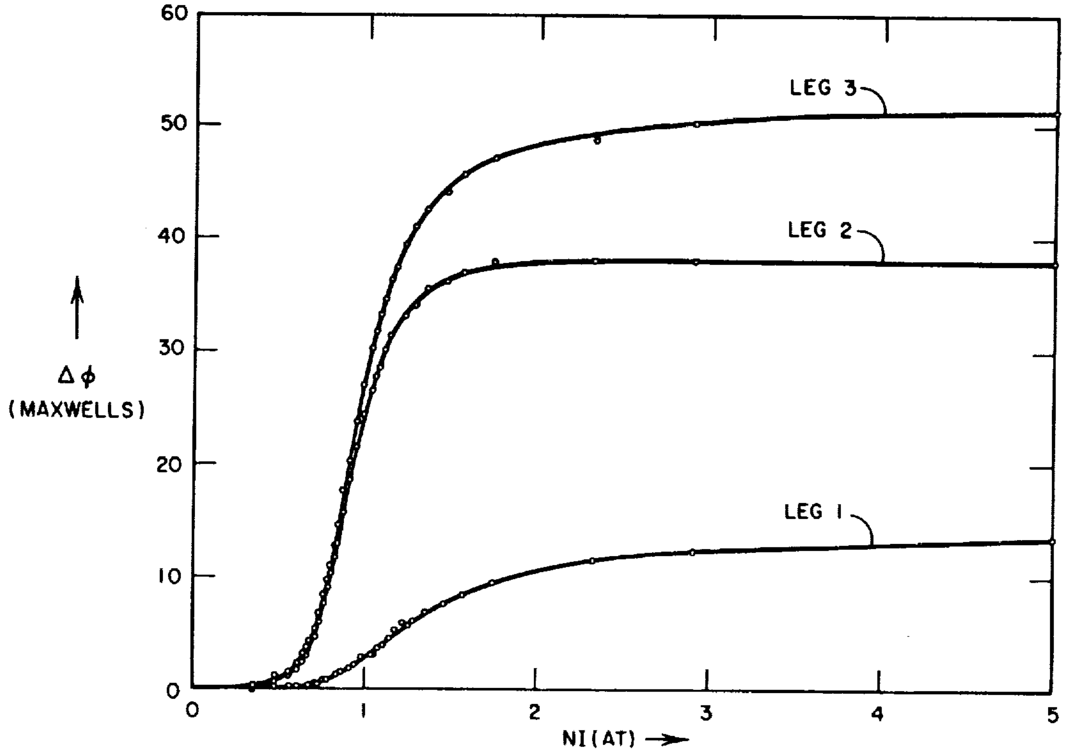

(b) DRIVE ON LEG 3

RC-3696-178

FIG. 29 MEASURED FLUX DIVISION IN A NONSATURABLE CORE

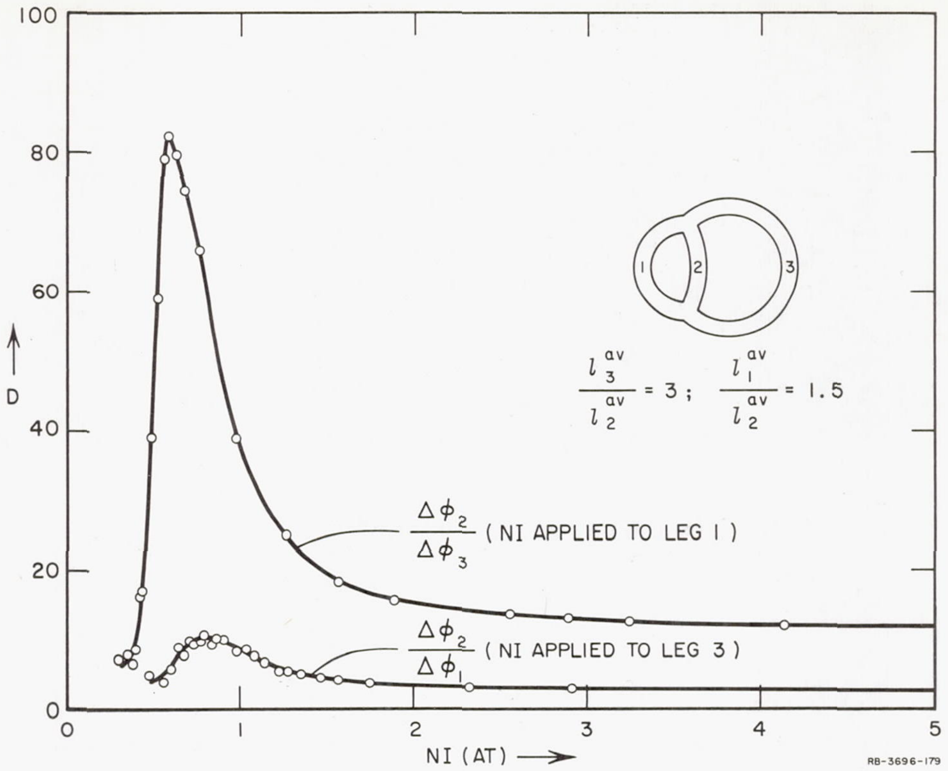

FIG. 30 FLUX-DIVISION RATIO IN NONSATURABLE CORE N

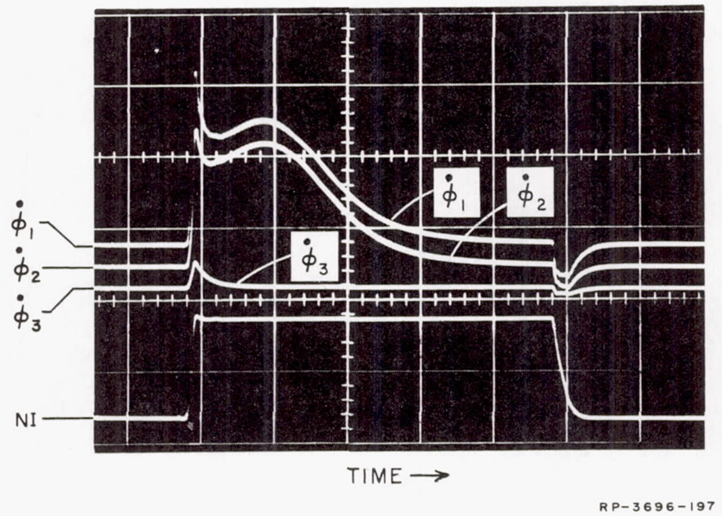

FIG. 31 FLUX-DIVISION OSCILLOGRAMS OF CORE N FOR NI = 0.7 AT ON LEG 1
Time scale = 1 μsec/major div.;
$\dot{\phi}$ scale = 0.09 (V/T)/major div.

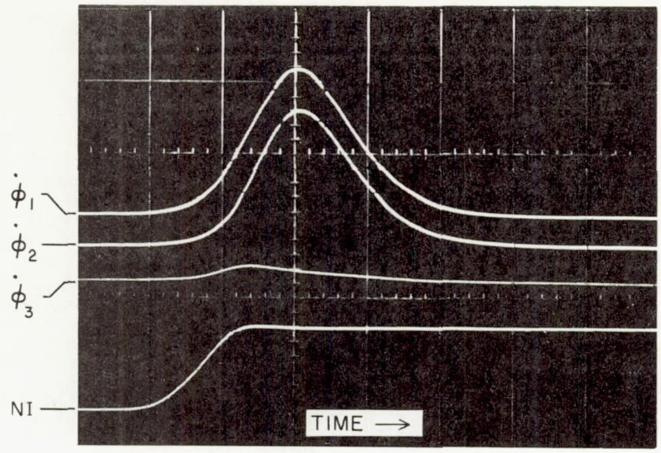

(a) SET TIME

Time scale = 0.1 μsec/major div.

$\dot{\phi}$ scale = 1.6 (v/T)/major div.

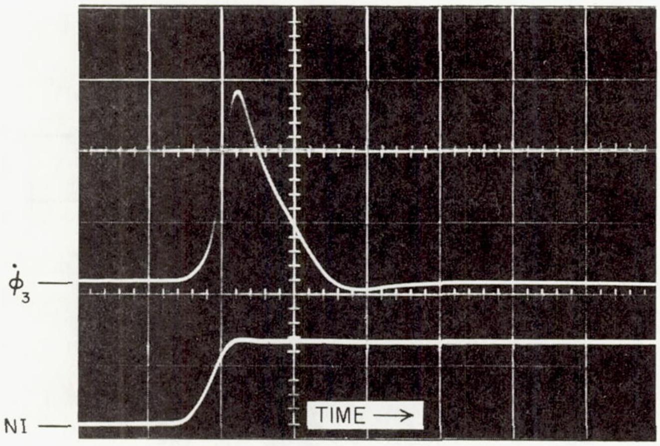

(b) EXPANDED $\dot{\phi}_3(t)$

DURING SET TIME

Time scale = 0.2 μsec/major div.

$\dot{\phi}$ scale = 0.12 (v/T)/major div.

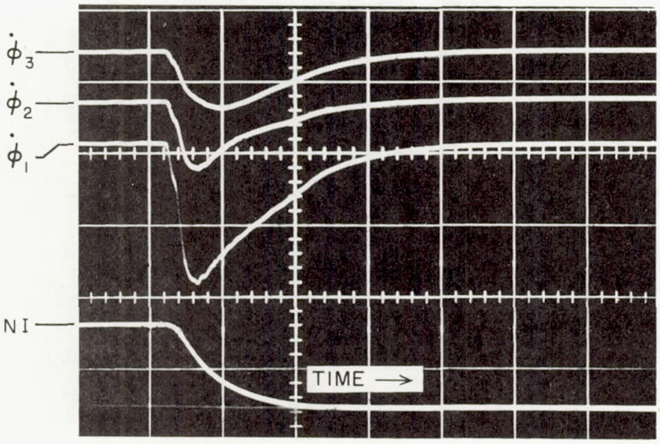

(c) FALL TIME

Time scale = 0.2 μsec/major div.

$\dot{\phi}$ scale = 0.029 (v/T)/major div.

RP-3696-198

FIG. 32 FLUX-DIVISION OSCILLOGRAMS OF CORE N FOR NI = 3.0 AT ON LEG 1 higher is the error. Thus, when *NI* is applied to Leg 1, at $NI = 0.592$ *AT*, $\Delta\phi_2/\Delta\phi_3$ reaches a peak of $82.3\,{}^{+27.7}_{-16.5}$ (*i.e.*, the error is less than ${}^{+33.6}_{-20.0}$ %); however, for $NI = 4.138$ *AT*, $(\Delta\phi_2/\Delta\phi_3) = 11.91 \pm 0.16$, (*i.e.*, the error is less than ±1.34%). When *NI* is applied to Leg 3, at $NI = 0.794$ *AT*, $\Delta\phi_2/\Delta\phi_1$ reaches a peak of $10.7\,{}^{+10.6}_{-\ 3.6}$, (*i.e.*, the error is less than ${}^{+99.0}_{-33.7}$ %); however, for $NI = 2.914$ *AT*, $(\Delta\phi_2/\Delta\phi_1) = 3.08 \pm 0.12$, (*i.e.*, the error is less than ±3.9%). These errors for the low values of *NI* could have been decreased by increasing the number of turns of the sense windings on the longer legs. This improvement was made in measuring the flux division in Core *S*, as will be shown later.

(2) It is hard to compare our experimental data with the data in Refs. 6 and 7 because we do not know what material was used for fabrication of the Laddic reported on in Refs. 6 and 7. There is, however, similarity between the plots of $\Delta\phi_2$ and $\Delta\phi_3$ for the ratio of $l_3/l_2 = 3$, which is common to Refs. 6 and 7 and Fig. 29(a), except for the following. In Refs. 6 and 7 [see also Report 1, Fig. 72(b), p.75], $\Delta\phi_2$ and $\Delta\phi_3$ versus *NI* is less curved and rises with a higher slope than in Fig. 29(a). This difference might have been caused by the use of material of higher threshold and squarer $B(H)$ loop in Refs. 6 and 7. Another difference between these sets of data is that in Fig. 29(a), $\Delta\phi_2$ and $\Delta\phi_3$ versus *NI* have small but finite slope at high values of *NI* (say, above 2 *AT*), whereas in Refs. 6 and 7, $\Delta\phi_2$ and $\Delta\phi_3$ are essentially constant in this range of *NI*.

(3) In the plots of *D* versus *NI* for leg ratios of 3 and 1.5 (Fig. 30), we observe that in each core, *D* reaches a peak at some relatively low value of *NI*. In order to understand what causes this peak to occur, let us refer also to Fig. 29(a), where *NI* is applied to Leg 1. As *NI* is increased from zero, there are slight inelastic flux changes in all legs until at around $NI = 0.4$ *AT*, *H* in Legs 1 and 2 reaches the threshold value. A further increase in *NI* causes an appreciable inelastic $\Delta\phi$ in Legs 1 and 2, but $\Delta\phi_3$ hardly increases, since H_3 is below the (soft) threshold. In this region of

NI, therefore, $\Delta\phi_2/\Delta\phi_3$ increases with NI. As NI exceeds $\sim 0.6\,AT$, H_3 exceeds the (soft) threshold, and $\Delta\phi_3$ increases. For values of NI above 0.8 AT, $\Delta\phi_1$ and $\Delta\phi_2$ start to level off due to saturation, but $\Delta\phi_3$ continues to rise. This calls for a decrease in $\Delta\phi_2/\Delta\phi_3$. Thus, at a value of NI somewhere between 0.6 AT and 0.8 AT (Fig. 30), $\Delta\phi_2/\Delta\phi_3$ reaches a peak. A similar mechanism causes the peak in $\Delta\phi_2/\Delta\phi_1$ versus NI in the case where NI is applied to Leg 3 except that since $l_3 > l_1$, this peak is reached at a value of NI higher than when NI is applied to Leg 1.

(4) The oscillograms of $\dot{\phi}_2$ and $\dot{\phi}_3$, (Figs. 31 and 32), are similar to the ones in Ref. 7, except that in Ref. 7 these oscillograms were not extended to the fall time. As in Ref. 7, $\dot{\phi}_3$ becomes negative (while NI is still on) if NI is high enough. The explanation for this phenomenon can be found in Report 1, pp. 77-80.

(5) The waveshapes of $\dot{\phi}_1$, $\dot{\phi}_2$, and $\dot{\phi}_3$ during the fall time of NI were predicted in Report 1 [Fig. 75(b), p. 79]. Comparing peak values of $\dot{\phi}$ in Report 1, $|\dot{\phi}_{3p}| > |\dot{\phi}_{2p}|$, whereas in the oscillograms of Fig. 32(c), $|\dot{\phi}_{3p}| < |\dot{\phi}_{2p}|$. This disagreement stems from the following reason: Prediction of the waveforms was based on the assumption that since Leg 3 is in a soft state and Leg 2 is in a hard state, the slope $\epsilon = (d\phi)_\epsilon/dF$ in Leg 3 is higher than in Leg 2. Such an argument is correct but incomplete; there is an additional factor, *i.e.*, Leg 3 being longer than Leg 2, which acts in an opposite direction. Which factor is predominant, depends on the circumstances. Apparently, the factor of leg-length ratio is predominant in Fig. 32(c), whereas in Fig. 75(b) of Report 1, the soft-state factor was assumed predominant. Based on this point, and since $(d\phi)_\epsilon/dF$ varies during the fall time, instead of comparing $\dot{\phi}_{p2}$ and and $\dot{\phi}_{p3}$, we should have compared $\Delta\phi_{\epsilon 2}$ and $\Delta\phi_{\epsilon 3}$ during the fall time. When this comparison is made in Fig. 32(c), we find that $|\Delta\phi_{\epsilon 3}| > |\Delta\phi_{\epsilon 2}|$, which agrees with the basic assumptions made in Report 1 in predicting the waveshapes of $\dot{\phi}$ in the three legs.

3. FLUX DIVISION IN A SATURABLE CORE

a. EXPERIMENTATION

Core *S* [Fig. 22(b)] was designed and fabricated specially for measurement of flux division in a saturable core. The manner of dividing this saturable core into Legs m, 3, and 4 and the dimensions of these legs are also shown in Fig. 22(b).

The experimental setup followed the one shown in Fig. 10, p. 26. Leg 4 was first unloaded. The core was cleared to a negative remanent state (not shown in Fig. 10). A current pulse of amplitude I and duration T was then applied to an N-turn winding on Leg m in the SET direction, and the net flux change in Leg m, $\Delta\phi_m$, was measured. The magnitudes of I and T were adjusted until $\Delta\phi_m$ was equal to $2\phi_r$, which is the maximum possible inelastic $\Delta\phi$ in Leg 3 (or Leg 4). For each pair of values of I and T that yielded $\Delta\phi_m = 2\phi_r$, the values of $\Delta\phi_3$, $\Delta\phi_4$, and I were recorded.

This procedure was repeated for three values of load:

(1) $N_L = 2$, $R_L = 1.02$ ohm, *i.e.*, $(N_L^2/R_L) = 3.926\ T^2/\text{ohm}$.

(2) $N_L = 1$, $R_L = 0.093$ ohm, *i.e.*, $(N_L^2/R_L) = 10.66\ T^2/\text{ohm}$.

(3) $N_L = 2$, $R_L = 0.1$ ohm, *i.e.*, $(N_L^2/R_L) = 40.00\ T^2/\text{ohm}$.

b. RESULTS

The resulting plots of $\Delta\phi_3$ and $\Delta\phi_4$ versus NI are shown in Fig. 33 for the four values of N_L^2/R_L. The corresponding plots of D will later be compared with calculated plots.

Oscillograms of $\dot{\phi}_m$, $\dot{\phi}_3$, $\dot{\phi}_4$, and NI are shown in Fig. 34 for the case of $NI = 0.8\ AT$ and Leg 4 unloaded. These oscillograms were taken at a temperature of 29°C and a repetition rate of 60 cps. Note that $NI = 0.8\ AT$ is below the minimum value of NI that enables $\Delta\phi_m$ to be equal to $2\phi_r$, as is evident from Fig. 33(a). These oscillograms were taken in order to explain a phenomenon associated with peaking of D in a saturable core, as will be discussed later.

Our next objective is to compare measured and calculated plots of D versus NI. In order to calculate these plots, we first must determine the leg parameters.

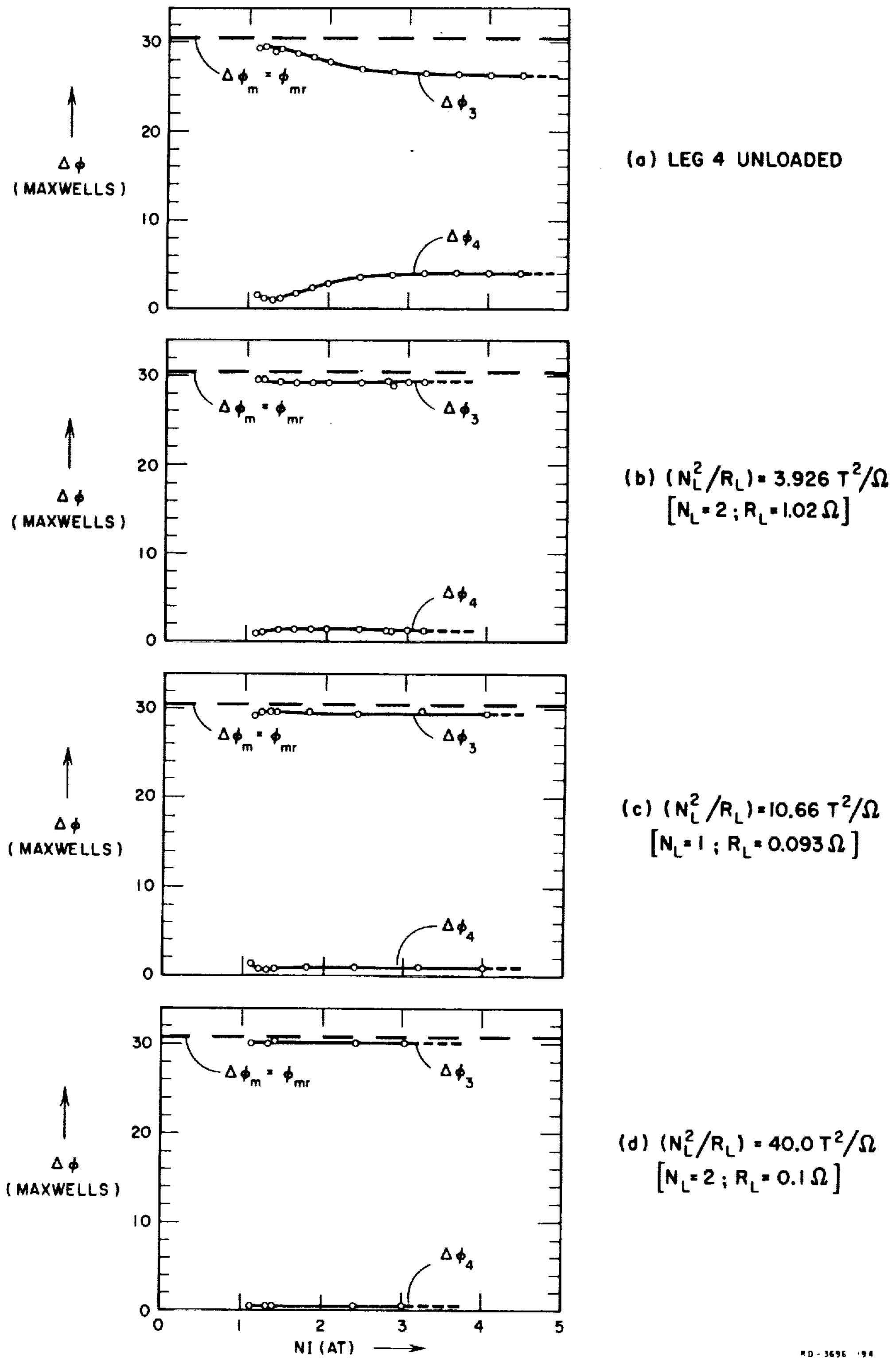

(a) LEG 4 UNLOADED

(b) $(N_L^2/R_L) = 3.926\ T^2/\Omega$
$[N_L = 2 ; R_L = 1.02\,\Omega]$

(c) $(N_L^2/R_L) = 10.66\ T^2/\Omega$
$[N_L = 1 ; R_L = 0.093\,\Omega]$

(d) $(N_L^2/R_L) = 40.0\ T^2/\Omega$
$[N_L = 2 ; R_L = 0.1\,\Omega]$

FIG. 33 FLUX-DIVISION IN SATURABLE CORE S FOR SEVERAL LOAD VALUES

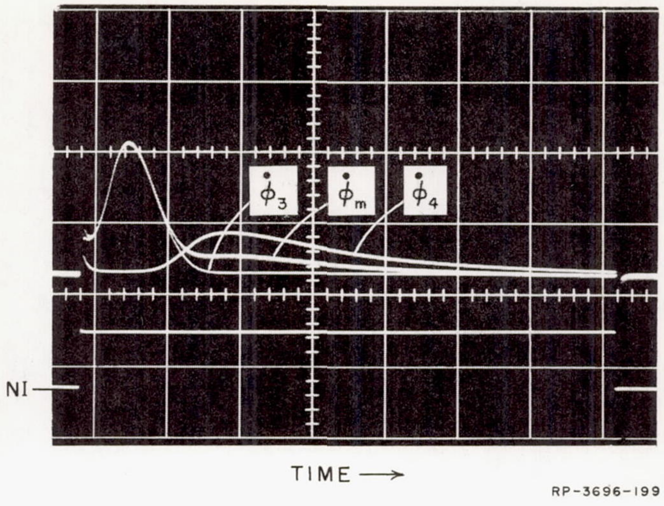

FIG. 34 FLUX-DIVISION OSCILLOGRAMS OF CORE S WITH NI = 0.8 AT
Time scale = 4 μsec/major div.;
$\dot{\phi}_m$ and $\dot{\phi}_3$ scale = 0.046 (V/T)/major div.;
$\dot{\phi}_4$ scale = 0.020 (V/T)/major div.

c. LEG PARAMETERS

The inelastic-switching leg parameters were measured in the same manner as described in Part C-4. Leg m [Fig. 22(b)] was wrapped by a short-circuited winding, and Legs 3 and 4 in series were tested as a single-leg core. The measured peak $\dot{\phi}$, $\dot{\phi}_{p34}$, is recorded versus the applied MMF, F_{34}, in Fig. 35.

By extending the linear portion of $\dot{\phi}_{p34}$ versus F_{34} (dashed line in Fig. 35), it is found that $F_{034} = 0.85\ AT$ and $\rho_{34p} = 0.75$ ohm/T^2. Following Fig. 22(b), the leg dimensions are as follows: $l_m^{av} = 16.845$ mm, $l_3^{av} = 5.040$ mm, $l_4^{av} = 8.960$ mm; $A_3 = A_4 = (A_m/2) = 0.665$ mm^2. Substituting $l_{34}^{av} = l_3^{av} + l_4^{av} = 14.000$ mm and $A_{34} = A_3 = A_4 = 0.665$ mm^2 into Eqs. (88) and (89), we find that $H_0 = 60.6\ AT/m$ and $\zeta_p = 15{,}800$ ohms/(T^2m). Substituting the leg dimensions and the values of H_0 and ζ_p into Eqs. (88) and (89), the leg parameters in the linear region of $\dot{\phi}_p$ versus F are found to be as follows: $F_{0m} = 1.0227\ AT$, $F_{03} = 0.306\ AT$, $F_{04} = 0.544\ AT$, $\rho_{mp} = 1.246$ ohms/T^2, $\rho_{3p} = 2.083$ ohms/T^2, and $\rho_{4p} = 1.172$ ohms/T^2.

The nonlinear portion of $\dot{\phi}_{p34}$ versus F_{34}, (Sec. I-D-5-b) is approximated by the solid line in Fig. 35. With reference to Eq. (90), p. 40,

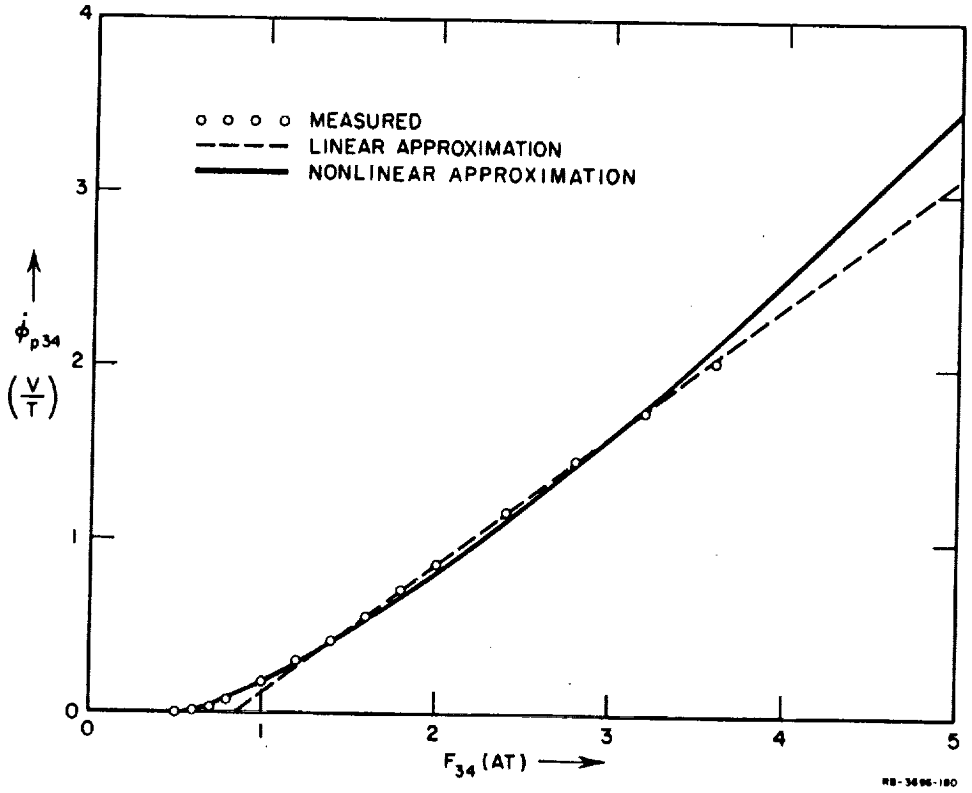

FIG. 35 $\dot{\phi}_p$ vs. F OF LEGS 3 AND 4 OF CORE S IN SERIES

$\lambda_{34} = 0.5$ ohm/$(T^{\nu+1}A^{\nu-1})$, $F''_{034} = 0.55$ AT, and $\nu = 1.3$. Substituting the values of l^{av}_{34} and A_{34} into Eqs. (91) and (92), we find that $H''_0 = 39.3$ AT/m, and $\kappa = 10{,}520$ ohms/$(T^{\nu+1}A^{\nu-1}m^{2-\nu})$. Hence, the leg parameters in the nonlinear region of $\dot{\phi}_p$ versus F are as follows: $F''_{0s} = 0.662$ AT, $F''_{03} = 0.198$ AT, $F''_{04} = 0.352$ AT, and, in units of ohms/$T^{2.3}A^{0.3}$, $\lambda_s = 0.357$, $\lambda_3 = 0.855$ and $\lambda_4 = 0.405$.

These values of parameters were then employed in computing D versus NI for various load levels, to be discussed next.

d. COMPUTED *D* VERSUS MEASURED *D*

Computation of flux-division ratio D versus applied MMF NI was based on Eqs. (70) through (73). The ratio ϕ_r/ϕ_s was measured (*cf.* Part C-3) and found to be slightly larger than 0.9, and was rounded to 0.9. Later, we shall examine the effect of ϕ_r/ϕ_s on D. The computation of D was performed on the Burroughs 220 computer, using the ALGOL programing language.

For a given value of N_L^2/R_L and for each value of NI, the computation steps are described as follows: Initial numerical values of the parameters of each of the three legs are assumed to be F_0 and ρ_p. These six parameter values are substituted into Eqs. (70) through (72) in order to solve for p transcendentally. Switching time T[Eq. (D-14)], is then evaluated and substituted into Eq. (D-12) in order to determine $\bar{F}_3$, which is then substituted into Eq. (D-4) in order to determine $\bar{F}_s$. The expression

$$\bar{F}_4 = \bar{F}_3 - \frac{\left(\frac{N_L^2}{R_L}\right)\left(\frac{\phi_r}{\phi_s} - \frac{\phi_{3f}}{\phi_s}\right)}{T/\phi_s} \tag{122}$$

is then used to determine $\bar{F}_4$ [Eq. (122) is obtained by substituting $\bar{\dot{\phi}}_4 = \Delta\phi_4/T = (\phi_r + \phi_{4f})/T = (\phi_r - \phi_{3f})/T$, Eqs. (60) and (62), into Eq. (54)].

For each leg whose parameters ν, λ and F_0'' are known, substitution of $\bar{F}$ into Eqs (94) and (95) yields the first approximation for the leg parameters ρ_p' and F_0'. These six leg parameters replace the initial values of leg parameters, and the same computation steps are repeated. This procedure is repeated several times until one of the variables, *e.g.*, $\bar{F}_3$, has changed by less than 0.1% in the last cycle. The values of p and q in the last cycle are substituted into Eq. (73) in order to compute D.

Computed plots of D versus NI for various values of N_L^2/R_L are compared in Fig. 36 with experimental data. The accuracy of the experimental measurement is lower as NI becomes smaller, since when $\Delta\phi_4$ becomes smaller, the noise level is more significant. The error in $\Delta\phi$ due to the noise level in the flux-reference (*cf.* Appendix F) is less than $\pm 0.1/N_o$ maxwells, where N_o is the number of turns of the sense winding. For the cases of $(N_L^2/R_L) = 0$, 3.926, 10.66, and 40.0, N_o on Leg 4 was equal to 2, 20, 10, and 20, respectively.

e. DISCUSSION

(1) The calculated D versus NI (Fig. 36,) is far from coinciding with the measured curves. However, in view of the complexity of flux division, these results are nevertheless encouraging. The measured D decreases as NI increases

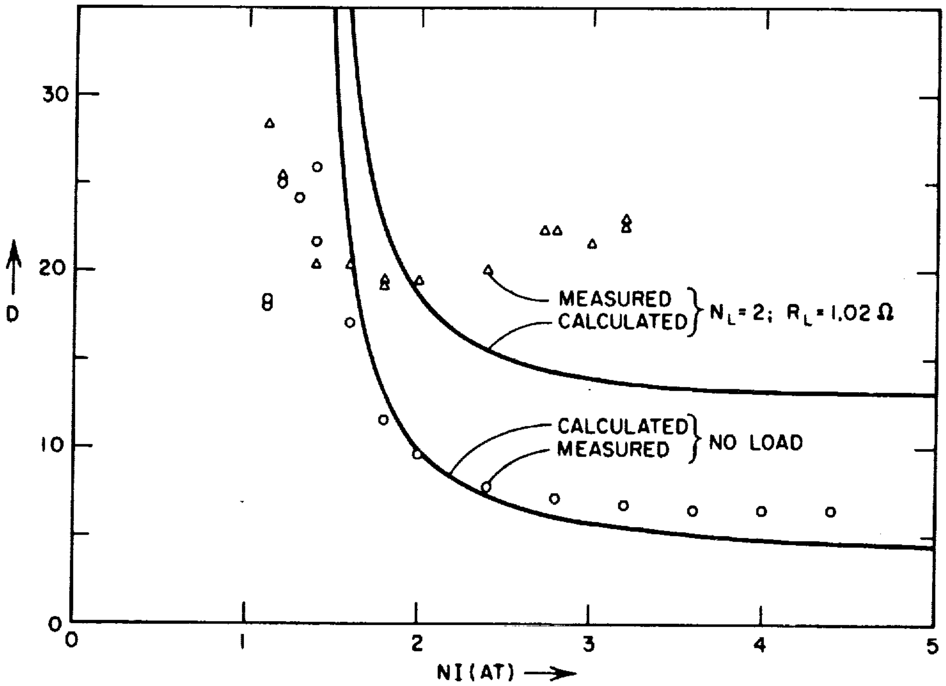

(a) $(N_L^2/R_L) = 0$ AND $3.926\ T^2/\Omega$

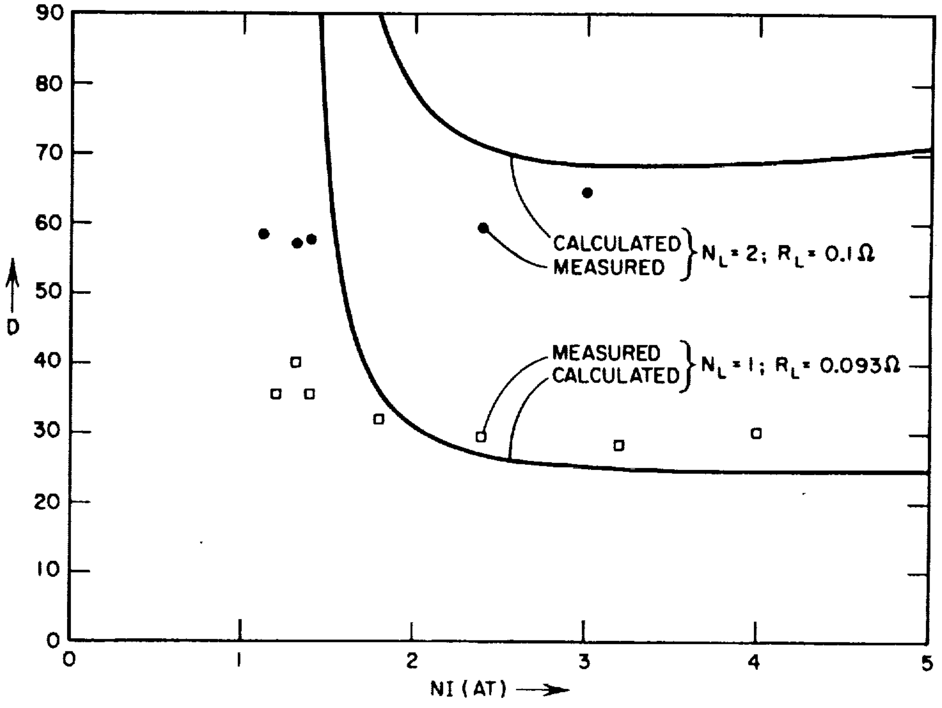

(b) $(N_L^2/R_L) = 10.66$ AND $40.00\ T^2/\Omega$

RC-3696-181

FIG. 36 CALCULATED AND MEASURED D vs. NI WITH (N_L^2/R_L) AS A PARAMETER
$\phi_r/\phi_s = 0.9$

above, say, 1.3 *AT*, until, at a certain value of *NI*, *D* reaches a minimum. (No such minimum is reached in the no-load case for *NI* below 5.0 *AT*.) The computed *D* versus *NI* for the loaded case also has a minimum point that becomes more pronounced as N_L^2/R_L increases (see also Fig. 39 later). When we first computed *D* versus *NI*, we assumed constant F_0 and ρ_p in each leg, and the resulting curves were monotonically decreasing for all values of N_L^2/R_L. Since the effect of the curvature of $\dot{\phi}_p$ versus *F* was accounted for in computing the curves in Fig. 36, it may be concluded that the minimum of *D* versus *NI* is associated with the nonlinearity of $\dot{\phi}_p$ versus *F*. Since the assumption of constant F_0 and ρ_p is valid for high values of *NI*, the effect of including the nonlinearity of $\dot{\phi}_p$ versus *F* is not to raise *D* at high values of *NI*, but rather to drop *D* at the low values of *NI*. We may conclude, therefore, that for values of *NI* larger than *NI* at the minimum point, *D* rises and approaches an asymptote as $NI \to \infty$.

(2) The main discrepancy between the computed and measured curves is around the low values of *NI*, where the measured *D* reaches maximum. Obviously, the analysis in Sec. I-D does not account for the mechanism that causes *D* to reach maximum. This phenomenon is explained qualitatively as follows. There is a minimum value of *NI* (1.1 *AT* in this case), below which $\Delta\phi_m < 2\phi_r$, even if $T \to \infty$. Around this low value of *NI*, flux switching follows a certain sequence. First, flux switching occurs essentially only in Legs *m* and 3, because $H_4 < H_{th}$. Toward the end of the flux switching in Leg 3, F_3 increases because Leg 3 reaches the wing of the static $\phi(F)$ curve near saturation, while Leg *m* is near a demagnetized state. Such a redistribution of *NI* into higher F_3 and lower F_m follows the requirement that $\dot{\phi}_m = \dot{\phi}_3$ and the fact that $A_m > A_3$. The increase in F_3 ($=F_4$ in the no-load case) increases F_4 beyond the static threshold value of Leg 4, and Leg 4 is then able to switch inelastically. Leg 4, therefore, switches only *after* Leg 3 completes most of its switching. This conclusion is verified experimentally in Fig. 34, where *NI* was chosen below 1.1 *AT* in order to emphasize the delay in $\dot{\phi}_4$ relative to $\dot{\phi}_3$. Coming back to the plot of *D* versus *NI*, as *NI* is increased beyond 1.1 *AT*, the pulse duration *T* must decrease in order to keep $\Delta\phi_m = 2\phi_r$. Such a decrease in *T* will decrease $\Delta\phi_4$ (because when *NI* is cut off, Leg 4 is still switching), but hardly affect $\Delta\phi_3$ (because Leg 3 has already completed switching). The amount dropped in $\Delta\phi_4$ is equal to the amount raised in $\Delta\phi_3$, because $\Delta\phi_3 + \Delta\phi_4 = 2\phi_r =$ constant. Such an increase in $\Delta\phi_3$ results from the increase in *NI*. This increase in $\Delta\phi_3$ and decrease in $\Delta\phi_4$ explain why $D(= \Delta\phi_3/\Delta\phi_4)$ increases with *NI*. These variations in $\Delta\phi_3$ and $\Delta\phi_4$ can be seen in Figs. 33(a) and (c). In Fig. 33(d) the load is so high, that H_4 does not exceed H_{th}, hence

this phenomenon does not occur. It is not understood why this phenomenon was not observed in Fig. 33(b). As NI increases further, it becomes high enough to switch all legs simultaneously, as assumed in our analysis, and D decreases with NI. At the transition between the region where D increases with NI and the region where D decreases with NI, D reaches its maximum value. Note that this mechanism is entirely different than the mechanism that causes D to reach maximum in Core N, as discussed previously. In fact, since all legs in Core N have the same cross-sectional area, the phenomenon described here cannot occur in Core N.

(3) The measured value $(\phi_r/\phi_s) = 0.9$ [hence, following Eq. (68), $\delta = (1 - 0.9)/(1 + 0.9) = 0.05263$] was used in order to compute D versus NI, Fig. 36. One may wonder how sensitive D is to ϕ_r/ϕ_s; in other words, how crucial is the measurement of ϕ_r/ϕ_s. To answer this question, D versus NI in the no-load case was computed for various values of ϕ_r/ϕ_s, ranging from 0.86 to 0.96. The resulting plots are shown in Fig. 37. We conclude from these plots that, considering the agreement between calculated and measured D versus NI in general, determination of ϕ_r/ϕ_s need not be within tight tolerances.

(4) In computing D versus NI, Fig. 36, variation in leg parameters with NI were accounted for. However, in doing so, the computation was much more complex than if the leg parameters were constant. In several cases, the accuracy of the results may be sacrificed somewhat in order to simplify the computation procedure. To have an idea of how much accuracy is sacrificed by such an assumption, D versus NI in the no-load case was recalculated, assuming constant leg parameters obtained from the linear portion of $\dot{B}_p$ versus H. The resulting curve is compared in Fig. 38 with the measured curve and the curve whose calculation was based on assuming that F_0' and ρ_p' of each leg varies with NI. As expected, assuming constant F_0 and ρ_p in each leg for low values of NI results in a substantial error, but for medium and high values of NI, such an assumption is certainly justified. To get better agreement at the low values of NI, yet to keep the computation simpler, the $\dot{\phi}_p$ *vs.* F might be piecewise linearized into two regions.

(5) For future reference, the effect of the load on D versus NI was recalculated for a wider range and rounded values of N_L^2/R_L. These curves are shown in Fig. 39. Note how the minimum point of D becomes more pronounced as N_L^2/R_L increases.

(6) The assumption of $\delta \to 1$ was examined in the analysis, Sec. I-D-4-d; it corresponds to the assumption that in each leg, $\rho = \rho_p =$ constant. Accounting for variation in leg parameters with NI, D_{NL} versus NI for $\delta \to 1$ was computed from Eq. (80). The resulting plot is compared in Fig. 40 with computed D_{NL} versus NI, assuming that $\delta = 0.05263$, *i.e.*, $\phi_r/\phi_s = 0.9$.

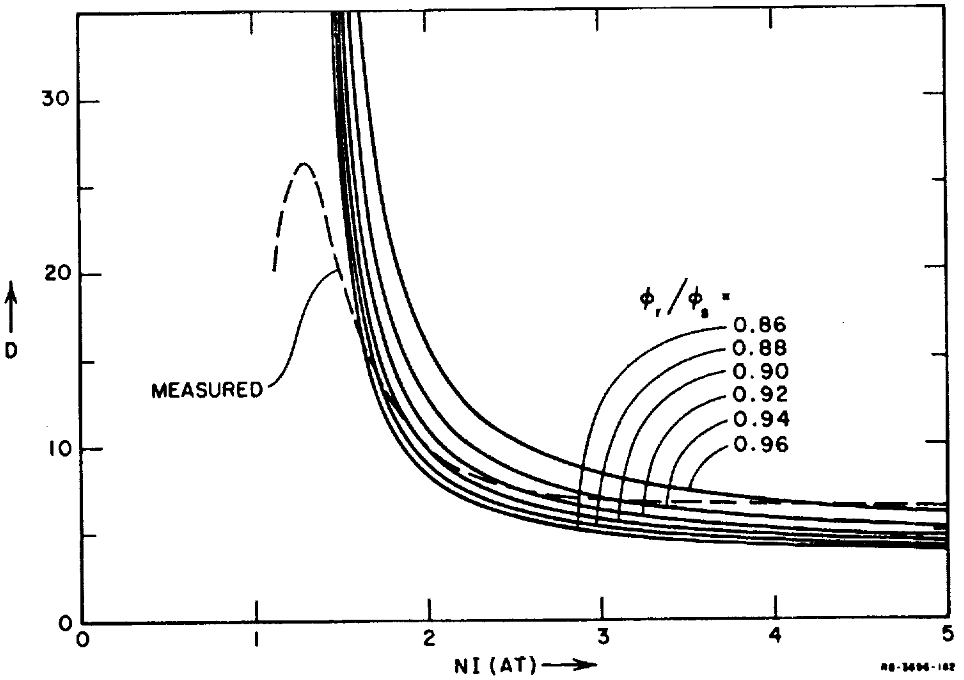

FIG. 37 EFFECT OF (ϕ_r/ϕ_s) ON CALCULATED D vs. NI IN THE NO-LOAD CASE

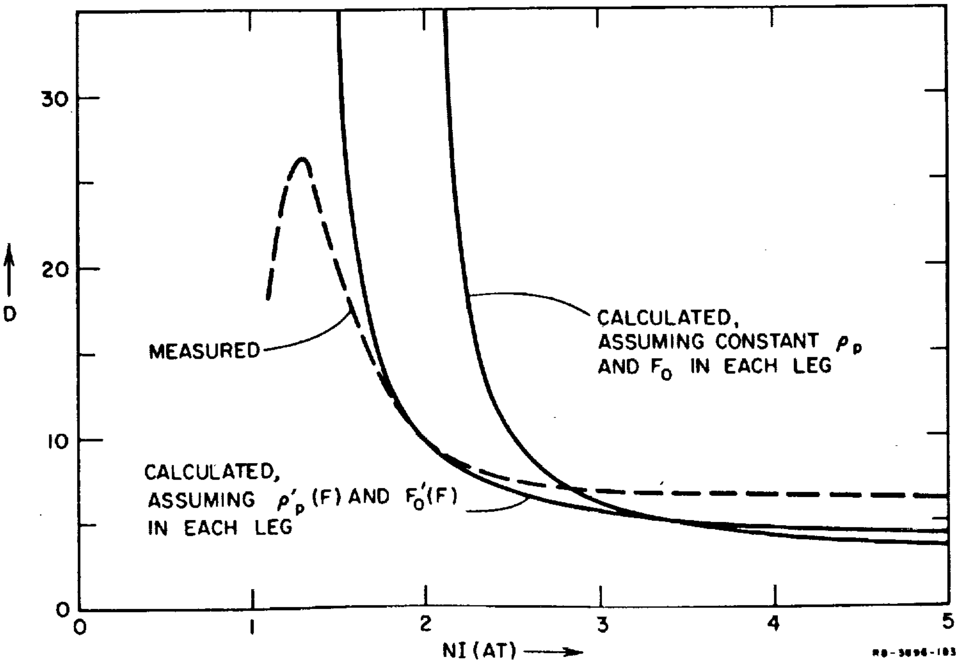

FIG. 38 D vs. NI IN THE NO-LOAD CASE

$\phi_r/\phi_s = 0.9$

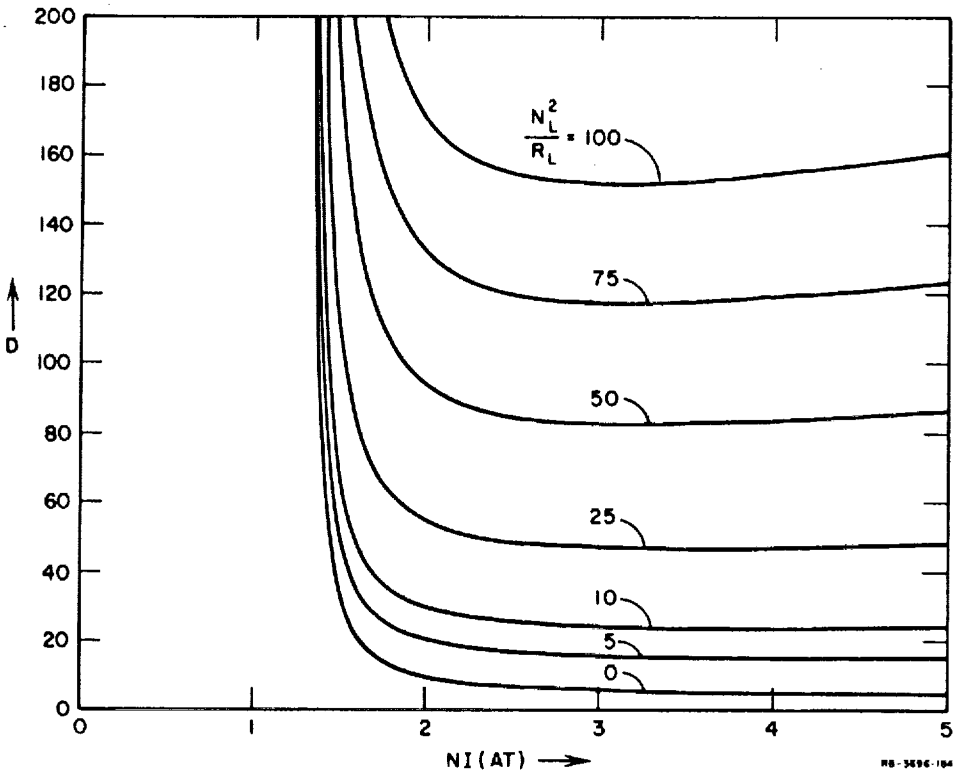

FIG. 39 CALCULATED D vs. NI WITH LOAD AS A PARAMETER $\phi_r/\phi_s = 0.9$

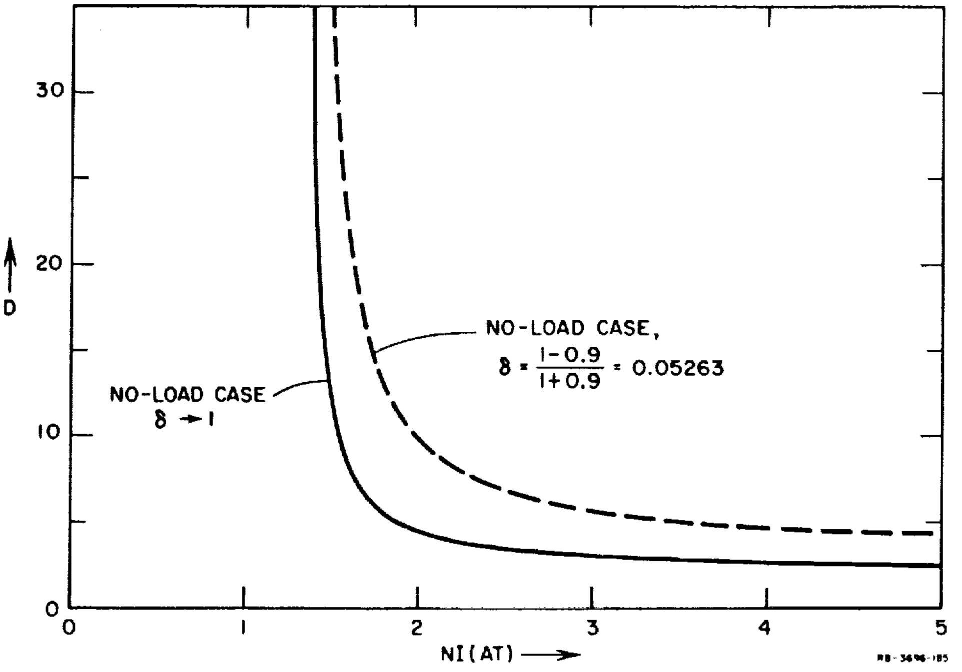

FIG. 40 CALCULATED D_{NL} vs. NI FOR $\delta \rightarrow 1$

(7) The effect of l_4/l_3 on the asymptotic value of D as $NI \to \infty$ is shown in Fig. 41 for various values of $\rho_{4p}/(R_L/N_L^2)$. Assuming that $(\phi_r/\phi_s) = 0.9$, these plots were calculated from Eqs. (111), (112), (72), and (73). At a first glance, these plots look suprisingly linear, whereas in fact they are nonlinear. In order to understand why these plots appear linear, let us first examine the no-load case. By differentiating the expression for $D_{NL,NI\to\infty}$ [Eq. (113)] with respect to l_4/l_3, the slope s of $D_{NL,NI\to\infty}$ versus l_4/l_3 is found to be

$$s = \frac{dD_{NL,NI\to\infty}}{d(l_4/l_3)} = 2(-ln\ \delta)\frac{1-\delta^2}{\delta}\left(\frac{y}{\delta^{-y}-\delta^{y}}\right)^2 , \qquad (123)$$

where

$$y = \frac{1}{1+\frac{l_4}{l_3}} . \qquad (123a)$$

Expressing δ^{-y} and δ^{y} in Eq. (123) by infinite series, we obtain

$$s = -ln\,\delta\,\frac{1-\delta^2}{2\delta}\left[\frac{y}{y\ ln\,\delta + \frac{(y\ ln\,\delta)^3}{3!} + \frac{(y\ ln\,\delta)^5}{5!} + \cdots}\right]^2 . \qquad (124)$$

For $l_4/l_3 >> 1$, $|y\ ln\ \delta| << 1$, hence s, Eq. (124), may be approximated by

$$s \simeq \frac{1-\delta^2}{2\delta(-ln\ \delta)} . \qquad (125)$$

Since $\delta^2 << 1$, Eq. (125) may be simplified further to the following:

$$s \simeq \frac{1}{2\delta(-ln\ \delta)} . \qquad (126)$$

It is evident from Eq. (125) or Eq. (126) why $D_{NL,NI\to\infty}$ versus l_4/l_3 may well be approximated by a straight line

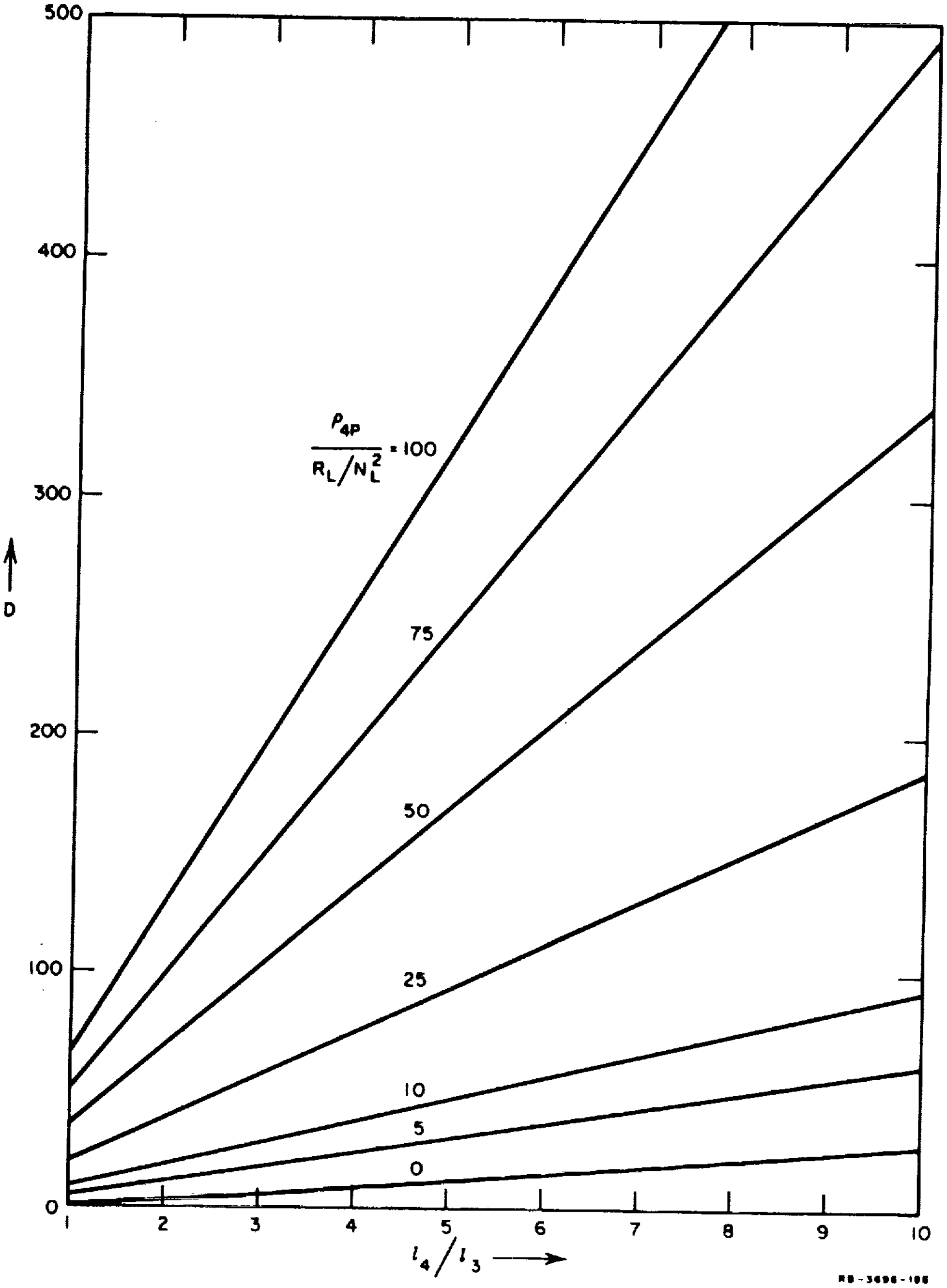

FIG. 41 CALCULATED $D_{N1\to\infty}$ vs. (l_4/l_3) FOR VARIOUS $(\rho_{4p}N_L^2/R_L)$ VALUES $\phi_r/\phi_s = 0.9$

of a slope s which depends only on δ. In Fig. 41, $\delta = [1 - (\phi_r/\phi_s)]/[1 + (\phi_r/\phi_s)] = (1 - 0.9)/(1 + 0.9) = 0.05263$. Thus, for $(l_4/l_3) >> 1$ in the no-load case, Eq. (126) yields $s \cong 3.22$, which agrees well with the corresponding plot in Fig. 41. For the cases where Leg 4 is loaded, the plot appears even more linear. The mathematical interpretation is complicated by the transcendental equation for $p_{NI \to \infty}$, Eq. (111). However, it was shown[8] that loading Leg 4 has essentially the same effect on D as increasing l_4/l_3 of an unloaded core. Hence, the expression in Eq. (126) is even a better approximation for s than in the no-load case, and the plots are more linear.

4. SUMMARY

Flux division in a nonsaturable core was measured (Figs. 29 and 30), and oscillograms of $\dot{\phi}$ waveforms (Figs. 31 and 32) were studied. These data are compared with previous treatments of this subject.[6,7,1] Flux division in a saturable core was measured (Fig. 33) and compared with calculated plots (Fig. 36) for four load values. Plots of D versus NI are also calculated, assuming switching parameters obtained from a nonlinear $\dot{\phi}_p$ versus F curve (Fig. 35), under the following conditions: no load with various ϕ_r/ϕ_s values (Fig. 37); various load values (Fig. 39); and $\delta \to 1$ in the no-load case (Fig. 40). Also, assuming constant switching parameters, D versus NI in the no-load case (Fig. 38), and D versus l_4/l_3 for $NI \to \infty$ (Fig. 41) were calculated.

E. UNSETTING EFFECT

1. INTRODUCTION

The unsetting effect was described in Report 1 (pp. 96-99). This effect is a special case of a more general phenomenon, according to which elastic $\Delta\phi$, $\Delta\phi_\epsilon$, in a leg driven far into saturation will cause an appreciable inelastic $\Delta\phi$ in (at least) two other legs. This phenomenon stems from the availability of two inelastic-switching paths, one for the rise and the other for the fall of $\Delta\phi_\epsilon$ in the leg in saturation. Upon termination of the drive pulse, the legs of the core were shown (*cf*. Fig. 93, Report 1, p. 97) to be left in a "stressed" state, *i.e.*, a residual H field, sustained by magnetic poles near the leg junctions, remains in each leg. Due to variations in air-flux linkage, a tight winding on the driven leg minimizes the unsetting effect. Our objective now is to verify experimentally the variations in ϕ and F predicted under two conditions (Fig. 93, Report 1, p. 97): a positive drive on Leg 3, and a negative drive on Leg 4.

2. EXPERIMENTS

A commercial core, AMP Core No. 395813-1, was chosen for the experiment. The core dimensions are shown in Fig. 42. Three small apertures were ignored, and a fourth one was identified with the small aperture in Fig. 92, Report 1, p. 97. From the core dimensions in Fig. 42, the average leg lengths are found to be as follows: $l_m^{av} = 14.8$ mm; $l_3^{av} = 1.1$ mm; $l_4^{av} = 2.45$ mm. The core parameters are as follows:
$H_c = 39.0\ AT/m (=0.49\ oe)$; $S_w = 63.7\ (AT/m)\mu\text{sec} (=0.8\ oe\ \mu\text{sec})$;
$2\phi_{r3} = 2\phi_{r4} = \phi_{rm} = 21$ maxwells; and $F_0 = 0.72\ AT$ (around the major aperture).

Experimental verification of the unsetting effect was performed in two separate experiments. The drive windings in both experiments were wound *tightly* as shown in Fig. 92 of Report 1 (p. 97) (instead of separate N_s and N_H windings, a single winding with N_s turns was wound on Leg 3). In addition, a two-turn sense winding was wound on each leg.

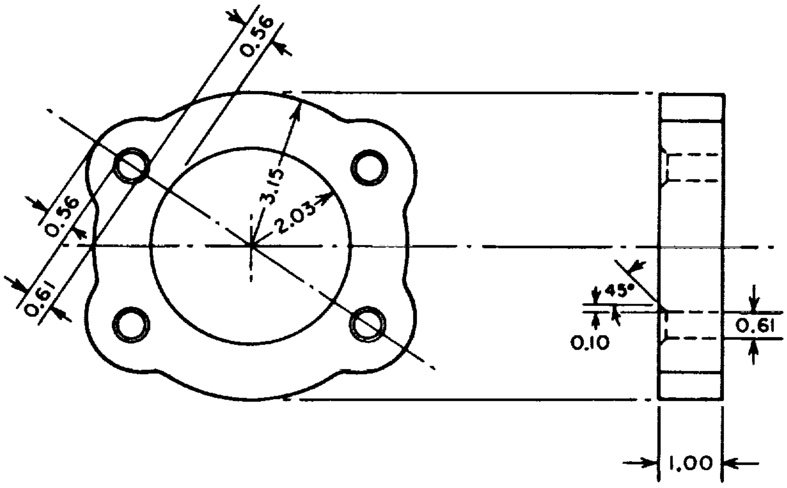

FIG. 42 DIMENSIONS OF THE CORE USED FOR THE UNSETTING EXPERIMENT
AMP Incorporated, Core No. 395813-1;
Dimensions in mm;
Tolerance ≅ ±0.025mm

The conditions for the two experiments were similar, except for the SET state. In the first experiment, the SET MMF was relatively small, so that the unsetting of Legs m and 3 was caused by pure elastic flux switching in Leg 4. In the second experiment, the SET MMF was high enough to cause some inelastic setting (supersetting effect) in Leg 4, as indicated by Point E in Fig. 93 of Report 1 (p. 97). The results of the first experiment are in the form of oscillograms and the results of the second experiment are in the form of plots.

In the first experiment, the number of turns of the drive windings (Fig. 92 of Report 1, p. 97) were: $N_C = 7$, $N_s = 1$, and $N = 10$. The drive currents were 2 μsec long, and their amplitudes were: $I_C = 3A$, $I_s = 3A$, and $I = 12A$ and $20A$. Oscillograms of the drive currents and the resulting changes in ϕ during the CLEAR, SET, and UNSET phases are shown in Fig. 43, for the two values of unsetting MMFs, $NI = 120\ AT$, and $NI = 200\ AT$. These oscillograms are in agreement with Fig. 93 of Report 1 (p. 97).

In the second experiment, the number of turns were $N_C = 7$, $N_s = 2$, and $N = 14$. The drive currents were 2 μsec long; the CLEAR and SET currents were kept constant ($N_C I_C = 25\ AT$ and $N_s I_s = 6\ AT$), and Current I was varied. For each value of NI, $\dot{\phi}$ was integrated and $\Delta\phi$, relative to the CLEAR state, was measured at three different times (see Fig. 93, Report 1, p. 97): after I_s is removed (Point E), during the application of I (Point G), and after I is removed (Point J). The flux measurement was made by means of the flux-reference (*cf*. Appendix F). The resulting curves are shown in Fig. 44. These results will now be discussed.

3. DISCUSSION

Let us now compare the experimental results in Fig. 44 with the variations in ϕ and F of each leg, which were predicted in Fig. 93, Report 1, p. 97. In general, Fig. 44 agrees with the predicted variations of ϕ in each leg. There are, however a few points that should be discussed. In order to facilitate this discussion, let us establish the following nomenclature: Let P and Q stand for any point in Fig. 93, Report 1, p. 97. Then, $\Delta\phi_{jP}$ represents the flux change of Leg j ($j = m$, 3, 4) from the CLEAR state (Point A, $\phi = -\phi_{rj}$) to Point P; ϕ_{jP} represents the flux level of Leg j at Point P; and $\Delta\phi_{j(P-Q)}$ represents the flux change of Leg j from Point P to Point Q.

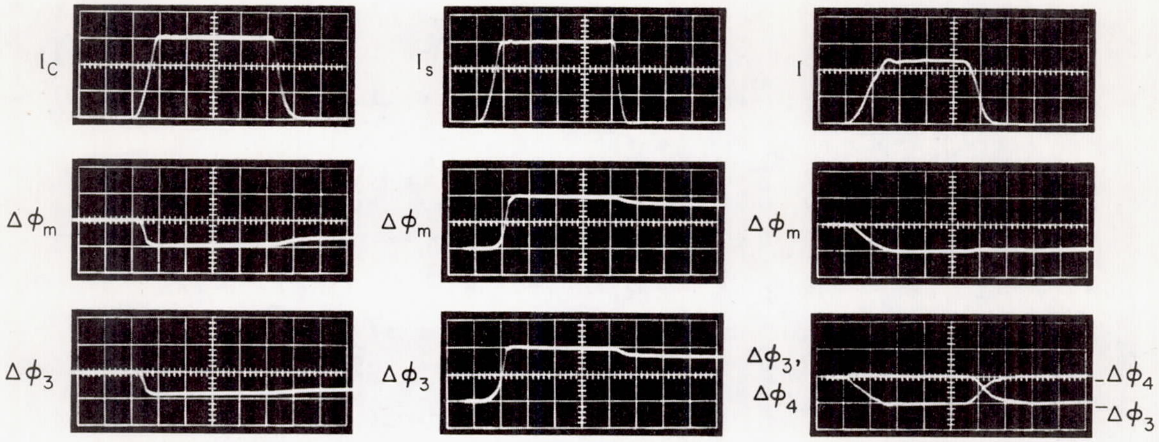

i CLEAR ii SET iii UNSET

(a) NI = 120 amp TURNS

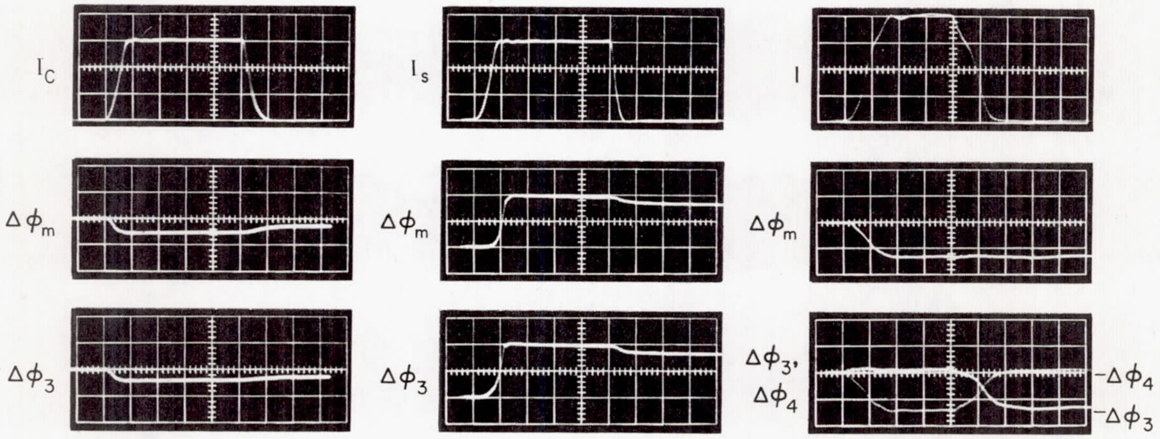

i CLEAR ii SET iii UNSET

(b) NI = 200 amp TURNS

RP-3696-200

FIG. 43 OSCILLOGRAMS OF DRIVE CURRENT AND FLUX CHANGE vs. TIME FOR THE UNSETTING EXPERIMENT
Time Scale = 0.5 μsec/major div.; Scale for I_C and I_s = 1 A/major div.; Scale for I = 5 A/major div.

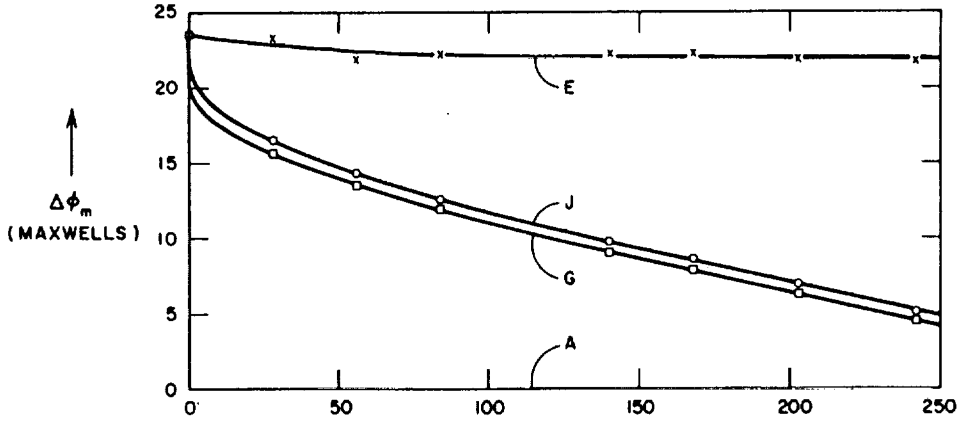

(a) LEG m

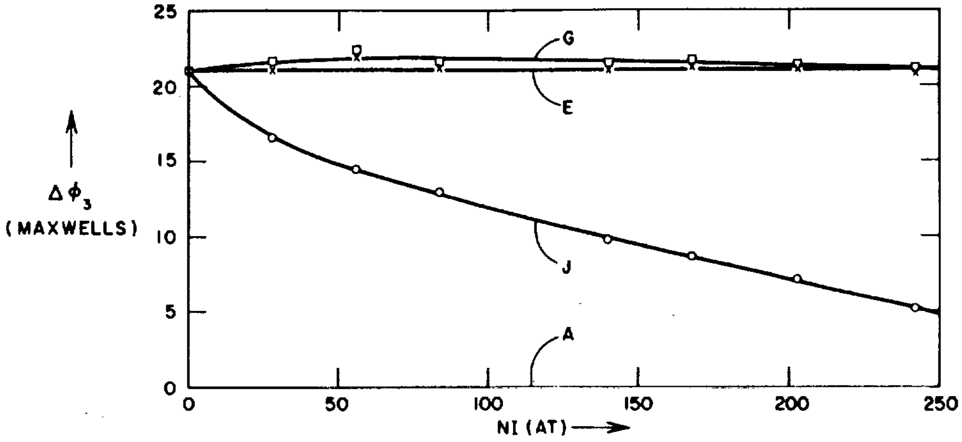

(b) LEG 3

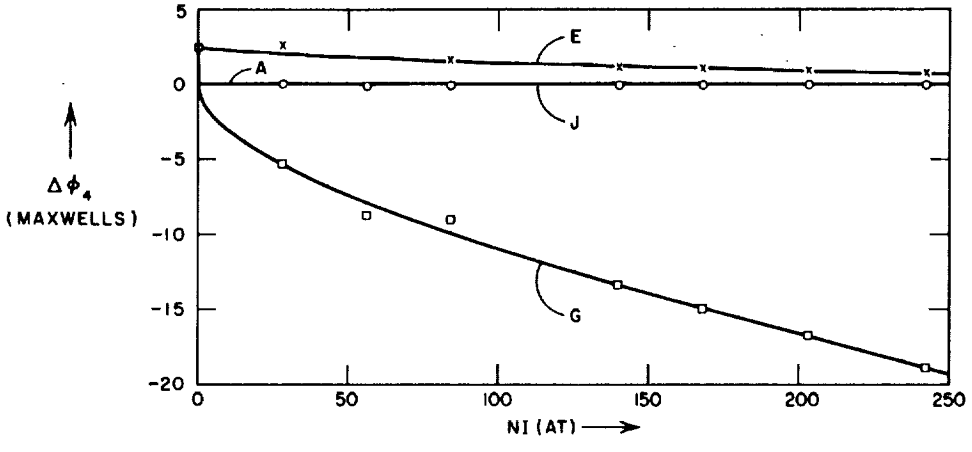

(c) LEG 4

RC-3696-196

FIG. 44 EXPERIMENTAL UNSETTING EFFECT

After the CLEAR MMF is removed, the core is set via Leg 3. Due to the supersetting effect (*cf*. Report 1, pp. 93-94), $\Delta\phi_{mE} > 2\phi_{r3}$ (= 21 maxwells), $\Delta\phi_{3E} \cong 2\phi_{r3}$, and $\Delta\phi_{4E} > 0$. The experimental $\Delta\phi_E$ of the three legs agree with what had been anticipated except for the following: Since N_sI_s was maintained constant (6 *AT*), $\Delta\phi_E$ of each leg was expected to be independent of *NI*. Instead, $\Delta\phi_{mE}$ and $\Delta\phi_{4E}$ have a slight droop as *NI* increases. This droop could not be explained until we found that the current pulser that had been used in this experiment had a low dc leakage current. This current increased from 1 to 15 ma as we increased the number of pulser channels that were connected in parallel. Instead of recording new data with the dc MMF cancelled, we decided to use the data because the effect was small, and because the main purpose of the experiment was to measure $\Delta\phi_{mJ}$ and $\Delta\phi_{4J}$, which, as will be shown later, are not influenced by the dc MMF. Furthermore, we shall interpret the data in considerable detail because of the interesting phenomena associated with the dc leakage currents in the experiments.

The resulting dc MMF (*i.e.*, *N* times the dc leakage current) of up to 0.21 ampere turns caused Points *A* [Fig. 97(b), Report 1, p. 97] to be biased away from the CLEAR state. This dc bias pushed Point *A* of Leg 4 down and Point *A* of Leg 3 up (in order to balance the elastic drop in ϕ_4), resulting in ϕ_3 being clamped to the static loop above $-\phi_{r3}$. (The effect on ϕ_m was negligible due to the relative length of Leg *m*.) The abscissa of Leg *j* ($j = m$, 3, 4) in Fig. 44 corresponds to the biased Point *A*, not to $\phi = -\phi_{rj}$. SET MMF pulse, N_sI_s, is applied next. Because of the higher initial ϕ_{3A}, the resulting $\Delta\phi_{3(A-C)}$ is smaller than the corresponding flux change without the dc MMF. This causes $\Delta\phi_{m(A-C)}$, and hence $\Delta\phi_{m(A-E)}$, to be smaller as well. Due to the dc MMF, ϕ_3 relaxes to Point *E* slightly higher than without the dc MMF (causing ϕ_{4E} to be lower). There are, therefore, two opposing effects of the dc MMF on $\Delta\phi_{3(A-E)}$. No net effect could be detected experimentally. This is evident from Fig. 44(b), where $\Delta\phi_{3(A-E)}$ is constant in *NI* (*NI* varies with the dc leakage current). An additional drop in ϕ_{mE} and ϕ_{4E} was caused during the interval between the I_s and *I* pulses by the combined dc MMF of the leakage current in the $N(=14)$ turns on Leg 4 and the $N_C(=7)$ turns on Leg *m*. This combined dc MMF of up to 0.315 *AT* acted against a soft threshold around the major aperture. Given sufficient time (as was the case in the experiment), some of the inelastic flux that had been set into Leg 4 due to the supersetting effect was switched back via Leg *m*.

Compared with the case of no dc MMF, ϕ_{4E} is lower, thus $|\Delta\phi_{4(E-G)}|$ is smaller because of a smaller inelastic switching. This results in less unsetting of Leg *m*, *i.e.*, $|\Delta\phi_{m(E-J)}|$ becomes smaller. It was found experimentally that $\Delta\phi_{m(J-A)}$ was independent of the dc MMF. This may be explained by the fact that the dc MMF decreases both $\Delta\phi_{m(A-E)}$ and $|\Delta\phi_{m(E-J)}|$. During the fall time, as Current *I* drops to the dc leakage level, ϕ_4 rises from Point *G* to Point *J*, which is slightly lower than in Fig. 93(c) (Report 1, p. 97); hence, ϕ_{3J} is slightly higher.

We therefore conclude that Point *J* of each leg is hardly affected by the dc leakage in the pulser. Based on this conclusion, the curves in Fig. 44 were plotted as follows. For each leg, $\Delta\phi_J$ (resulting from the CLEAR pulse) was plotted first; $\Delta\phi_{(E-J)}$ was then used to plot $\Delta\phi_E$, and $\Delta\phi_{(E-G)}$ was used to plot $\Delta\phi_G$.

The plots of $\Delta\phi_{mJ}$ and $\Delta\phi_{3J}$, Figs. 44(a) and (b), show the magnitude of the unsetting effect. For example, Leg 3 in a SET state can be demagnetized (*i.e.*, ϕ_3 dropped from $+\phi_{r3}$ to zero) by driving Leg 4 by $NI = 128$ *AT* (which is about 178 times F_0 around the major aperture). For $NI = 242$ *AT* ($=336\ F_0$), $\Delta\phi_{3J} = 5.2$ maxwells, thus 75% of $2\phi_{r3}$ was unset.

4. FALL-TIME EFFECT

The effect of winding position on the unset flux was discussed in Report 1 (p. 99). It was shown there that the tighter the drive winding is, the smaller is the amount of unset flux.

The amount of unset flux is also influenced by the fall time of the drive current. This stems from the fact that Leg 3 is unset inelastically, and inelastic switching requires a longer time than elastic switching. If the fall time is too short, the (fast) elastic switching in Leg 4, being unable to close fully through Leg 3, would close partially through the surrounding air. This would result in a creation of pole distribution near the leg junctions. The polarity of the poles is similar to the one in Fig. 87(c) of Report 1 (p. 92). These poles act on Leg *m* in the positive direction, and on Legs 3 and 4 in the negative direction. As a result, the excess *H* in Leg 3 would increase, enabling Leg 3 to switch faster. However, if the (soft) threshold in Leg *m* is exceeded, a portion of the elastic $\Delta\phi_4$ is steered into Leg *m* in the positive direction, and the pole density would decrease. The net result is a decrease in the unset flux in both Leg *m* and Leg 3. In conclusion, the unsetting effect is expected to be smaller as the fall time becomes shorter (below some threshold value). This conclusion has not yet been verified experimentally.

5. SUMMARY

The unsetting effect, which has been described in Report 1, is verified experimentally (Fig. 43). After the tested core is cleared, Leg 3 is set by a fixed SET MMF, and this is followed by applying a variable negative NI to Leg 4. After the removal of a relatively high NI, the core is left in a state commonly obtained by a relatively low NI through the major aperture. Additional effects due to leakage dc current in the driver pulser cause the set flux in Legs m and 4 to be slightly lower than without the leakage current. These effects are explained and taken into account in plotting the experimental data in Fig. 44.

Since the unsetting of Leg 3 during the fall of the drive current I involves inelastic switching, the duration of the fall of I influences the amount of the unset flux. The shorter the fall time is, the smaller is the unsetting effect.

F. CONCLUSIONS

In discussing and evaluating the results of much of Sec. II, it has been assumed that the magnetic properties of a core, or a leg of a core, are determined by integrating the corresponding material properties over the x coordinate (*cf*. Report 1, Fig. 19, p. 18) of the leg. This assumption is invalid if the material properties at one x value in the leg are affected by the process of switching or the magnetic state at other x values in the leg. For example, if the material of a toroidal core has a large magnetostriction constant, then a partially switched annular region of the core (where $|B| < B_r$), which is not free to change its dimensions, may produce a stress that can change the material properties in other regions of the core. However, we have no experimental evidence to support such an effect, and further investigation is needed.

The $\phi(F)$ testing of blank ferrite disks before the ultrasonic cutting of cores is an easy means of detecting disks having relatively abrupt radial variations in material $B(H)$ property, and of making comparisons between disks. Even though $\phi(F)$ testing cannot guarantee that a disk is entirely free of material variations, it is valuable for detecting appreciable nonuniformity.

Two possible modifications of the parabolic switching model were examined numerically in Sec. II-A-3. One accounted for $\rho_p(F)$ variations and the other for $F_0(\phi)$ variations. Analytical functions have not been given for $\rho_p(F)$ and $F_0(\phi)$; this remains to be done in the future. Modification of the parabolic model is needed primarily in the slow-switching range. On the basis of $\dot{\phi}(\phi)$ curves for a thin ring of *OD/ID* = 1.06, the result of performing these two modifications numerically was examined. It is concluded that some discrepancies still exist, but that very significant improvements do result. In some cases it may be desirable, for simplicity, to include only the $\rho_p(F)$ modification. This results in the same modification used in Sec. I-D-5, except for the terminology, *i.e.*, ρ_p' and F_0' are functions of F.

The discussion of flux switching in a core having a re-entrant shape makes use of the concept of a *switching line*. This concept is also useful in discussing switching in other types of non-toroidal cores. Single-aperture cores with re-entrant shapes can be divided into two classes. In cores of the first class, the shortest closed line that can be drawn inside the core and around the aperture does not touch the outer edge of the core. In cores of the second class, this shortest closed line touches the outer edge of the core. The discussion on slow flux switching in the first class (*cf*. Part B-3) is not detailed; it only presents the general configuration of the switching lines. The discussion of the second class includes a proposed model, which is called the switching crossover zone. This model, although self consistent, is intended only as an example of the kind of switching that may occur. The validity of the concepts presented in discussing re-entrant shaped cores rests upon two assumptions:

(1) that zone boundaries actually exist and have approximately the properties described in Report 1, pp. 119-128, and

(2) that the static $B(H)$ loop of the ferrite material has vertical sides. It is hoped that the basic concept of the crossover zone model will be useful in studying re-entrant shaped cores made of ferrite having more realistic static $B(H)$ properties.

The section on design considerations was specifically concerned with the design of two cores to be used for experimental studies of flux switching in multipath cores. The basic goal was to design two cores that would exhibit as few superfluous phenomena as possible. These considerations may not be applicable to the design of cores for optimum performance in a practical circuit. The final designs are not necessarily the best that could be achieved. For example, in determining l_i, l_o and l^{av} of each leg of Core *N* after the core was cut, the problem of the re-entrant core shape was first realized. Thus, the design of Core *N* could be improved by making Leg 2 straight instead of slightly curved.

The hyperbolic $B(H)$ model, which was used to obtain the static $\phi(F)$ equations in terms of core dimensions and material parameters, is experimentally checked for a core made of Telemeter Magnetic T-5 material [*cf.* Fig. 28(c)]. The disagreement in ϕ for $-5H_{th}l_o < F < +5H_{th}l_o$ is reasonably small, when compared to ϕ_r. However, the disagreement in ϕ from $-\phi_r$ up to ϕ corresponding to $F = H_{th}l_o$ is about 50% of the measured $\Delta\phi$ [*cf.* Fig. 28(d)]. This means that the hyperbolic $B_e(H)$ function, which fits the purely elastic switching region $-\infty < H < 0$, does not describe $B(H)$ properly in the region $0 < H < H_{th}$. It is evident that this region is characterized not only by elastic switching (as assumed by the model), but also by inelastic switching (of the same order of magnitude as the elastic switching). If it becomes important to describe $B(H)$ accurately in the region $0 < H < H_{th}$, then an additional function will have to be introduced. Evaluation of the hyperbolic $B(H)$ model in describing the static $B(H)$ properties of other materials has not been made.

The analysis of flux division was based on two factors: variation of ρ with ϕ, and the nonlinearity of ρ and F_0 at low values of F in each leg. From the comparison between calculated and measured D versus NI, it seems that these two factors are major contributors to the phenomenon of flux division. However, there are other factors (not accounted for in our analysis) that introduce errors to the calculated plots, especially when slow switching is involved in Leg 4 or all legs. These factors are:

(1) A small amount of inelastic flux change at a field lower than the threshold value,

(2) The limitations of the parabolic model of ρ in describing $\dot{\phi}$ at low F, even if the nonlinearity of $\dot{B}_p$ versus H is accounted for, and

(3) Elastic flux change during the rise time of NI may differ from the elastic flux change during the fall time of NI.

Inclusion of these factors in the analysis is bound to yield better results, but this involves establishment of additional switching models. Rather than improving the analysis of flux division in a saturable core, we feel that our next step should be to establish switching models for a soft state, so that we can analyze flux division in a nonsaturable core.

Experimental verification was given which clearly substantiated the existence of the unsetting effect and gave the magnitude of the effect for a particular core. Calculations of this magnitude, based on geometry and material properties, remains to be done.

APPENDIX A

CALCULATION OF STATIC $\phi(F)$ CURVE

APPENDIX A

CALCULATION OF STATIC $\phi(F)$ CURVE

The objective is to calculate a static $\phi(F)$ curve of a constant-width leg; the calculation is based on the suggested hyperbolic models for $B(H)$ [Eqs. (10) and (11)] in saturation and between saturation levels. This calculation is done by substituting Eqs. (2) and (3) into Eqs. (10) and (11) in order to derive $B(F,x)$, which will then be integrated from $x = 0$ to $x = w$ [Eq. (7)].

For $H \le H_{th}$, B is equal to

$$B_e = -B_r - (B_{ss} - B_r)\frac{F}{F - H_a(l_i + \alpha x)} + \frac{\mu_0 F}{l_i + \alpha x} \quad . \qquad \text{(A-1)}$$

For $H \ge H_{th}$, B is equal to

$$B_u = -B_r + (B_{ss} + B_r)\frac{F - H_q(l_i + \alpha x)}{F - H_n(l_i + \alpha x)} + \frac{\mu_0 F}{l_i + \alpha x} \quad . \qquad \text{(A-2)}$$

In deriving the expressions for $\phi(F)$, three regions of F are distinguished: $F \le l_i H_{th}$, $l_i H_{th} \le F \le l_o H_{th}$, and $l_o H_{th} \le F$.

1. $\underline{F \le l_i H_{th}}$

For this region of F, $H < H_{th}$ throughout the leg cross section, and only Eq. (A-1) is valid. By substituting Eq. (A-1) into Eq. (7) and integrating from $x = 0$ to $x = w$, we obtain the following expression:

$$\phi = \frac{Fh}{\alpha}\left[\frac{B_{ss} - B_r}{H_a}\ ln\left(\frac{F - H_a l_o}{F - H_a l_i}\right) + \mu_0\ ln\left(\frac{l_o}{l_i}\right)\right] - B_r hw \quad . \qquad \text{(A-3)}$$

2. $l_i H_{th} \leq F \leq l_o H_{th}$

The leg cross section is divided into two sections: In the inner section, $H > H_{th}$, and in the outer section, $H < H_{th}$. Let x_t be the distance from the inner edge to the boundary between the two sections. At $x = x_t$, $H = H_{th}$, hence Eqs. (2) and (3) yield

$$x_t = \frac{1}{\alpha}\left(\frac{F}{H_{th}} - l_i\right) \quad . \tag{A-4}$$

In the section where $0 \leq x \leq x_t$, Eq. (A-2) is valid; in the section where $x_t \leq x \leq w$, Eq. (A-1) is valid. Therefore, Eq. (7) becomes

$$\phi = h[\int_0^{x_t} B_u(F,x)dx + \int_{x_t}^{w} B_e(F,x)dx] \quad . \tag{A-5}$$

After substituting Eqs. (A-1) and (A-2) into Eq. (A-5) and integrating, we get the following expression:

$$\phi = \frac{Fh}{\alpha}\left\{\frac{B_{ss} - B_r}{H_a}\, ln\left[\frac{F - H_a l_o}{F\left(1 - \frac{H_a}{H_{th}}\right)}\right] + \frac{(B_{ss} + B_r)(H_q - H_n)}{H_n^2}\, ln\left[\frac{F\left(1 - \frac{H_n}{H_{th}}\right)}{F - H_n l_i}\right]\right.$$

$$\left. + \frac{(B_{ss} + B_r)H_q}{H_n H_{th}} + \mu_0\, ln\left(\frac{l_o}{l_i}\right)\right\} - h\left[\frac{(B_{ss} + B_r)H_q}{H_n}\,\frac{l_i}{\alpha} + B_r w\right] \quad . \tag{A-6}$$

3. $l_o H_{th} \leq F$

Here $H > H_{th}$ throughout the leg cross section, and only Eq. (A-2) is valid. After Eq. (A-2) is substituted into Eq. (7), and integration is performed from $x = 0$ to $x = w$, the following expression is obtained:

$$\phi = \frac{Fh}{\alpha}\left[\frac{(B_{ss} + B_r)(H_q - H_n)}{H_n^2}\, ln\left(\frac{F - H_n l_o}{F - H_n l_i}\right) + \mu_0\, ln\left(\frac{l_o}{l_i}\right)\right] + hw\left[\frac{(B_{ss} + B_r)H_q}{H_n} - B_r\right] \quad . \tag{A-7}$$

APPENDIX B

RELUCTANCE OF A VARIABLE-WIDTH LEG OF LINEAR MATERIAL

APPENDIX B

RELUCTANCE OF A VARIABLE-WIDTH LEG OF LINEAR MATERIAL

Let a point in space be described by rectangular coordinates (x,y,z), and by orthogonal curvilinear coordinates (u_1,u_2,u_3). There is a functional relation between x, y, and z and u_1, u_2, and u_3. It can be shown[5] that an element of distance is expressed by

$$ds = \sqrt{\sum_{i=1}^{3} g_{ii}(du_i)^2} \quad , \tag{B-1}$$

where

$$g_{ii} = \left(\frac{\partial x}{\partial u_i}\right)^2 + \left(\frac{\partial y}{\partial u_i}\right)^2 + \left(\frac{\partial z}{\partial u_i}\right)^2 \quad . \tag{B-2}$$

Since we have assumed a leg to have a constant thickness h, our problem is two dimensional, and Eqs. (B-1) and (B-2) are reduced to

$$ds = \sqrt{g_{11}du_1^2 + g_{22}du_2^2} \quad , \tag{B-3}$$

where

$$g_{11} = \left(\frac{\partial x}{\partial u_1}\right)^2 + \left(\frac{\partial y}{\partial u_1}\right)^2 \quad , \tag{B-4}$$

and

$$g_{22} = \left(\frac{\partial x}{\partial u_2}\right)^2 + \left(\frac{\partial y}{\partial u_2}\right)^2 \quad . \tag{B-5}$$

Now consider a variable-width leg whose boundaries follow the directions of some orthogonal curvilinear coordinates u_1 and u_2. In Fig. B-1, the edges of such a leg are defined by $u_2 = u_{2a}$ and $u_2 = u_{2b}$, and the ends of the leg are defined by $u_1 = u_{1a}$ and $u_1 = u_{1b}$, where u_{2a}, u_{2b}, u_{1a}, and u_{1b} are all constants.

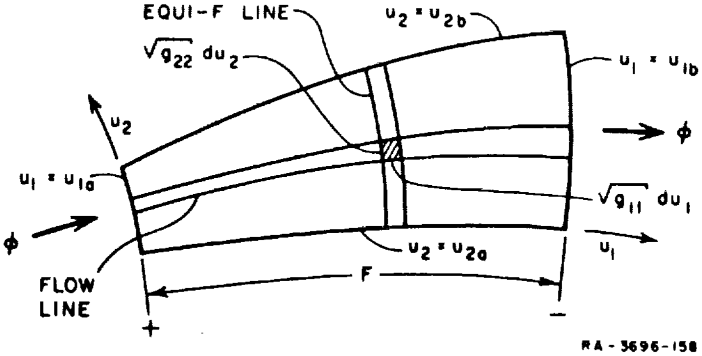

FIG. B-1 CURVILINEAR LEG

The leg is now divided into curvilinear squares of length $\sqrt{g_{11}}du_1$ and width $\sqrt{g_{22}}du_2$ that, together with thickness h, define leg elements. The length and width of each curvilinear square vary in such a way that the MMF drop along the leg element, $H\sqrt{g_{11}}du_1$, and the flux through it, $Bh\sqrt{g_{22}}du_2$, are identical for all the leg elements. By plotting these curvilinear squares, one gets the equi-F lines along the u_2 direction and the flow lines along the u_1 direction. The reluctance of every leg element defined by a curvilinear square is the same, and following Eqs. (26) and (27), is equal to

$$\Delta \mathfrak{R} = \frac{H\sqrt{g_{11}}du_1}{Bh\sqrt{g_{22}}du_2} = \frac{1}{\mu h}\,\frac{\sqrt{g_{11}}du_1}{\sqrt{g_{22}}du_2} \quad . \tag{B-6}$$

The reluctance of $\delta\mathfrak{R}$ of a larger leg element, defined by two adjacent equi-F lines, is the inverse of the integral of the inverse of $\Delta\mathfrak{R}$, *i.e.*,

$$\delta\mathfrak{R} = \frac{du_1}{\mu h \displaystyle\int_{u_{2a}}^{u_{2b}} \sqrt{\frac{g_{22}}{g_{11}}}\, du_2} \quad . \tag{B-7}$$

The reluctance of the whole leg is obtained by integrating $\delta\mathfrak{R}$ along the leg; hence,

$$R = \frac{1}{\mu h} \int_{u_{1a}}^{u_{1b}} \frac{du_1}{\int_{u_{2a}}^{u_{2b}} \sqrt{\frac{g_{22}}{g_{11}}}\, du_2} \quad . \tag{B-8}$$

Let us now apply Eq. (B-8) to three examples.

Example 1--A toroid of inner radius r_i and outer radius r_o.

Here, $u_1 \equiv \theta$ ($u_{1a} = 0$; $u_{1b} = 2\pi$); $u_2 \equiv r$ ($u_{2a} = r_i$; $u_{2b} = r_o$); $x = r \cos \theta$; and $y = r \sin \theta$. Following Eqs. (B-4) and (B-5), $g_{11} = r^2$ and $g_{22} = 1$. Thus,

$$R = \frac{1}{\mu h} \int_{0}^{2\pi} \frac{d\theta}{\int_{r_i}^{r_o} \sqrt{\frac{1}{r^2}}\, dr} \quad ,$$

or

$$R = \frac{1}{\mu h} \frac{2\pi}{ln\left(\frac{r_o}{r_i}\right)} \quad . \tag{B-9}$$

Example 2—A tapered leg (see Fig. 3) of length $r_b - r_a$ and angle β.

Here, $u_1 \equiv r$ ($u_{1a} = r_a$; $u_{1b} = r_b$); $u_2 \equiv \theta$ ($u_{2a} = 0$; $u_{2b} = \beta$); $x = r \cos \theta$; $y = r \sin \theta$; $g_{11} = 1$; $g_{22} = r^2$. Thus,

$$R = \frac{1}{\mu h} \int_{r_a}^{r_b} \frac{dr}{\int_{0}^{\beta} \sqrt{\frac{r^2}{1}}\, d\theta} \quad ,$$

or

$$\mathcal{R} = \frac{1}{\mu h} \frac{\ln\left(\frac{r_b}{r_a}\right)}{\beta} \quad . \tag{B-10}$$

Example 3—A transfluxor-like leg, Fig. B-2, defined by angle α and eccentric circles of radii r_a and r_b and eccentricity e. It can be shown[5] that the circles can be described by bicylindrical coordinates (η, θ) that are related to the rectangular coordinates according to

$$x = \frac{a \sinh \eta}{\cosh \eta - \cos \theta} \quad , \tag{B-11}$$

and

$$y = \frac{a \sin \theta}{\cosh \eta - \cos \theta} \quad , \tag{B-12}$$

where a is a scale factor which is related to r_a, r_b and e as follows:

$$a = \frac{1}{2e}\sqrt{e^4 - 2e^2(r_b^2 + r_a^2) + (r_b^2 - r_a^2)^2} \; . \tag{B-13}$$

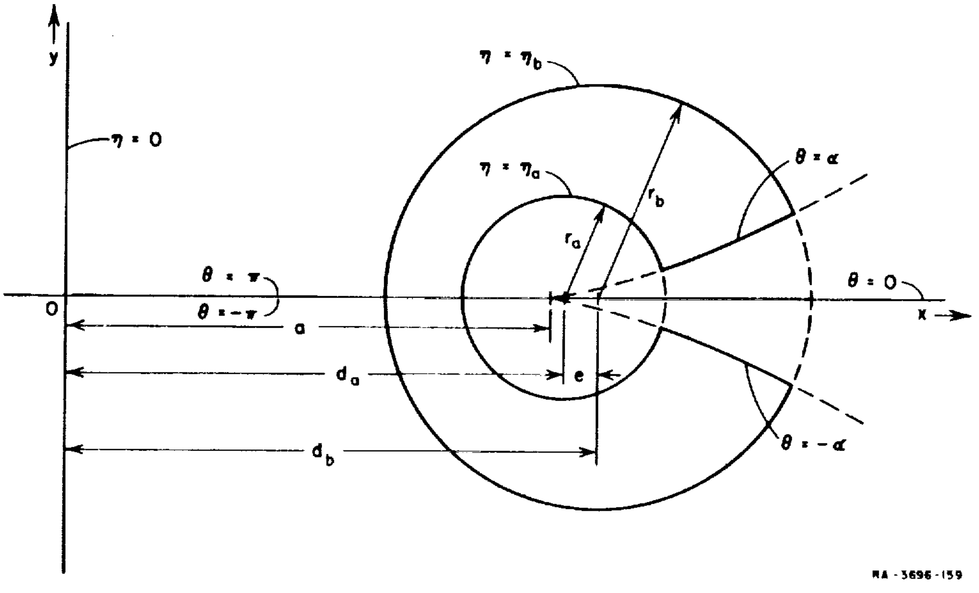

FIG. B-2 TRANSFLUXOR LEG

A flow line follows a circle of radius

$$r = \frac{a}{|\sinh \eta|} \tag{B-14}$$

with a center on the x axis at a distance

$$d = a \coth \eta \tag{B-15}$$

from the origin. By varying η from η_a to η_b $(\eta_a > \eta_b)$, the circles expand and move to the right, *i.e.*, the radii increase from r_a to r_b and the centers move from $x = d_a$ to $x = d_b$.

A constant-F line, perpendicular to the flow lines, follows a circle of radius

$$r' = \frac{a}{|\sin \theta|} \tag{B-16}$$

with center on the y axis at a distance

$$d' = a \cot \theta \tag{B-17}$$

from the origin. The leg ends are thus sections of circles defined by letting $\theta = \pm\alpha$ in Eqs. (B-16) and (B-17).

In order to calculate R, let us divide the leg into two symmetrical half legs, one above the x axis and one below it. The width of each half leg varies as θ varies from $\pm\pi$ to $\pm\alpha$. The total R is twice that of one of the half legs. For the top half leg, $u_1 \equiv \theta$ $(u_{1a} = \pi;\ u_{1b} = \alpha)$; $u_2 \equiv \eta$ $(u_{2a} = \eta_a;\ u_{2b} = \eta_b)$. Following Eqs. (B-4), (B-5), (B-11), and (B-12),

$$g_{11} = g_{22} = \left(\frac{a}{\cosh \eta - \cos \theta}\right)^2 \quad . \tag{B-18}$$

The total R is then

$$\mathsf{R} = 2 \cdot \frac{1}{\mu h} \int_{\pi}^{a} \frac{d\theta}{\int_{\eta_a}^{\eta_b} d\eta} \quad ,$$

or

$$\mathcal{R} = \frac{1}{\mu h} \frac{2(\pi - \alpha)}{\eta_a - \eta_b} . \qquad \text{(B-19)}$$

Substituting Eq. (B-14) into Eq. (B-19),

$$\mathcal{R} = \frac{1}{\mu h} \frac{2(\pi - \alpha)}{\sinh^{-1}\left(\frac{a}{r_a}\right) - \sinh^{-1}\left(\frac{a}{r_b}\right)} , \qquad \text{(B-20)}$$

where a is expressed in terms of r_a, r_b and eccentricity e in Eq. (B-13).

As a final note to the problem of finding $\mathcal{R}$ in general, suppose that the leg boundaries are not amenable to analytical expression. In a case like this, we shall have to resort to numerical or graphical approximations.[4,5] The smaller the curvilinear squares are, the more accurate is the approximation, but this makes the process more tedious. It is better to start with large curvilinear squares so as to have a feel for the general trend, and then reduce their size step by step.

Suppose we end up with $n_1 \times n_2$ curvilinear squares, each with the same length ratio $\Delta l_1/\Delta l_2$ (subscript 1 corresponds to the direction of flow lines along the leg; subscript 2 corresponds to the direction of equi-F lines across the leg). The total $\mathcal{R}$ is, then,

$$\mathcal{R} = \frac{1}{\mu h} \frac{\Delta l_1}{\Delta l_2} \frac{n_1}{n_2} . \qquad \text{(B-21)}$$

APPENDIX C

CALCULATION OF $\bar{\rho}_t$

APPENDIX C

CALCULATION OF $\bar{\rho}_t$

The expression for $\bar{\rho}(u_f)$ in general [Eq. (47)] is

$$\bar{\rho} = \frac{u_f - u_0}{\displaystyle\int_{u_0}^{u_f} \left(\frac{1}{\rho}\right) du} \quad . \tag{C-1}$$

The expression for ρ_t was shown to be [*cf*. Eq. (33)]

$$\rho_t = \frac{2\zeta_p h\beta}{ln\left(\dfrac{c^2 - u^2}{1 - u^2}\right)} \quad , \tag{C-2}$$

where $c = r_b/r_a$ and $u = \phi/\phi_s$. Substituting Eq. (C-2) into Eq. (C-1),

$$\bar{\rho}_t = 2\zeta_p h\beta \frac{u_f - u_0}{\displaystyle\int_{u_0}^{u_f} ln\left(\frac{c^2 - u^2}{1 - u^2}\right) du} \quad . \tag{C-3}$$

The integrand in the denominator of Eq. (C-3) can be written as

$$\begin{aligned} ln\left(\frac{c^2 - u^2}{1 - u^2}\right) = {} & ln\ (c + u) + ln\ (c - u) - ln\ (1 + u) \\ & - ln\ (1 - u) \quad . \end{aligned} \tag{C-4}$$

Hence,

$$\int ln\left(\frac{c^2 - u^2}{1 - u^2}\right) du = (c + u)\ ln\ (c + u) - (c - u)\ ln\ (c - u)$$
$$- (1 + u)\ ln\ (1 + u) + (1 - u)\ ln\ (1 - u) \quad , \tag{C-5}$$

or,

$$\int ln\left(\frac{c^2 - u^2}{1 - u^2}\right) du = ln\left[\frac{(c + u)^{c+u}(1 - u)^{1-u}}{(c - u)^{c-u}(1 + u)^{1+u}}\right] \quad . \tag{C-6}$$

After substituting the limits of integration u_0 and u_f into Eq. (C-6), Eq. (C-3) gives

$$\overline{\rho}_t = 2\zeta_p h\beta \frac{u_f - u_0}{ln\left[\frac{(c + u_f)^{c+u_f}(1 - u_f)^{1-u_f}(c - u_0)^{c-u_0}(1 + u_0)^{1+u_0}}{(c - u_f)^{c-u_f}(1 + u_f)^{1+u_f}(c + u_0)^{c+u_0}(1 - u_0)^{1-u_0}}\right]} \quad . \tag{C-7}$$

Substitution of $u_0 = -u_r$ into Eq. (C-7) results in Eq. (50).

APPENDIX D

CALCULATION OF FLUX-DIVISION PARAMETERS

APPENDIX D

CALCULATION OF FLUX-DIVISION PARAMETERS

The six basic equations for calculating flux-division ratio D are Eqs. (52) through (57). Two of these equations have already been employed in the text. Equation (52) was used in order to show that $\phi_{3f} = -\phi_{4f}$ [*cf.* Eq. (62)]. Equation (56) was used to derive Eqs. (65) and (66) which, when combined, become

$$\tanh^{-1}\left(\frac{\phi_{3f}}{\phi_s}\right) = \frac{\rho_{3p}}{\phi_s}\left(\int_0^T F_3 dt - F_{03}T\right) - \tanh^{-1}\left(\frac{\phi_r}{\phi_s}\right) \quad . \qquad \text{(D-1)}$$

Equation (D-1) includes two unknowns, T and $\int_0^T F_3 dt$; hence two more equations are needed. These two equations will be derived from four of the basic equations that have not been used yet: Eqs. (54) and (57) will lead to one equation, and Eqs. (53) and (55) will lead to the other.

For the sake of convenience, let us rewrite Eqs. (54), (57), (53), and (55) in this order.

$$F_4 = F_3 - \frac{N_L^2}{R_L}\dot{\phi}_4 \quad , \qquad \text{(D-2)}$$

$$\dot{\phi}_4 = \rho_{4p}\left[1 - \left(\frac{\phi_4}{\phi_s}\right)^2\right](F_4 - F_{04}) \quad , \qquad \text{(D-3)}$$

$$NI = F_m + F_3 \quad , \qquad \text{(D-4)}$$

and

$$\dot{\phi}_m = \rho_{mp}\left[1 - \left(\frac{\phi_m}{2\phi_s}\right)^2\right](F_m - F_{0m}) \quad . \qquad \text{(D-5)}$$

Substituting the expression for F_4 [Eq. (D-2)] into Eq. (D-3) results in

$$\dot{\phi}_4 = \frac{F_3 - F_{04}}{\dfrac{1}{\rho_{4p}[1 - (\phi_4/\phi_s)^2]} + \dfrac{N_L^2}{R_L}} \quad . \tag{D-6}$$

Hence

$$\int_{-\phi_r}^{\phi_{4f}} \left\{ \frac{1}{\rho_{4p}[1 - (\phi_4/\phi_s)^2]} + \frac{N_L^2}{R_L} \right\} d\phi = \int_0^T (F_3 - F_{04})dt \quad . \tag{D-7}$$

After integration and substitution of $\phi_{4f} = -\phi_{3f}$ [Eq. (62)], Eq. (D-7) yields

$$\frac{\phi_s}{\rho_{4p}} \left[\tanh^{-1}\left(\frac{\phi_r}{\phi_s}\right) - \tanh^{-1}\left(\frac{\phi_{3f}}{\phi_s}\right)\right] + \frac{N_L^2}{R_L}(\phi_r - \phi_{3f}) = \int_0^T F_3 dt - F_{04}T \quad . \tag{D-8}$$

Equation (D-8) is the second of the equations needed to solve for ϕ_{3f}/ϕ_s. The third equation will be derived as follows.

Following Eq. (D-4),

$$\int_0^T F_3 dt = NIT - \int_0^T F_m dt \quad . \tag{D-9}$$

Following Eq. (D-5),

$$\int_{-2\phi_r}^{0} \frac{d\phi_m}{1 - \left(\dfrac{\phi_m}{2\phi_s}\right)^2} = \rho_{mp}\left(\int_0^T F_m dt - F_{0m}T\right) \quad ; \tag{D-10}$$

hence,

$$\int_0^T F_m dt = F_{0m} T + \frac{2\phi_s}{\rho_{mp}} \tanh^{-1}\left(\frac{\phi_r}{\phi_s}\right) . \tag{D-11}$$

Substituting Eq. (D-11) into Eq. (D-9),

$$\int_0^T F_3 dt = (NI - F_{0m})T - \frac{2\phi_s}{\rho_{mp}} \tanh^{-1}\left(\frac{\phi_r}{\phi_s}\right) . \tag{D-12}$$

Equations (D-1), (D-8), and (D-12) will now be employed to solve for γ [which is equal to 2 $\tanh^{-1}$ (ϕ_{3f}/ϕ_s)]. Substituting the expression for $\tanh^{-1}$ (ϕ_{3f}/ϕ_s), Eq. (D-1), into Eq. (D-8), we get

$$\frac{2\phi_s}{\rho_{4p}} \tanh^{-1}\left(\frac{\phi_r}{\phi_s}\right) + \frac{N_L^2}{R_L} (\phi_r - \phi_{3f}) = \left(1 + \frac{\rho_{3p}}{\rho_{4p}}\right)\int_0^T F_3 dt - \left(F_{04} + F_{03}\frac{\rho_{3p}}{\rho_{4p}}\right) T . \tag{D-13}$$

Substitution of Eq. (D-12) into Eq. (D-13) yields an expression for T:

$$T = \frac{2\phi_s \tanh^{-1}\left(\frac{\phi_r}{\phi_s}\right)\left[\frac{1}{\rho_{4p}} + \frac{1}{\rho_{mp}}\left(1 + \frac{\rho_{3p}}{\rho_{4p}}\right)\right] + \frac{N_L^2}{R_L}(\phi_r - \phi_{3f})}{(NI - F_{0m})\left(1 + \frac{\rho_{3p}}{\rho_{4p}}\right) - F_{04} - F_{03}\frac{\rho_{3p}}{\rho_{4p}}} . \tag{D-14}$$

Subtracting $F_{03}T$ from both sides of Eq. (D-12), and substituting the resulting expression for $(\int_0^T F_3 dt - F_{03}T)$ into Eq. (D-1) results in

$$\tanh^{-1}\left(\frac{\phi_{3f}}{\phi_s}\right) = \frac{\rho_{3p}}{\phi_s}(NI - F_{0m} - F_{03})T - \left(1 + \frac{2\rho_{3p}}{\rho_{mp}}\right)\tanh^{-1}\left(\frac{\phi_r}{\phi_s}\right) . \tag{D-15}$$

Substitution of the expression for T [Eq. (D-14)] into Eq. (D-15) results in the expression

$$\frac{\gamma}{2} = \tanh^{-1}\left(\frac{\phi_{3f}}{\phi_s}\right) = \frac{a_1\left(\frac{\phi_r}{\phi_s} - \frac{\phi_{3f}}{\phi_s}\right) + a_2 \tanh^{-1}\left(\frac{\phi_r}{\phi_s}\right)}{a_3} , \quad \text{(D-16)}$$

in which a_1, a_2, and a_3 depend on core parameters and NI as follows:

$$a_1 = \frac{N_L^2 \rho_{4p}}{R_L} \rho_{3p} (NI - F_{0m} - F_{03}) , \quad \text{(D-17)}$$

$$a_2 = (NI - F_{0m})(\rho_{3p} - \rho_{4p}) + F_{04}\rho_{4p}\left(1 + 2\frac{\rho_{3p}}{\rho_{mp}}\right) - F_{03}\rho_{3p}\left(1 + 2\frac{\rho_{4p}}{\rho_{mp}}\right) , \quad \text{(D-18)}$$

and

$$a_3 = (NI - F_{0m})(\rho_{3p} + \rho_{4p}) - F_{04}\rho_{4p} - F_{03}\rho_{3p} . \quad \text{(D-19)}$$

Equation (D-16) is transcendental, and ϕ_{3f}/ϕ_s is solved for numerically after the coefficients a_1, a_2, and a_3 have been evaluated. Following Eq. (68),

$$\tanh^{-1}\left(\frac{\phi_r}{\phi_s}\right) = \frac{1}{2} \ln\left(\frac{1 + \frac{\phi_r}{\phi_s}}{1 - \frac{\phi_r}{\phi_s}}\right) = -\frac{1}{2} \ln \delta . \quad \text{(D-20)}$$

Substituting Eq. (D-20) into Eq. (D-16) and multiplying both sides by 2,

$$\gamma = \frac{2a_1\left(\frac{\phi_r}{\phi_s} - \frac{\phi_{3f}}{\phi_s}\right) - a_2 \ln \delta}{a_3} , \quad \text{(D-21)}$$

or,

$$\gamma = p - q \ln \delta , \quad \text{(D-22)}$$

in which

$$p = \frac{2a_1\left(\frac{\phi_r}{\phi_s} - \frac{\phi_{3f}}{\phi_s}\right)}{a_3} , \qquad (D\text{-}23)$$

and

$$q = \frac{a_2}{a_3} . \qquad (D\text{-}24)$$

After substituting the expressions for a_1, a_2, and a_3 [Eqs. (D-17) through (D-19)], Eqs. (D-22), (D-23), and (D-24) are identical with Eqs. (69), (70), and (71), respectively.

APPENDIX E

SECOND-ORDER INTEGRATOR

APPENDIX E

SECOND-ORDER INTEGRATOR

The measurement of flux changes or observation of $\phi(t)$ waveforms requires the use of an integrator. The commonly used *R-C* integrator has the problem of integrator droop. One way of overcoming this problem is to add a signal that is approximately equal and opposite to the error of the *R-C* integrator.[2,12] This error-correcting signal can be obtained by integrating the output of the *R-C* integrator with another *R-C* integrator, as shown in Fig. E-1. The wide-band preamplifier has a high input impedance (≈ 1 megohm) and a low output impedance (less than 100 ohms). The outputs Ke_1 and e_2 can be added algebraically in a dual-trace oscilloscope preamplifier. Assuming that Capacitors C_1 and C_2 are initially discharged, the following differential equations illustrate the principle of operation:

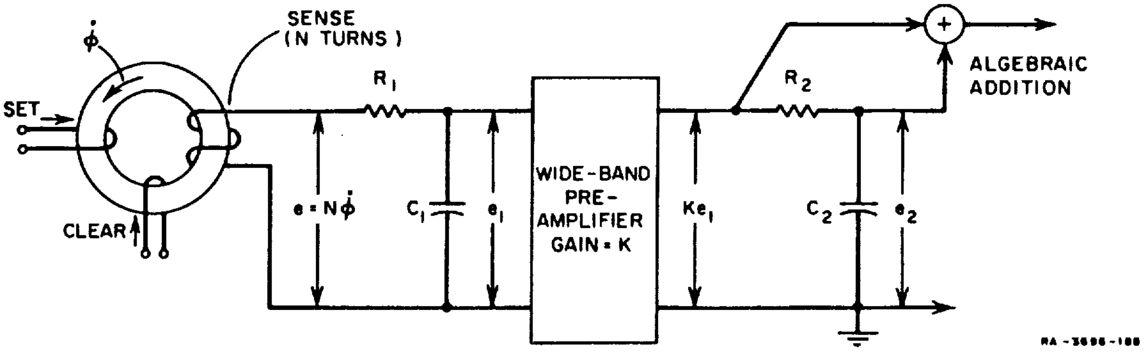

FIG. E-1 SECOND ORDER R-C INTEGRATION

$$Ke_1 = \frac{K}{R_1C_1}\int e\,dt - \frac{K}{R_1C_1}\int e_1 dt \quad , \tag{E-1}$$

and

$$e_2 = \frac{K}{R_2C_2}\int e_1 dt - \frac{1}{R_2C_2}\int e_2 dt \quad . \tag{E-2}$$

By making $R_1C_1 = R_2C_2$ and adding Eqs. (E-1) and (E-2), we obtain

$$Ke_1 + e_2 = \frac{K}{R_1C_1}\int edt - \frac{1}{R_1C_1}\int e_2dt \quad . \tag{E-3}$$

Note that the amplified error of the first integration, $-(K/R_1C_1)\int e_1dt$, has been cancelled by the output of second integration, except for a second-order error, $-\int(1/R_1C_1)e_2dt$. The main signal, which contains the first-order error, is Ke_1, and the error-correcting signal is e_2. A comparison of experimental integrals for a first-order and a second-order integrator is shown in Fig. E-2. The value of RC for this figure is 300 μsec.

Further correction can be obtained by adding more stages, providing a means is available for adding three or more signals that have a common ground.

Greater accuracy may also be achieved by slightly overcorrecting the error with a second-order integrator. This can be accomplished either by making $R_2C_2 < R_1C_1$ or by having unequal gains in the two channels of the preamplifier in which addition is accomplished. The second-order integral in Fig. E-2 was not overcorrected.

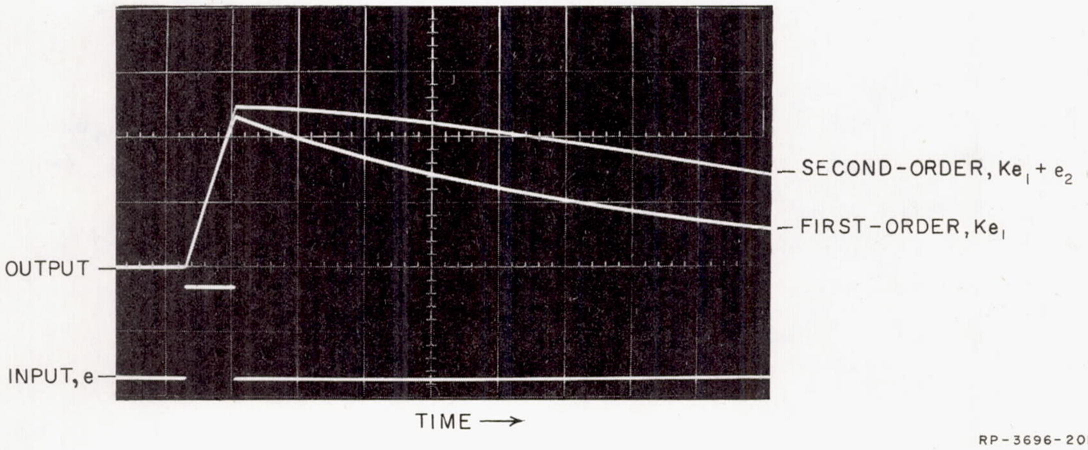

RP-3696-201

FIG. E-2 OSCILLOGRAM COMPARING FIRST-ORDER AND SECOND-ORDER INTEGRATION
RC = 300 μsec; Time Scale = 50 μsec/major div.

APPENDIX F

FLUX REFERENCE

APPENDIX F

FLUX REFERENCE*

The flux reference is an instrument for measuring either remanent or total magnetic flux switched by a current pulse. The use of the flux reference overcomes the problems of

(1) Not having a fixed flux standard

(2) Integrator droop

(3) Amplifier gain variations and nonlinearities

(4) Oscilloscope cathode-ray-tube distortions

(5) The tedious job of accurately reading signal deflections on the oscilloscope.

The flux reference consists basically of a standard core which is switched (from negative to positive remanence) simultaneously with the core to be measured, and a special integrator that integrates and sums (algebraically) $N\dot{\phi}$ of the standard core and the unknown $N\dot{\phi}$. The standard core has many separate sense windings that can be connected in series in order to cancel out the EMF due to the flux switching in the tested core. The circuit is shown in Fig. F-1(a). The component values given in this figure are the values for the flux reference that was built in this laboratory, and are included only as an example. Potentiometer R_4 gives a continuous fine variation of the flux reference output.

The R-C integrator consists of two resistors, R_1 and R_2, feeding into the same capacitor C. If Capacitor C is discharged at $t = 0$, then at $t = t_0$ the output e_C is given by

$$e_C = \frac{1}{RC}\int_0^{t_0} (e_{std} + e_u)dt - \frac{2}{RC}\int_0^{t_0} e_C dt \quad , \qquad \text{(F-1)}$$

---

* Developed by E. K. Van De Riet of Stanford Research Institute.

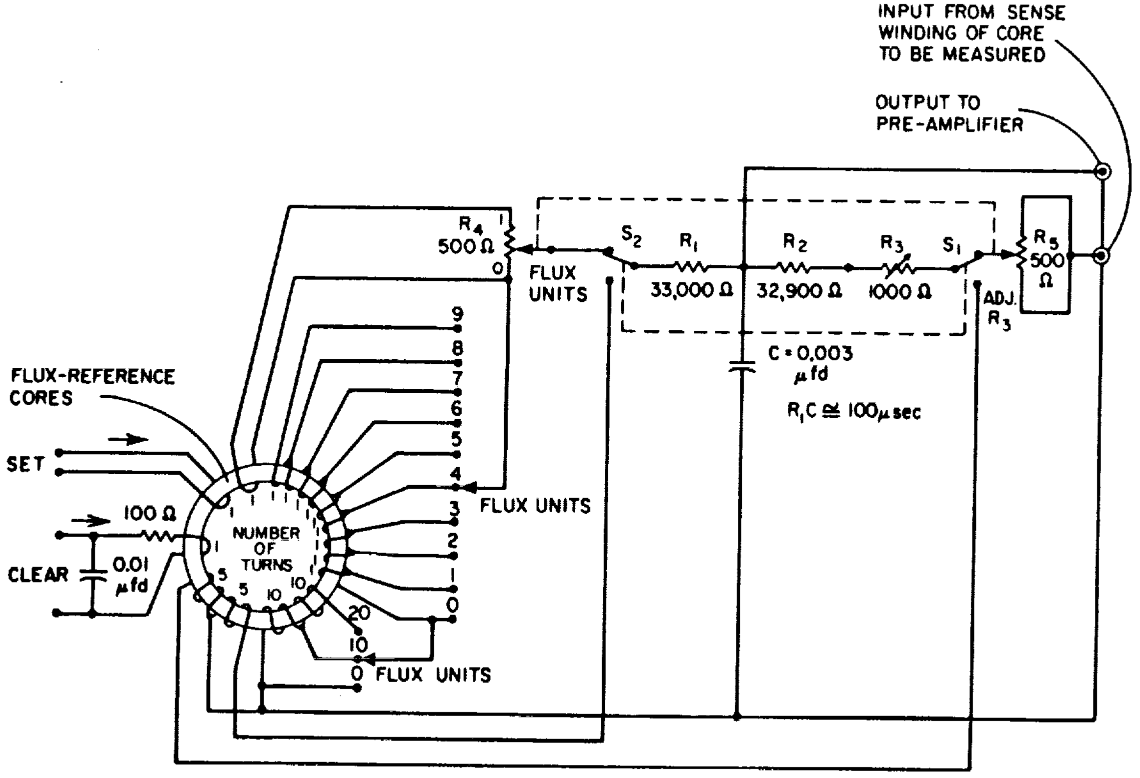

(a) CIRCUIT

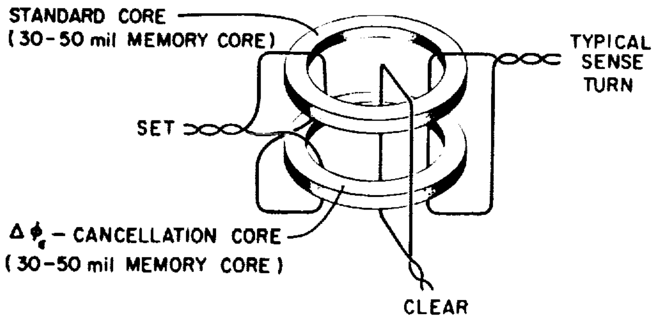

(b) WIRING OF FLUX-REFERENCE CORES

RC-3696-189

FIG. F-1 FLUX REFERENCE

where e_{std} is the output EMF from the standard core, e_u is the unknown EMF whose time integral is to be measured, and R is the total resistance on each side of C. The quantity e_{std} is given by

$$e_{std} = (N + P_4)\dot{\phi}_{std} \quad , \tag{F-2}$$

where N is the number of turns connected on the standard core, P_4 is the relative setting $(0 \leq P_4 \leq 1)$ of Potentiometer R_4, and $\dot{\phi}_{std}$ is $\dot{\phi}$ of the standard core. The value of R is

$$R = R_1 + R_4P_4(1 - P_4) = R_2 + R_3 + R_5P_5(1 - P_5) \quad . \tag{F-3}$$

If a positive $\int_0^{t_0} e_u dt$ is to be measured, then $\int_0^{t_0} e_{std}dt$ must be negative, and N and P_4 are adjusted so that $e_C = 0$ at $t = t_0$. Under this condition, Eq. (F-1) reduces to

$$\int_0^{t_0} e_u dt = -\int_0^{t_0} e_{std}dt + 2\int_0^{t_0} e_C dt \quad . \tag{F-4}$$

The quantity $\int_0^{t_0} e_{std}dt$ is obtained from Eq. (F-2), *i.e.*,

$$\int_0^{t_0} e_{std}dt = (N + P_4)\Delta\phi_{std} \quad , \tag{F-5}$$

where $\Delta\phi_{std}$ is known from having calibrated the standard core. The term $2\int_0^{t_0} e_C dt$ is the error in the measurement. Note that the error is proportional to the net area under the $e_C(t)$ curve between the times $t = 0$ and $t = t_0$ [*cf.* the flux sum waveform in Fig. F-2]. This net area can be reduced to zero by adjusting the timing of the flux-reference SET pulse relative to the SET pulse of the core to be measured, thereby eliminating the integrator droop problem. The area under the $e_C(t)$ curve for $t > t_0$ is of no concern. The effective time constant of this integrator is $RC/2$, as shown by the coefficient of the last term in Eq. (F-1). Potentiometer R_5 is ganged to Potentiometer R_4 ($R_5 = R_4$; $P_5 = P_4$) in order to equalize the time constant variations (as P_4 varies) for both inputs to the R-C integrator. The maximum time-constant variation [*cf.* Eq. (F-3)] with P_4 is about ±0.2%. However, as long as both

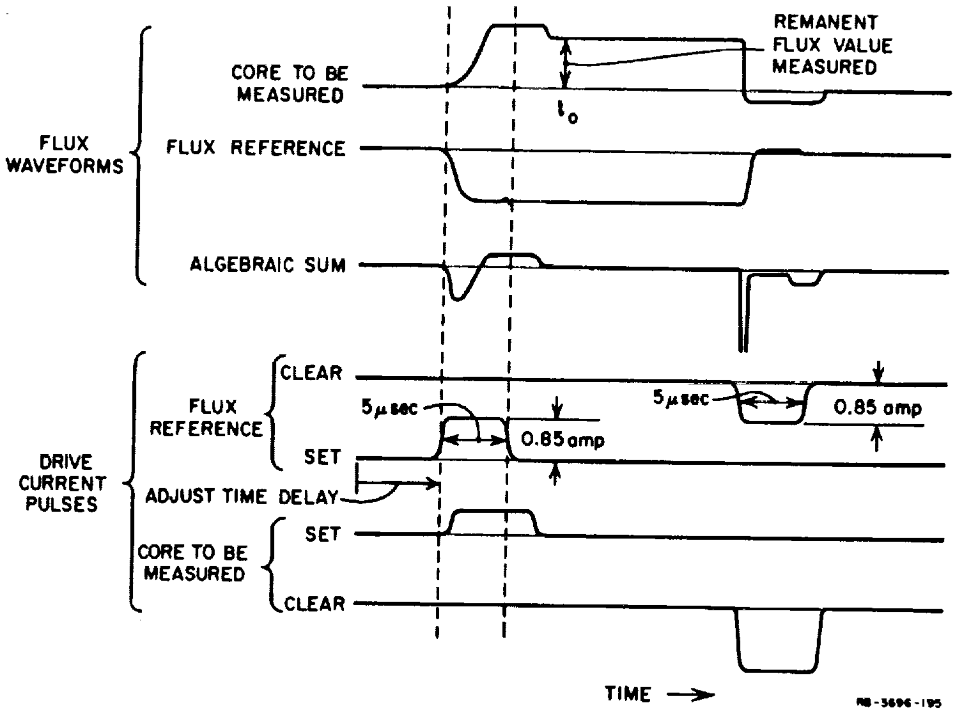

FIG. F-2 FLUX AND CURRENT WAVEFORMS IN MEASURING INELASTIC $\Delta\phi$ BY FLUX REFERENCE

time constants vary together, no error is introduced. The time constant of the two inputs are made exactly equal by switching S_1 and S_2 to their lower position and adjusting R_3 to give zero output [*cf.* Eq. (F-3)]. Second-order integration could be used, thereby reducing the accuracy to which the plus and minus areas of the $e_C(t)$ curve must be made equal. Even without second-order integration, the areas need only be crudely nulled. This can easily be judged by looking at $\phi(t)$ on the oscilloscope.

The standard core, which is a 30-50 mil ferrite memory core, is connected to another identical core ($\Delta\phi_\epsilon$-cancellation core) so as to cancel the elastic flux changes of the standard core during SET time [see Fig. F-1(a)]. The edges of these cores were rounded so that wiring short-circuits could be avoided. After the 42 turns were wound, the cores were potted for permanency of wire placement, and placed in a small temperature-controlled oven to remove problems due to temperature variations. The temperature was set well above ambient, so that automatic temperature control by heating only could be employed. The oven heater operates from a 28 v dc source.

The *R-C* network in the CLEAR winding serves to increase the CLEAR pulse fall time to about 1 μsec in order to eliminate the possibility of unsetting due to ringing.

The CLEAR and SET pulses required for the flux reference can be generated either externally or internally, so long as the pulse timing can be properly adjusted. An internal pulse source, of course, makes for a simpler experimental setup and reduces the possibility of errors for routine experimental measurements.

The units of the flux reference are not standard units of webers or maxwells, but need to be calibrated in some such standard units. This calibration process must be very carefully done, unless only relative flux values are to be measured. The instrument used in this laboratory was calibrated by carefully photographing the $\dot{\phi}(t)$ waveform of the flux reference and measuring its area. The resulting calibration factor was: one unit = 3.64 maxwells (or 0.0364 v μsec per turn) ±1%. The noise level typically limits the precision to within ±0.1 maxwell. The maximum capacity is 110 maxwells.

The actual use of the flux reference to measure the flux switched by a particular drive pulse consists of three steps. First, the flux reference is adjusted to obtain a null on the oscilloscope. Second, the time delay of the flux reference drive pulse is adjusted until the flux sum waveform has approximately equal positive and negative areas. (In some cases, the first step may need to be repeated.) Third, the flux value is read from the dials of the flux reference.

APPENDIX G

TECHNIQUE FOR OBTAINING $\dot{\phi}(\phi)$

APPENDIX G

TECHNIQUE FOR OBTAINING $\dot{\phi}(\phi)$

Automatic tracing of $\dot{\phi}(\phi)$ can be accomplished by feeding the $\dot{\phi}$ signal to the vertical axis of an oscilloscope and the integral of $\dot{\phi}(t)$ on the horizontal axis. The integration of $\dot{\phi}(t)$ to obtain $\phi(t)$ for the horizontal signal can satisfactorily be accomplished by the use of second-order integration (see Appendix E). The circuit is shown in Fig. G-1(a). The $\dot{\phi}$ preamplifier is used to introduce a time delay that is equal to the time delay obtained in the ϕ preamplifier. Figure G-1(b) shows the timing of the pulses, and Fig. G-1(c) shows the resulting $\dot{\phi}(\phi)$; the numbers correspond to the numbers on the $\dot{\phi}(t)$ curve in Fig. G-1(b). The line segments 4-5, 7-8, 11-12, and 14-1 in Fig. G-1(c) are a result of integrator droop. They are exaggerated in the figure for clarity. Since the CRT beam spends a relatively large amount of time on the segment 14-1, this portion of the trace is overly bright. A Z-axis pulse is used to eliminate this and other undesirable portions of the trace. By the use of multiple exposures, the function $F(\phi)$ can be superimposed upon an oscillogram of $\dot{\phi}(\phi)$, thereby indicating the part of $\dot{\phi}(\phi)$ for which $F(\phi)$ is constant.

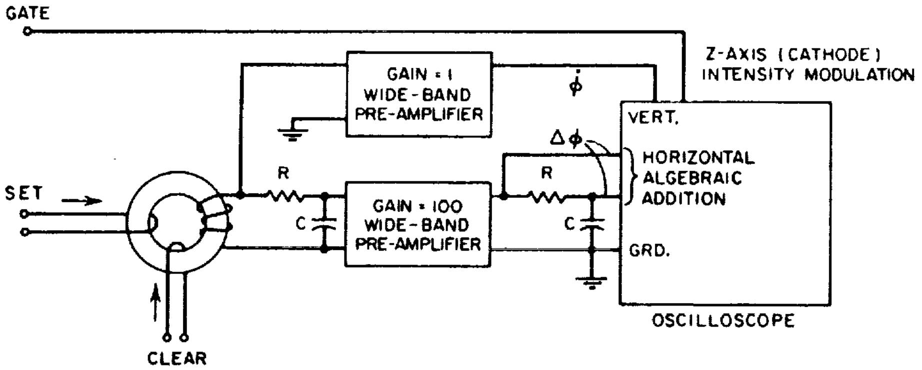

(a) CIRCUIT

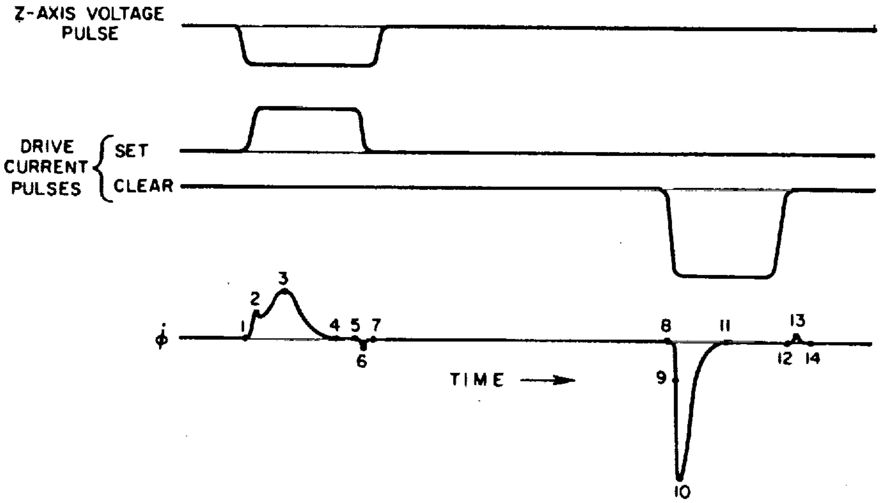

(b) PULSE TIMING

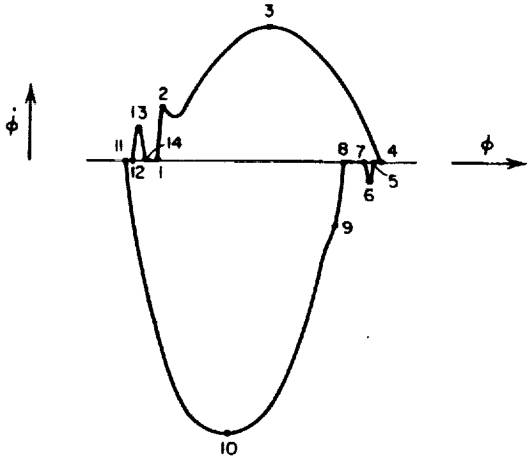

(c) RESULTING $\dot{\phi}(\phi)$ CURVE

RB-3696-190

FIG. G-1 TECHNIQUE USED TO OBTAIN $\dot{\phi}(\phi)$ CURVE

APPENDIX H

TEST PROCEDURES FOR DETERMINATION OF LEG PARAMETERS

APPENDIX H

TEST PROCEDURES FOR DETERMINATION OF LEG PARAMETERS

Step-by-step laboratory test procedures for determination of leg parameters, as discussed in Sec. II-C, are described as follows.

1. STATIC $\phi(F)$ EXPERIMENT

The circuit diagram is shown in Fig. H-1. Inductor L is an air core inductor, which serves to block any current that results from $N_s\dot{\phi}$ during the CLEAR time. The flux change can be measured either by means of the flux reference (*cf*. Appendix F) or by means of a second-order integrator (*cf*. Appendix E). The test procedure is outlined as follows.

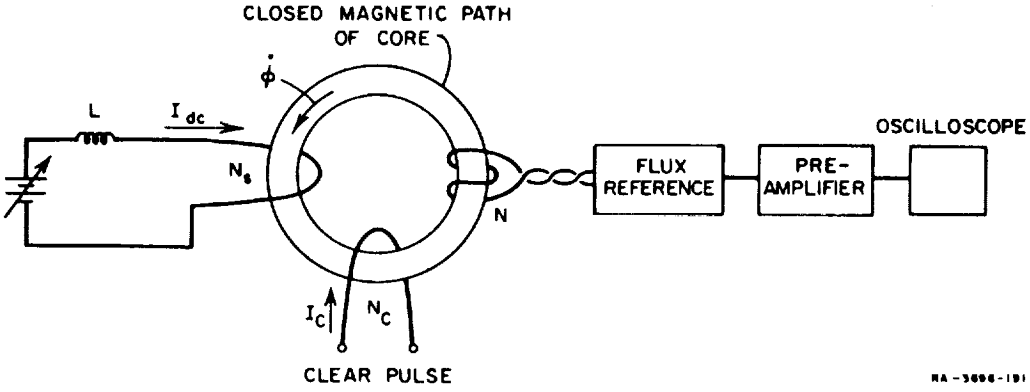

FIG. H-1 STATIC ϕ(F) EXPERIMENT

a. MIXED INELASTIC AND ELASTIC FLUX SWITCHING

(1) Select a closed magnetic path in the core to be tested (*cf*. Sec. II-C-2), preferably composed of uniform cross-sectional area.

(2) Block all other paths by means of a short-circuited winding (*cf*. Sec. II-C-2).

(3) Connect the circuit as shown in Fig. H-1, and adjust the repetition rate of the CLEAR pulse to about 60 cps. Be sure that the dc SET winding has a low enough resistance so that the SET winding would not heat the core for large values of I_{dc}.

(4) Establish an $N_C I_C$ that is sufficient to give a reproducible remanent state by making the pulse duration long enough (*e.g.*, 10 μsec) and the amplitude high enough. If the $\Delta\phi$ observed for a value of $N_s I_{dc}$ slightly beyond threshold changes as $N_C I_C$ is increased (say, by a factor of 2), then the initial value of $N_C I_C$ is insufficient.

(5) Record $N\Delta\phi$ versus $N_s I_{dc}$, adjusting $N_C I_C$ at each point such that the quantity $(N_C I_C - N_s I_{dc})$ remains constant (*cf*. Figs. 17 and 18). Measure $\Delta\phi$ at its peak value during the CLEAR pulse.

(6) Be sure to take a point for $N_s I_{dc} = (1/2)N_C I_C$ so that the location of $\phi = 0$ on the graph can be determined, as will be shown later.

b. ELASTIC FLUX SWITCHING

(1) Remove I_{dc}.

(2) Make $N_C I_C$ equal to the value used in Part *a* above to clear the core initially.

(3) Record $N\Delta\phi$ versus $N_C I_C$ for $N_C I_C$ varying between zero and the value used in Part *a* above. Measure $N\Delta\phi$ at its peak value during the CLEAR pulse. Record $N\Delta\phi$ and $N_C I_C$ as negative quantities.

c. DATA PROCESSING

(1) Shift the origin by subtracting from each $N\Delta\phi$ value (assumed positive) of Part *a* one half of the $N\Delta\phi$ value obtained for $N_s I_{dc} = (1/2)N_C I_C$. The resulting differences are the corresponding $N\phi$ values.

(2) Divide these values of $N\phi$ by N and multiply by the calibration factor of the flux reference or the second-order integrator to obtain ϕ in conventional units (*e.g.*, maxwells or v μsec per turn).

(3) Plot these ϕ values versus F, where F is $N_s I_{dc}$ of Part *a*(5). This curve will fall in the first and fourth quadrants of the graph.

(4) Determine ϕ_r from this graph by reading $|\phi|$ for $F = 0$.

(5) Divide each of the $N\Delta\phi$ values of Part *b*(3) by N and multiply by the calibration factor of the flux reference, or the second-order integrator.

(6) Subtract from each of these negative $\Delta\phi$ values the value of ϕ_r determined in Part *c*(4).

(7) Plot these negative ϕ values versus F, where F is $N_C I_C$ of Part *b*(3). This curve will fall in the third quadrant of the graph.

Determination of the static $\phi(F)$ curve is now completed. If necessary, a static $\phi(F)$ loop may be drawn by adding a curve that is symmetrical with respect to the origin.

2. $\dot{\phi}_p(F)$ EXPERIMENT

The circuit diagram is shown in Fig. H-2. The mercury choppers and the calibrated dc voltage references in this figure serve to measure the SET pulse amplitude and the peak switching voltage $N\dot{\phi}$ conveniently and accurately. The choppers superimpose on the oscilloscope both the signal (SET pulse or $N\dot{\phi}$) and the dc reference voltage. The reference voltage can then be adjusted to be equal to the pulse amplitude or the peak $N\dot{\phi}$,

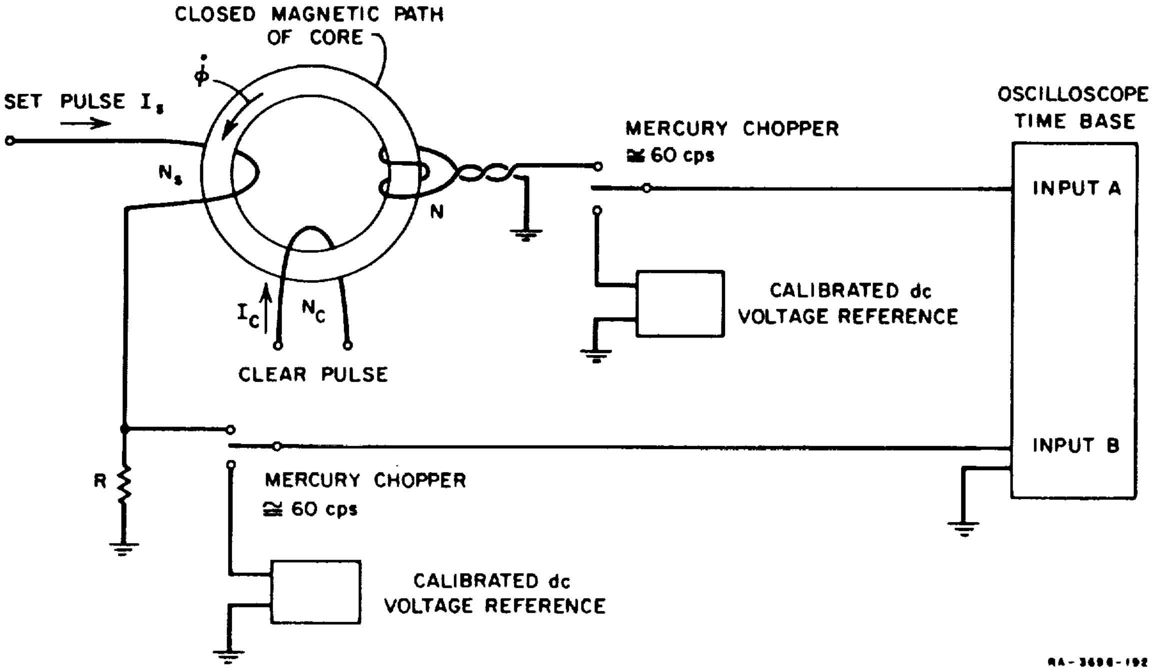

FIG. H-2 $\dot{\phi}_p$(F) EXPERIMENT

and its value read from the dials of the voltage reference. This procedure eliminates such problems as cathode-ray-tube distortion, time variations of the base line, parallax with the graticule, time variations of the oscilloscope vertical amplifier gains, and inaccuracy in reading the values from the graticule. Care must be taken to avoid distortion of the signal in passing through the chopper. The calibration resistor R must have a very low L/R ratio and an accurately known resistance value. The chopper technique described here can also be used to measure the CLEAR pulse amplitude in this experiment and both the SET and CLEAR pulse amplitudes in the static $\phi(F)$ experiment. The test procedure is as follows.

(1) Select a closed magnetic path in the core (*cf*. Sec. II-C-2).

(2) Block all other paths (*cf*. Sec. II-C-2).

(3) Connect the circuit as shown in Fig. H-2.

(4) The rectangular SET pulse should have a short rise time, so that most of the switching occurs while I_s is constant. The SET pulse duration is not critical, so long as it is sufficient to allow $\dot{\phi}$ to reach its peak value.

(5) Establish an $N_C I_C$ amplitude that is sufficient to give a reproducible remanent state. If the $\dot{\phi}(t)$ observed for a given value of $N_s I_s$ is changed significantly as $N_C I_C$ is doubled, then the initial value of $N_C I_C$ is insufficient.

(6) Record $N\dot{\phi}_p$ versus $N_s I_s$. Do not take $\dot{\phi}_p$ readings for $N_s I_s$ larger than about 80% of the value for which $\dot{\phi}_p$ begins to occur during the rising portion of the SET pulse.

(7) Divide the $N\dot{\phi}_p$ values by N and plot $\dot{\phi}_p$ versus F, where F is $N_s I_s$.

REFERENCES

1. D. Nitzan, "Flux Switching in Multipath Cores," Report 1, to Jet Propulsion Laboratory, Contract 950095 under NASw-6, SRI Project No. 3696, Stanford Research Institute, Menlo Park, California (November 1961).
2. V. W. Hesterman, "Evaluation of Flux-Switching Models for Magnetic Devices," Technical Report 2, Contract Nonr 2712(00), SRI Project No. 2697, Stanford Research Institute, Menlo Park, California (September 1961).
3. J. E. Knowles, "Some Observations of Bitter Patterns on Polycrystalline 'Square Loop' Ferrites, and a Theoretical Explanation of the Loop Shape and Pulse Characteristics of the Material," *Proc. Phys. Soc.* (London) **75**, p. 885 (1960).
4. S. Ramo and J. R. Whinnery, *Fields and Waves in Modern Radio* (John Wiley & Sons, Inc., New York, N.Y., 1953).
5. P. Moon and D. E. Spencer, *Field Theory for Engineers* (D. Van Nostrand Company, Inc., Princeton, N.J., 1961).
6. U. F. Gianola and T. H. Crowley, "The Laddic, a Magnetic Device for Performing Logic," *Bell Syst. Tech. J.* **38**, pp. 45-72 (January 1959).
7. U. F. Gianola, "Lesser-Known Properties of Ferrite Multi-Apertured Cores," *Proc. 1960 Electronic Components Conference, Washington, D.C.*, pp. 111-115 (May 1960).
8. E. U. Cohler and T. E. Baker, "Geometric Factors in Multiaperture Ferrite Devices," *Special Technical Conference on Nonlinear Magnetics, Los Angeles,* pp. 215-249 (November 1961).
9. G. C. Feth, "Core-Reset Functions in Magnetic Amplifier Analysis, Part II - Determination of Amplifier Performance," *AIEE Trans.* **77**, Part I, pp. 510-518 (September 1958).
10. D. R. Bennion, "Research on Multi-Aperture Magnetic Logic Devices," Tech. Report 1, Contract Nonr 2712(00), SRI Project No. 2697, Stanford Research Institute, Menlo Park, California (May 1960).
11. P. Hammond, "Leakage Flux and Surface Polarity in Iron Ring Stampings," *Proc. IEE (London)* **102**, Part C, pp. 138-147 (January 1955).
12. M. A. Thomae, "A New Technique for Analogue Integration and Differentiation," *IRE Trans. EC*-**9**, pp. 507-509 (December 1960).

INDEX

INDEX

INDEX

STANFORD
RESEARCH
INSTITUTE

MENLO PARK
CALIFORNIA

Regional Offices and Laboratories

Southern California Laboratories
820 Mission Street
South Pasadena, California

Washington Office
808 17th Street, N.W.
Washington 5, D.C.

New York Office
270 Park Avenue, Room 1770
New York 17, New York

Detroit Office
The Stevens Building
1025 East Maple Road
Birmingham, Michigan

European Office
Pelikanstrasse 37
Zurich 1, Switzerland

Japan Office
911 Iino Building
22, 2-chome, Uchisaiwai-cho, Chiyoda-ku
Tokyo, Japan

Representatives

Honolulu, Hawaii
Finance Factors Building
195 South King Street
Honolulu, Hawaii

London, England
19 Upper Brook Street
London, W. 1, England

Milan, Italy
Via Macedonio Melloni 40
Milano, Italy

London, Ontario, Canada
P.O. Box 782
London, Ontario, Canada